The Dissertation Committee for Gaurav Chaudhary
certifies that this is the approved version of the following dissertation:

Topological Superconductivity in Chern Insulators

Committee:

Allan H. MacDonald, Supervisor

Qian Niu

Gregory A. Fiete

Chih-Kang Shih

Emanuel Tutuc

Topological Superconductivity in Chern Insulators

by

Gaurav Chaudhary

DISSERTATION

Presented to the Faculty of the Graduate School of

The University of Texas at Austin

in Partial Fulfillment

of the Requirements

for the Degree of

DOCTOR OF PHILOSOPHY

THE UNIVERSITY OF TEXAS AT AUSTIN

August 2019

Dedicated to my parents.

Acknowledgments

I am grateful to many of my family members, friends, mentors, and collaborators, who over the course of past few years helped me scientifically or motivationally. I take this opportunity to thank them.

First, I thank my advisor Prof. Allan MacDonald for his endless support. Allan is rare combination of a world renowned physicist and a very kind and supportive advisor. In our cut-throat vocation, Allan taught me to strive for deep understanding over quick results, which can advance collaborative science in an effective way. I am grateful for his patience with me and going out of his way to make himself available. After three wonderful courses and endless discussions it would not be an overstatement to say Allan is the reason I know a thing or two about condensed matter physics.

Next, I would like to thank Prof. Greg Fiete for an ongoing collaboration, serving in my committee, teaching wonderful course on statistical mechanics, and being overall encouraging and helping person.

I thank Prof. Qian Niu, Prof. Ken Shih, and Prof. Emanuel Tutuc for serving in my committee. Directly or indirectly I learned many aspects of condensed matter physics and research in general from them.

During last year of my undergraduate studies, I fortunately ended up in great mentorship of Prof. V. Ravishankar. During that year, he supervised my undergraduate thesis, gave wonderful lectures on quantum information and group theory, and his mentorship methods gave me confidence to work in theoretical physics. I thank him for all his inspiration.

Administration at UT Physics has helped me through all paper works including extra burden that comes with being an international student. For that, I thank the administration at physics department, especially Michele Landfield and Jane Ann Parker at CQS for making my life easier.

I thank Prof. Samir Lounis, Manuel dos-Santos Dias, Prof. Dmitry Efimkin, Prof. Xiao Li, Martin Rodriguez-Vega, Zexun Lin, Yongxin Zeng,

Chao Lei, Fei Xue, Ming Xie, Jihang Zhu and Pawel Potasz for collaborations of various degrees of magnitude and success. Special thanks go to Manuel for being a patient teacher during a successful collaboration.

I thank Hua Chen, Fengcheng Wu, Nemin Wei, Igor Blinov, Lukas Linhart, Benedetta Flebus, Chunli Huang, Ajesh Kumar, and other current and past group members for various discussions, from which I benefited immensely. Special thanks to Igor and Dmitry for the gung-ho Russian way of discussions and questioning, Ajesh and Chunli for prolonged lunch time discussions.

Apart from the above mentioned people whose direct professional help I benefited from, I was lucky to have friends who helped me keep my sanity. Akshay for his consistent help and mentorship from my day zero in Austin, Natasa for all the friendly advices and help that came even before asking, and that one time when we actually discussed math, Rahul and Amrita for sticking around when my other Austin friends were migrating elsewhere, my UT physics friends: Yorgos, Stefan, Josiah, Abhranil (special thanks to Yorgos and Sarah for hosting thanksgiving dinners and other get-togethers), my undergrad physics friends (aka Satpura EP gang): Anmol, Ambarish, Parag, Mayank, Jai, Shadman, Puneet, Srivatsan, Satvik, and Umesh, my other friends from Satpura: Gaurav Assat, Naman, Avnish, Nilesh (special thanks to Gaurav Assat for sharing the PhD journey for most part), my roommate-friends over the years: Areesh, Adarsh, Gaurav Assat (special thanks to Areesh for staying my roommate for all the years), my professional hiking buddy Kelly, and more than anyone else my girlfriend Jennifer for her constant support over the last year.

Apart from the above mentioned humans, I would like to thank non-human creatures in my life. Perfect Gorgeous (P. G.) Richards, Simmi Sen Verma, Lola Serwe Stratis, and Balthazar Archibald Prancy Paws III. You guys are the best!

Finally, I would like to thank my family to whom this thesis is dedicated. To my loving parents and my sister who were my first science teachers, and who let me be at the diametrically opposite part on the globe to fulfill my ambition.

Topological Superconductivity in Chern Insulators

Publication No. _____

Gaurav Chaudhary, Ph.D.
The University of Texas at Austin, 2019

Supervisor: Allan H. MacDonald

This dissertation presents studies of topological superconductivity in Chern insulator systems. In particular, when a Chern insulator such as a quantum Hall or a quantum anomalous Hall system is proximity coupled to a trivial s-wave superconductor. While quantum anomalous Hall based system is investigated in detail in both one and two dimensions, the focus is solely on two dimensions in quantum Hall bases system. Both quantum Hall and quantum anomalous Hall break time reversal ($\mathcal{T}$)-symmetry. Hence throughout this thesis, we focus on the $\mathcal{T}$-symmetry broken topological superconductor systems, which fall in the class $\mathbb{D}$ of the Altland-Zirnbauer classification.

After a brief introduction to thesis in chapter 1 and review of topological superconductivity in chapter 2, in chapter 3, a realistic system motivated from the experimental observation of the quantum anomalous Hall effect is considered. The focus of this chapter is on one dimensional (1D) topological superconducting phase in thin ribbon geometries [Phys. Rev. B 97, 081102(R)]. It identifies the quantum anomalous Hall based system as highly controllable platform for Majorana zero modes, which can be potentially used as Majorana braiding device.

In chapter 4, two dimensional (2D) topological superconducting phase in the quantum Hall based system is studied [arXiv:1903.12249]. Because of the inherent requirement of the external magnetic field to achieve quantum Hall physics, this system requires consideration of vortex lattice phase in the parent superconductor. It is shown that the topological superconducting phase

is determined by the type of vortex lattice. Hence, making quantum Hall based system different than quantum anomalous Hall based system, giving much richer phase diagram. Experimental protocol to engineer and observe Majorana edge modes in this system is also discussed.

In chapter 5, reentrant superconductivity under magnetic fields beyond semiclassical critical magnetic field is discussed. It is argued that recently discovered superconductivity in magic angle twisted bilayer graphene (MATBG) can be a promising ground to observe this phase.

In chapter 6, recent transport experiments in quantum anomalous Hall/superconductor devices are discussed. The two main experiments on this system have contradictory results and there is widespread debate on possible explanations of the experimental observations, which can born out of chiral Majorana mode (*i.e.* topological) or disorder (*i.e.* trivial). The main arguments on both sides are summarized and some strategies to resolve the debate are proposed.

Table of Contents

List of Figures

List of acronyms

1D one dimensional

2D two dimensional

2DEG two-dimensional electron gas

2DES two-dimensional electron system

3D three-dimensional

BdG Bogoliubov-de Gennes

COM center-of-mass

DFT density-functional theory

FFLO Fulde–Ferrell–Larkin–Ovchinnikov

MATBG magic angle twisted bilayer graphene

TI topological insulator

$\mathcal{T}$ time reversal

Chapter 1

Introduction

The discovery of the quantum Hall effect [1] started a new paradigm in condensed matter physics, related to the topological phases of quantum matter [2]. When a two-dimensional electron system (2DES) is under strong perpendicular magnetic field, the bulk becomes insulating, with conducting edge states [3, 4]. The Hall conductance becomes quantized in the unit of e^2/h and has mere uncertainty of one parts per billion, which survives even in the presence of disorder. This extraordinary quantization is due to the topological robustness first pointed out by Thouless and collaborators [5, 6]. It was shown by Haldane [7] using a lattice model for graphene with complex next-nearest neighbor hopping, that magnetic field is not a requirement for quantized Hall conductance. Thus termed quantum anomalous Hall effect, shows the same topological character as quantum Hall effect without external magnetic field. The quantum anomalous Hall effect was later experimentally observed in magnetically doped thin films of three dimensional 3D topological insulator (TI) [8].

The Quantum Hall effect is the earliest known example of topological phase and together with its close cousin quantum anomalous Hall effect forms the most well understood class of topological phases, *i.e.* Chern insulators. Chern insulators have broken $\mathcal{T}$-symmetry, and the bulk insulating phase is protected by the chiral conducting edge states. The topological invariant is the integral of Berry curvature over the Brillouine zone [9], which is also equal to the number of chiral edge modes.

Topological superconductivity, which is the focus of this thesis, is the generalization of the concept of topology from an insulating system to the superconducting system [10]. At the mean-field approximation, superconductivity is described by the Bogoliubov-de Gennes (BdG) Hamiltonian in the

electron-hole basis. The eigenstates of the superconducting BdG Hamiltonian describe the Bogoliubov quasiparticles. In the language of the Bogoliubov quasiparticles, the system is effectively non-interacting. The topological superconductivity then corresponds to the non-trivial topology of the mean-field BdG Hamiltonian, which in many cases is mathematically similar to the non-trivial topology describing the non-interacting electron Hamiltonian.

The BdG formulation doubles the Hilbert space of the system via introducing particle-hole redundancy. Because of the particle-hole symmetry (redundancy), for a topological superconductor the boundary modes coming from the non-trivial topology are equal superposition of electrons and holes. The creation and annihilation operators of these boundary modes follow a peculiar relation $\hat{\gamma}_k = \hat{\gamma}^\dagger_{-k}$ for the propagating edge modes of a 2D-topological superconductor or $\hat{\gamma} = \hat{\gamma}^\dagger$ for point like modes at the end on one dimensional (1D)-topological superconductor. This peculiar relation is reminiscent to the Majorana Fermions first proposed in high energy physics context as real solutions of the free particle Dirac equation by Ettore Majorana [11, 12]. The Majorana Fermion is its own antiparticle. The Majorana modes found in topological superconductors are quasiparticle analogue of the Majorana Fermions. However, unlike the free Majorana Fermions, the Majorana modes do not follow Fermionic exchange statistics. In 2D, the Majorana modes follow non-Abelian exchange statistics, for which they are shown to be of importance in topological quantum computation [13]. Because of their fundamental importance and potential applications alike, the quest for Majorana modes in 2DES has been one of the most active areas of condensed matter research over the past decade [14].

Since natural topological superconductors are rare, efforts have been made to engineer them. The first success was achieved by proximity coupling semiconductor quantum wires with strong Rashba spin-orbit coupling to an s-wave superconductor under a Zeeman field [15, 16, 17, 18, 19, 20, 21]. Topological superconductivity can also be achieved by proximity coupling s-wave superconductors to TI surface states [22, 23, 24, 25, 26, 27, 28], placing magnetic ion chains/islands on top of an s-wave superconductor [29, 30, 31], and occurs in some Fe-based superconductors [32, 33, 34, 35]. For topological superconducting systems based on proximity-coupling to parent s-wave superconductors,

the general scheme is to obtain the topological property from an exploitable feature of the electronic structure of the host system, for example from the large spin-splitting in the Dirac-like surface state of 2D band TI [22]. Alternately, the topological nature can stem from single particle Chern bands [25].

This thesis focuses on possible topological superconductivity and the Majorana modes when Chern insulator system, such as when quantum Hall or quantum anomalous Hall is proximity coupled to an s-wave superconductor.

In chapter 2, we first review the theory of $\mathcal{T}$-symmetry broken topological superconductivity in 1D and 2D. We show the presence of Majorana zero modes at the end of a 1D topological superconductors and chiral Majorana edge modes at the boundary of a 2D topological superconductor. A spinless superconductor with p-wave pairing symmetry serves as the conceptually simplest system to understand topological superconductivity and the Majorana modes. In the later part, we study a model quantum anomalous Hall system proximity coupled to an s-wave superconductor. We study the topological phase diagram in this system and show the presence of topological superconducting phase by comparing the low energy effective Hamiltonian with a model spinless p-wave superconductor.

In chapter 3, we study quantum wire geometry in a quantum anomalous Hall system proximity coupled to an s-wave superconductor. A thin film of magnetically doped topological superconductor can be used to achieve the quantum anomalous Hall phase in the normal part. We show that quasi 1D quantum wires can be defined on the surface of the magnetic-TI by gate arrays. When the magnetic-TI is in the quantum anomalous phase, the the gate defined quantum wires on the Magnetic-TI/superconductor hybrid systems have especially broad stability regions for both topological and non-topological states, facilitating creation and manipulation of the Majorana modes on the surface of the magnetic TI. Majorana braiding is an essential fundamental operation to achieve topological quantum computation and requires two dimensions to achieve. The quantum anomalous Hall based device is inherently 2D with quasi 1D regions defined by gates. This structure makes it an ideal platform to braid Majorana with electrostatic gating.

In chapter 4, we study quantum Hall system proximity coupled to an s-wave superconductor. In this system the electrons are Landau quantized in

their normal state and superconductor exists in vortex lattice phase because of the external magnetic field. We show that the appearance of topological superconducting phases with an odd number of Majorana edge modes is dependent on the structure of the system's vortex lattice. Hence, the vortex lattice structure is the main tuning knob for topological phases. More precisely, vortex lattices containing odd number of superconducting flux quanta per unit cell, always support an even number of chiral edge channels and are therefore adiabatically connected to normal quantum Hall insulators. We end the chapter by discussing strategies to engineer chiral topological superconductivity in this system by manipulating vortex lattice structure.

In chapter 5, we evaluate the sum of particle-particle ladder diagrams of electrons in the Landau levels, interacting with each other via short range attractive interaction. We consider a class of simple band models for the electrons and show the reentrance of superconductivity beyond the semi-classical upper critical magnetic field (H_{c2}). The reentrance of superconductivity is related to the very high density of states available to interacting electrons, when a single Landau level is close to the Fermi level. We argue that the recently discovered superconductivity in magic angle twisted bilayer graphene [36] is a promising system to observe this remarkable phenomena. This chapter takes a detour from the main focus on topological superconductivity in this thesis. However, superconductivity under broken $\mathcal{T}$-symmetry and Landau quantization of pairing electron is well in line with rest of the thesis.

In chapter 6, we first review the recent experimental efforts in finding 2D topological superconductor and chiral Majorana edge mode in transport experiments with quantum anomalous Hall system [26, 37, 38]. We highlight the different possible experimental interpretations and contradicting nature of the experimental findings in the above mentioned two experiments [26, 37]. We discuss future theory work and possible ways to settle the debate between contradicting experiments.

Chapter 2

Topological superconductivity: Review

In this chapter, we review the concept of the $\mathcal{T}$-symmetry broken topological superconductivity in both one 1D and 2D, using a model spinless superconductor with p-wave pairing symmetry [10, 39, 40]. In this model system, we show the presence of Majorana modes. In the later part, we take a simple quantum anomalous Hall model proximity coupled to s-wave superconductor and show that the low energy effective Hamiltonian is similar to the model chiral topological superconductor Hamiltonian in 2D [25]. This sets us in the direction to study Chern insulators as a suitable platform for topological superconductivity and Majorana modes in detail in the following chapters [27, 41].

Here we mention that throughout this thesis our focus is on broken $\mathcal{T}$-symmetry systems, which fall into the class $\mathbb{D}$ of the Altland-Zirnbauer classification [42, 43]. Theoretically, based on the symmetry class the BdG Hamiltonians can have more exotic topological structure [43]. However, the most experimental progress has been made in broken $\mathcal{T}$-symmetry systems [18, 19, 20, 21, 23, 24, 25, 26, 27, 28, 29, 30, 31] and remain the focus here.

2.1 Topological superconductivity in one dimension: Kitaev chain

A 1D-spinless superconductor is described by the lattice Hamiltonian,

$$H = -\mu \sum_j \hat{c}_j^\dagger \hat{c}_j \; - \; \frac{1}{2} \sum_j (t \hat{c}_j^\dagger \hat{c}_{j+1} + \Delta \hat{c}_j \hat{c}_{j+1} + h.c.) \,, \tag{2.1}$$

where all the length scales are normalized by the lattice constant. Here μ is the chemical potential, $t > 0$ is the nearest neighbor hopping strength, Δ is the superconducting pairing amplitude, and $\hat{c}_j$ annihilates an electron at

site j. Notice, because the electrons are spinless, the on-site superconducting interaction is forbidden due to Pauli's exclusion principle, and the simplest allowed superconducting interaction is the nearest neighbor term. To study the bulk properties of the chain, we use the periodic boundary condition and first transform the Hamiltonian to momentum space ($k \in [-\pi, \pi]$) and then use the particle-hole basis $\hat{\psi}_k = [\hat{c}_k, \hat{c}^\dagger_{-k}]^T$ to write the Hamiltonian in the standard BdG form:

$$H_k = \frac{1}{2}\sum_k \hat{\psi}^\dagger_k H_{BdG} \hat{\psi}_k \,, \tag{2.2a}$$

$$H_{BdG} = \begin{pmatrix} H_0(k) & \hat{\Delta}(k) \\ \hat{\Delta}^\dagger(k) & -H_0^*(-k) \end{pmatrix} . \tag{2.2b}$$

Here for the purpose of generality, we have written a more generic form of the BdG Hamiltonian. For the particular case of superconducting Hamiltonian in Eq. 2.1, the elements of the BdG Hamiltonian are simply

$$H_0(k) = -t\cos k - \mu \,, \quad \hat{\Delta}(k) = i\Delta \sin k \,. \tag{2.3}$$

The effective pair potential in momentum space $\Delta(k) = i\Delta \sin k$ takes a non-isotropic form, which has the p-wave form at low energy. The quasiparticle spectrum of the above Hamiltonian is

$$E_\pm(k) = \pm\sqrt{(t\cos k + \mu)^2 + \Delta^2 \sin^2 k} \,. \tag{2.4}$$

If one tunes the chemical potential μ from a very large negative value to a very large positive value, the spectrum becomes gapless with Dirac crossings at $k = 0$ when $\mu = -t$ and at $k = \pm\pi$ when $\mu = t$ as shown respectively in Fig. 2.1(b) and 2.1(d). The Dirac like gap closing and opening at isolated points gives the first indication of topological nature of this Hamiltonian. As we will show next, for $|\mu| < t$ the system is in topologically non-trivial phase and $|\mu| > t$, is in topologically trivial phase. Before going into the precise definition of this topology, it is worthwhile to consider the limiting case of non-trivial topology. In the limit $|\mu| \gg t, \Delta$, one can ignore some terms in the BdG Hamiltonian and write it as, $H_{BdG} \sim \mu\sigma_z$. Which simply describes a trivial insulator, since as $\mu \to -\infty$, there are no electrons present. The empty state is topologically trivial and the as long as the bulk gap does not close the trivial topological characterization remains conserved.

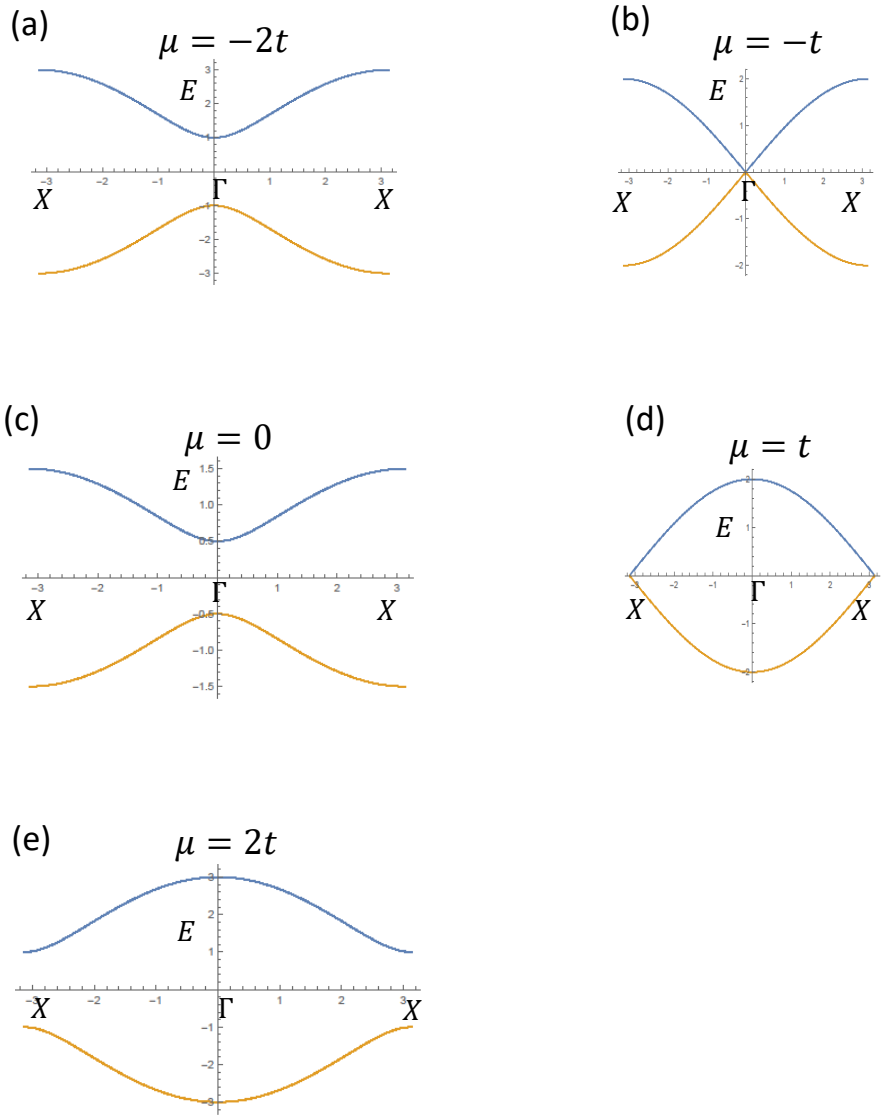

Figure 2.1: The BdG quasiparticle spectrum for 1D Kitaev chain model as chemical potential μ is tuned: (a) When $\mu = -2t$, the gapped phase is topologically equivalent to trivial vacuum. (b) At $\mu = -t$, Dirac like gap closing occurs at $k = 0$ point. (c) When $|\mu| < t$, the gap opens and the gapped phase is in topologically non-trivial regime. (d) At $\mu = t$, Dirac like gap closing occurs at $k = \pm\pi$-points. (e) When $\mu = 2t$, the gapped phase is topologically equivalent to a trivial insulator.

2.1.1 $\mathbb{Z}_2$-Topological invariant

The simplification of a 2×2 Hamiltonian makes it easier to understand topological invariant in a more intuitive manner. The projection of a general 2×2 Hamiltonian on Pauli matrices

$$H = h_0(k)\sigma_0 + \boldsymbol{h}(k) \cdot \boldsymbol{\sigma}\,, \tag{2.5}$$

has spectrum,

$$E(k) = h_0(k) \pm |\boldsymbol{h}(k)|\,, \tag{2.6}$$

where $\boldsymbol{h}(k) = [h_x(k),\, h_y(k),\, h_z(k)\,]^T$, $\sigma = [\sigma_x,\, \sigma_y,\, \sigma_z]^T$, and σ_j are the Pauli matrices. The particle-hole redundancy introduced in BdG formulation makes sure that for any 2×2 BdG construction of this type, $h_0(k) = 0$. For the particular BdG Hamiltonian in Eq. 2.3, $h_x(k) = 0$, $h_y(k) = -\Delta \sin k$, and $h_z(k) = -t \cos k - \mu$. One can then define a unit vector $\hat{\boldsymbol{h}}(k) = \boldsymbol{h}(k)/|\boldsymbol{h}(k)|$, which lies on a unit sphere shown in Fig. 2.2. Since $h_y(-k) = -h_y(k)$ and $h_z(k) = h_z(-k)$, any position of the unit vector $\hat{\boldsymbol{h}}(k)$ at k is related by symmetry to its position at $-k$. Hence, one only needs to consider $0 \leq k \leq \pi$. The unit vector at the two extreme points takes the values:

$$\hat{\boldsymbol{h}}(0) = -\hat{z}\,, \tag{2.7a}$$

$$\hat{\boldsymbol{h}}(\pi) = \mathrm{sgn}(t - \mu)\hat{z}\,. \tag{2.7b}$$

Starting from $k = 0$, the unit vector $\hat{\boldsymbol{h}}$ is at the south pole irrespective of the nature of the topology (See Fig. 2.2). In the topologically trivial phase (*i.e.* $|\mu| > t$) the unit vector stays in the lower hemisphere for all values of k as shown in Fig. 2.2(a). In contrast to the topologically trivial phase, in topologically non-trivial phase (*i.e.* $|\mu| < t$), the unit vector starts at the south pole at $k = 0$, but as k is increased, it moves towrds the northern hemisphere, eventually ending up at the north pole at $k = \pi$ as shown in Fig. 2.2(b). At the critical point $|\mu| = t$, the unit vector is not well defined. The topological invariant can then be defined as

$$\nu = \hat{\boldsymbol{h}}(0) \cdot \hat{\boldsymbol{h}}(\pi)\,. \tag{2.8}$$

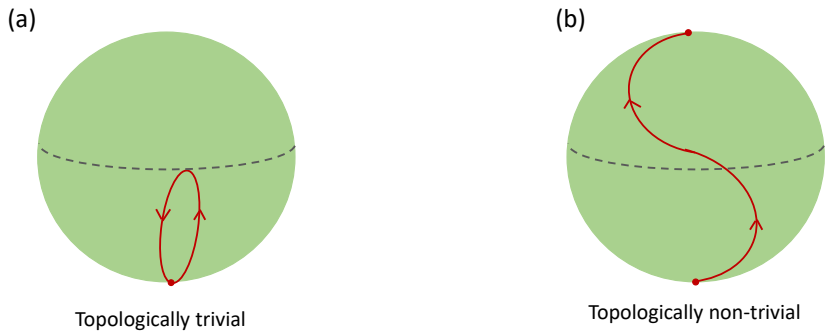

Figure 2.2: The $\mathbb{Z}_2$ topological invariant defined on the unit sphere: (a) In the trivial phase, as one moves in the Brillouine zone, the unit vector $\hat{\boldsymbol{h}}(k)$ remains in the southern hemisphere. (b) In the non-trivial phase, the unit vector $\hat{\boldsymbol{h}}(k)$ starts at the south pole at $k = 0$ and ends up at the north pole at $k = \pi$.

The topological invariant takes values $+1$ or -1 for the topologically trivial and the non-trivial phase respectively, because of this, it is called $\mathbb{Z}_2$ topological invariant [44, 45, 46, 47].

In the discussion above, we discarded half of the k-space. Such trick has a physical origin. In the BdG formulation to describe superconductivity, the Hilbert space was initially doubled by introducing the $\hat{\psi}$ operator. Discarding half of the k-space gets us back to the initially allowed number of states. Of course, the discarded space does not provide any independent information, since it is related by particle-hole transformation: $(\hat{\psi}^{\dagger}_{-k})^T = \sigma_x \hat{\psi}_k$. This makes it clear that the particle-hole symmetries in BdG Hamiltonian are redundancies created from doubling the Hilbert space. This is also one of the reason why often a Majorana mode is interpreted as half of an electron mode. The fact that the BdG transformation doubles the Hilbert space and eventually we have to get rid-off this doubling to understand the real physical effect, will reappear multiple times throughout this thesis.

Above, the use of a simple 2×2 BdG Hamiltonian allowed us to introduce $\mathbb{Z}_2$-topological invariant in an intuitive form. For a generic Hamiltonian with a

multi-component electron operator $\hat{c}_{ik}$, where index i is some finite component such as spin, orbital or layers along a finite direction of a quasi-1D structure (such as studied in next chapter), the $\mathbb{Z}_2$ invariant is calculated following a more generalized recipe [44]:

1. First skew-symmetrize the BdG Hamiltonian under the transformation

$$\tilde{\hat{\psi}}_{i,k} = U\,\hat{\psi}(k) \quad U = \frac{1}{\sqrt{2}}\begin{pmatrix} 1 & 1 \\ -i & i \end{pmatrix}, \tag{2.9}$$

   such that the transformed BdG Hamiltonian is:

$$\tilde{H}_{BdG}(k) = \begin{pmatrix} \frac{H_0(k) - H_0^*(-k) + \hat{\Delta} + \hat{\Delta}^\dagger}{2} & \frac{i[H_0(k) + H_0^*(-k) + \hat{\Delta}^\dagger - \hat{\Delta}]}{2} \\ \frac{-i[H_0(k) + H^*(-k) + \hat{\Delta} - \hat{\Delta}^\dagger]}{2} & \frac{H_0(k) - H^*(-k) - \hat{\Delta} - \hat{\Delta}^\dagger}{2} \end{pmatrix}. \tag{2.10}$$

2. The $\mathbb{Z}_2$ invariant is then defined as

$$\nu = \mathrm{sgn}[\mathrm{Pf}\,\tilde{H}_{BdG}(0)]\ \mathrm{sgn}[\mathrm{Pf}\,\tilde{H}_{BdG}(\pi)]\,, \tag{2.11}$$

   where Pf denotes the Pfaffian number, which is defined for a skew-symmetric matrix A as,

$$(\mathrm{Pf}\,A)^2 = \det(A)\,. \tag{2.12}$$

One can check the above definition reduces to Eq. 2.8 for the simple form of the BdG Hamiltonian in Eq. 2.3.

2.1.2 Majorana representation

The simple 1D-spinless superconductor model described here is the famous Kitaev chain model [44]. Kitaev solved the model in Majorana representation, giving important insights on the nature of the boundary states when the system is in topologically non-trivial regimes. In fact, the transformation U in Eq. 2.9 is also the transformation to Majorana basis. In the real space, the transformation U applied to electron creation and annihilation operators gives

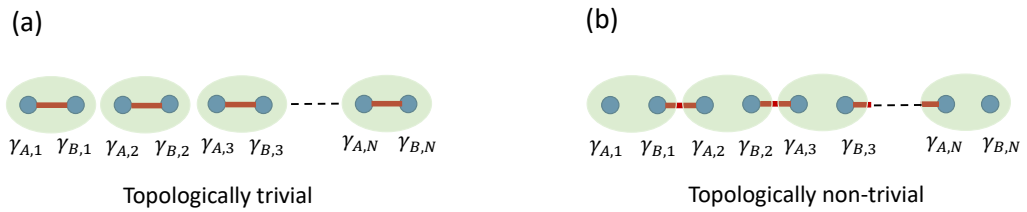

Figure 2.3: The Kiatev chain representation in the Majorana basis : The green shaded elliptical structures represent individual site of the Hamiltonian H in Eq. 2.2 represented in the electron creation-annihilation basis. The electron site is dimerized into to Majorana sites represented by blue circles. (a) In the trivial phase, the Majorana on a same site are coupled to give complex Fermions. (b) In the non-trivial phase, the Majorana at the same site are decoupled while coupling at the nearest neighbor. This leaves single unpaired Majorana at each end of the finite chain.

new operators,

$$\hat{\gamma}_{A,j} = \frac{\hat{c}_j + \hat{c}_j^\dagger}{\sqrt{2}}\,, \tag{2.13a}$$

$$\hat{\gamma}_{B,j} = -i\frac{\hat{c}_j - \hat{c}_j^\dagger}{\sqrt{2}}\,. \tag{2.13b}$$

One can identify the defining property of Majorana $\hat{\gamma}_{\alpha,j}^\dagger = \hat{\gamma}_{\alpha,j}$ above, which translates to being their own antiparticle. Additionally, they follow the anti-commutation relation:

$$\{\hat{\gamma}_{\alpha,j},\, \hat{\gamma}_{\alpha',j'}\} = 2\delta_{\alpha,\alpha'}\delta_{j,j'}\,. \tag{2.14}$$

Now, consider a finite superconducting chain with N-sites as shown in Fig. 2.3. After transforming to the Majorana basis, the Hamiltonian H in

Eq. 2.1 reads,

$$\tilde{H} = -\frac{\mu}{2}\sum_{j=1}^{N}(1 + i\gamma_{B,j}\gamma_{A,j}) \\ - \frac{i}{4}\sum_{j=1}^{N-1}[(\Delta + t)\gamma_{B,j}\gamma_{A,j+1} + (\Delta - t)\gamma_{A,j}\gamma_{B,j+1}]\,. \qquad (2.15)$$

Now, we investigate the limiting cases of the two topologically different phases discussed above in Sec. 2.1.1. Deep in the topologically trivial regime (*i.e.* $|\mu| \gg t, \Delta$), we can ignore the the second line of the Eq. 2.15. The two Majoranas $\hat{\gamma}_{A,j}$ and $\hat{\gamma}_{B,j}$ at the same lattice site j are coupled for every lattice site as shown in Fig. 2.3(a) and form a trivial complex Fermion state[1]. To fill every complex Fermion state (electronic state), one requires energy equal to the chemical potential μ, hence there are no zero energy states and the spectrum of the finite chain is fully gapped. Moreover, there is no distinctive feature of the modes at the end of the chain compared to the modes in the middle of the chain.

In the topologically non-trivial regime (*i.e.* $|\mu| < t$), for simplification of discussion, we choose $\mu \sim 0$ and $\Delta = t$. In this limit, the first and the last term on the right-hand side of the Eq. 2.15 vanish. The remaining term in the Hamiltonian couples one species of Majorana $\hat{\gamma}_{A,j}$ with the other species at neighboring site, *i.e.* $\hat{\gamma}_{B,j\pm1}$. As shown in the Fig. 2.3(b), at the each end of the chain in this limit one Majorana remains unpaired, which does not even appear in the Hamiltonian in Eq. 2.15. Because $\hat{\gamma}_{A,1}$ and $\hat{\gamma}_{B,N}$ do not appear in the Hamiltonian, they do not contribute to energy and are at exact zero energy, hence called Majorana zero modes. Here, we have chosen very specific constraints on parameters Δ, μ, and t to obtain exact solution, however, one can numerically verify these properties are unchanged for more general values as long as bulk gap does not close.

The transformation to the Majorana basis is simply a unitary transformation, generically well defined irrespective of the topological nature. Hence this

[1]Electron modes are referred to as complex Fermion and Majorana modes are referred to as real Fermion because their wavefunction is described by a real function

mathematical exercise needs to be supported by physical picture to appreciate the non-trivial nature of the physics. In a sense only the electron operators $\hat{c}$ and $\hat{c}^\dagger$ are physical. Hence, Majorana always appear in pair to describe one electron degree. Physically, the non-trivial part is the precise splitting of an electron degree into two spatially separated parts and forming a non-local electrons. A non-local complex Fermion mode written as

$$\hat{c} = \frac{\hat{\gamma}_{A,1} + i\hat{\gamma}_{B,N}}{\sqrt{2}}\,, \tag{2.16}$$

is the physical mode in the topologically non-trivial phase. This non-local electron mode can be occupied or emptied by chemical potential tuning. The non-locality and as a result of it, their robustness against local perturbations is also one of the reason for the interest in Majorana zero modes as a qubit for fault tolerant topological quantum computation [48].

Finally, the importance of spinlessness is also re-emphasized from the above exercise. A spinfull Hamiltonian will additionally double the allowed degrees of freedom at each site. In presence of small perturbations, this allows the isolated Majorana mode at each end to couple with another mode at the same end and create a localized complex Fermion mode. Since spin is present in general, the main challenge is to engineer effective spinless Hamiltonians that mimic the Kitaev's chain model. First success in this direction was achieved by proximity coupling semiconductor quantum wires with strong spin orbit coupling to an s-wave superconductor under a Zeeman field [15, 16, 17, 18, 19, 20, 21]. In the next chapter, we will get back to this problem using a different system, *i.e.* a quantum anomalous Hall system and show that one can effectively create a low energy Hamiltonian mimicking Kitaev's model. We also highlight the potential advantages that quantum anomalous Hall based Majorana device might have over the conventional spin-orbit coupled semiconductor nanowires.

2.2 Topological superconductivity in two-dimensions: chiral $p \pm ip$ wave superconductor

In this section we extend the concept of topological superconductivity to 2D. For the conceptual clarity and pedagogical comparison with 1D, we follow

similar structure of discussion as last section. As the simplest example and natural extension of the Kitaev's chain model, consider a 2D square lattice with the nearest neighbor hopping and spinless superconductivity, described by the Hamiltonian

$$H = -\mu \sum_j \hat{c}_j^\dagger c_j \; - \; \frac{t}{2} \sum_{\langle i,j \rangle} (\hat{c}_i^\dagger \hat{c}_j + h.c.) \; + \; \frac{\Delta}{2} \sum_j (\hat{c}_j \hat{c}_{j+\hat{x}} + i \hat{c}_j \hat{c}_{j+\hat{y}} + h.c.) \,, \tag{2.17}$$

where energy and length scale are normalized by the lattice constant. Here $j = n\hat{x} + m\hat{y}$, for $n, m \in \mathcal{Z}$ takes values on the lattice sites.

Following the same procedure of first transforming to the momentum space ($k_x, k_y \in [-\pi, \pi]$) followed by the BdG transformation $\hat{\psi}_{\boldsymbol{k}} = [\hat{c}_{\boldsymbol{k}}, \, \hat{c}_{-\boldsymbol{k}}^\dagger]^T$, one obtains the BdG Hamiltonian

$$H_{BdG} = \begin{pmatrix} -2t(\cos k_x + \cos k_y) - \mu & \Delta(\sin k_y - i \sin k_x) \\ \Delta(\sin k_y + i \sin k_x) & 2t(\cos k_x + \cos k_y) + \mu \end{pmatrix} , \tag{2.18}$$

and the spectrum

$$E_\pm(\boldsymbol{k}) = \pm \sqrt{\Delta^2(\sin^2 k_x + \sin^2 k_y) + [2t(\cos k_x + \cos k_y) + \mu]^2} \,. \tag{2.19}$$

As one continuously tunes the chemical potential μ from a large negative value to a large positive value, the gap first closes when $\mu = -4t$ at Γ-point in $\boldsymbol{k}$-space [shown in Fig. 2.4(b)], next when $\mu = 0$, the gap closes at X and Y-points [shown in Fig. 2.4(d)], and finally when $\mu = 4t$ the gap closes at M-point [shown in Fig. 2.4(f)]. When the chemical potential is below $-4t$ or above $4t$, the band is either completely empty or completely filled respectively, and the system is topologically trivial. Topologically it is same as vacuum, since one can take an extreme limit of $\mu \to \pm\infty$ without closing the gap. In the limit $|\mu| < 4t$, the system can be in topologically non-trivial state. One can immediately notice the similarity of this argument with the 1D case of Kitaev chain, where the topological phase transitions happen when the chemical potential coincides at the band edge. One difference being the presence of extra gap closing point $\mu = 0$ in this case, which we study in detail next.

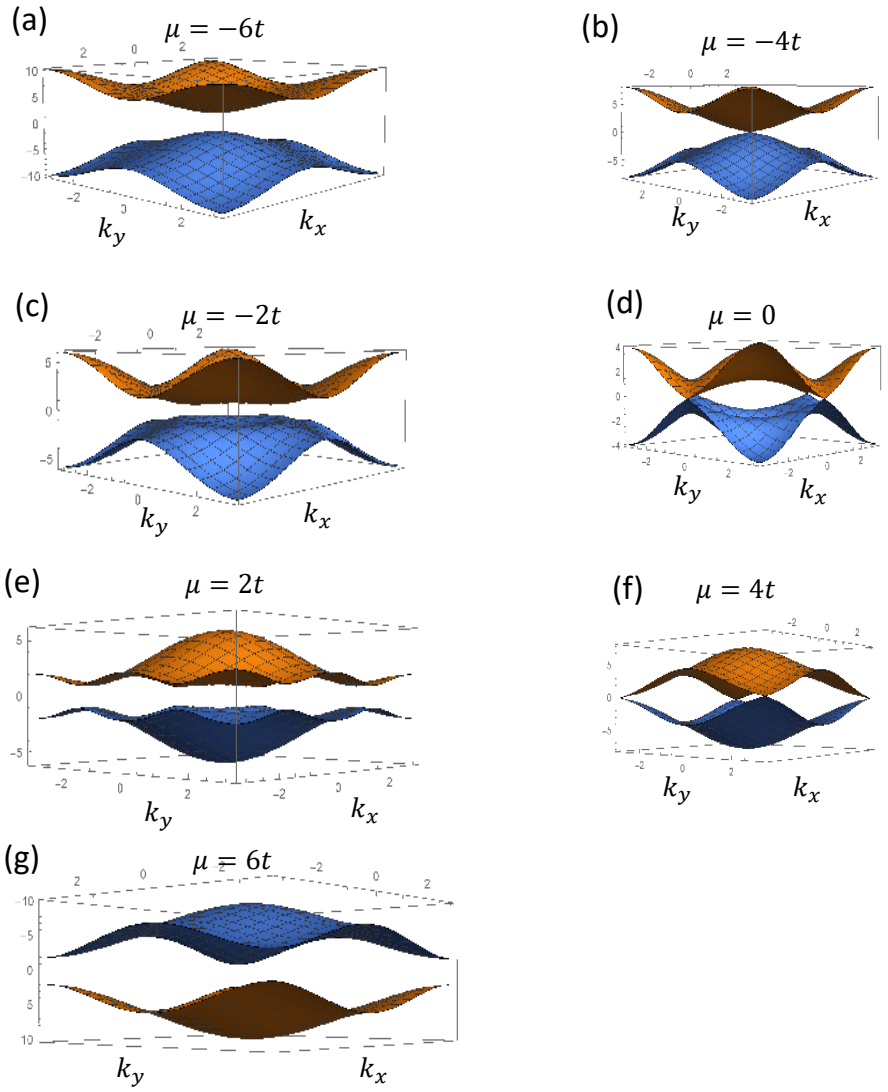

Figure 2.4: The Spectrum of a square lattice model for a 2D spinless superconductor as chemical potential μ is tuned: (a) When $\mu = -6t$, the gapped system is topologically trivial, (b) at $\mu = -4t$, Dirac gap closing occurs at Γ point, (c) when $-4t < \mu < 0$, spectrum is gapped and topologically non-trivial, (d) at $\mu = 0$, Dirac gap closing occurs at X and Y points, (e) when $0 < \mu < 4t$, spectrum is gapped and changes the topological character but still is non-trivial, (f) at $\mu = 4t$, Dirac gap closing occurs at M points, (g) when $\mu > 4t$, the gapped system is topologically trivial.

2.2.1 $\mathbb{Z}$-Topological invariant

To understand the nature of the topological invariant, we again project the BdG Hamiltonian over the Pauli matrices, $H_{BdG} = \boldsymbol{h}(\boldsymbol{k}) \cdot \boldsymbol{\sigma}$, and define the the unit vector $\hat{\boldsymbol{h}}(\boldsymbol{k}) = \boldsymbol{h}(\boldsymbol{k})/|\boldsymbol{h}(\boldsymbol{k})|$ mapping from Brillouine zone to the unit sphere, where

$$\boldsymbol{h}(\boldsymbol{k}) = [h_x(\boldsymbol{k}),\, h_y(\boldsymbol{k}),\, h_z(\boldsymbol{k})]^T\,, \tag{2.20a}$$

$$h_x(\boldsymbol{k}) = \Delta \sin k_y\,, \quad h_y(\boldsymbol{k}) = \Delta \sin k_x\,,$$

$$h_z(\boldsymbol{k}) = -2t(\cos k_x + \cos k_y) - \mu\,. \tag{2.20b}$$

The topological invariant is the integral of the solid angle subtended by the unit vector $\hat{\boldsymbol{h}}(\boldsymbol{k})$ on the unit sphere over the entire Brillouine zone and normalized to 4π (the solid angle subtended over the entire sphere), *i.e.*,

$$N = \frac{1}{4\pi} \int d\boldsymbol{k}\, \hat{\boldsymbol{h}}(\boldsymbol{k}) \cdot \left(\frac{\partial \hat{\boldsymbol{h}}(\boldsymbol{k})}{\partial k_x} \times \frac{\partial \hat{\boldsymbol{h}}(\boldsymbol{k})}{\partial k_y} \right). \tag{2.21}$$

We show in the App. A for a general 2×2 Hamiltonian on a torus, the above definition of the topologically invariant is just the Chern number of the valence band wave-function often used for non-interacting electronic system. In the particle-hole symmetric BdG Hamiltonian, it is simply the Chern number of the wavefunction of the Bogoliubov quasiparticle below zero energy. The major difference here is that the BdG Hamiltonian is in electron-hole basis with a doubled Hilbert space. Taking the similarity with the non-interacting electron system further, the topological invariant N here also counts number of chiral edge states, which is an integer, hence called integer-$\mathbb{Z}$ invariant. However, the nature of these edge states is dramatically different from the non-interacting case. We study these properties next.

Region I ($\mu < -4t$, topologically trivial)- As discussed above, in this region the system is topologically equivalent to a completely empty state, hence trivial. However, it is worthwhile to understand this from the Berry curvature (or the solid angle in the integrand of Eq. 2.21) computation. Deep in this region ($\mu \ll -4t$), as shown in the Fig. 2.5(a), the contribution to the Berry curvature coming from the vicinity of every high symmetry point is equal in

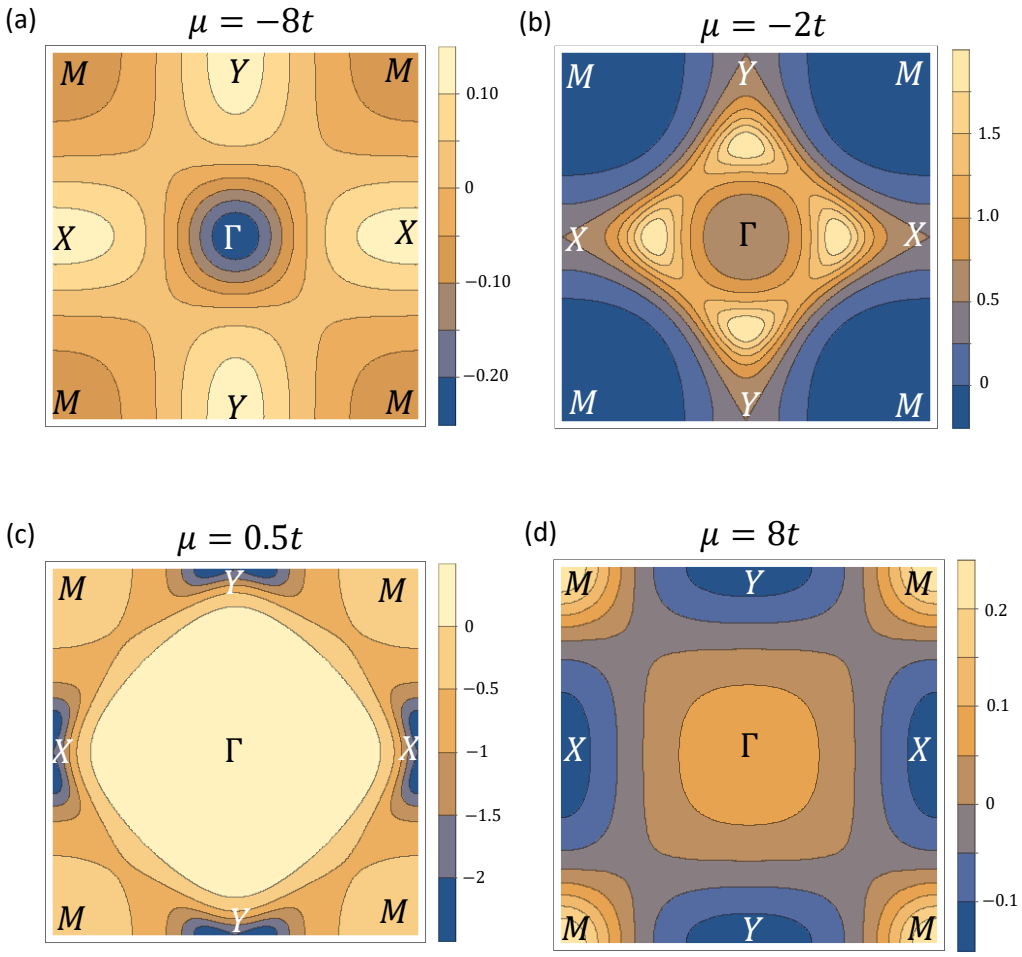

Figure 2.5: The Berry curvature of the Bogoliubov quasiparticle state below zero energy of the Hamiltonian in Eq. 2.18, in different gapped regions as μ is tuned: (a) When $\mu < -4t$, system is topologically trivial and the integral of the Berry curvature over the entire Brillouine zone vanishes. (b) After gap closing at $\mu = -4t$ and re-opening in the region $-4t < \mu < 0$, the Berry curvature contribution in the vicinity of Γ point changes sign. (c) After gap closing at $\mu = 0$, in the region $0 < \mu < 4t$, the Berry curvature contribution from X and Y points changes sign. (d) After gap closing at $\mu = 4t$ and re-opening in the region $\mu > 4t$, the system is in topologically trivial phase again, the integral of the Berry curvature over the entire Brillouine zone vanishes.

magnitude, however, the net contribution from Γ-point and M-point is canceled by the net contribution from the X and Y- point because of their opposite sign. As μ is increased to bring the system near the gap closing point, the Berry curvature near Γ-point takes very large value but also becomes concentrated near a very small region. The Berry curvature near X, Y and M-point spreads in larger Brillouine zone area but becomes smaller and more uniform in magnitude. This merely reflects the gap closing near Γ-point. Overall, the integral of Berry curvature over the entire Brillouine zone still vanishes and the $\mathbb{Z}$ topological invariant is takes the value $N = 0$.

Region II ($-4t < \mu < 0$, topologically non-trivial)- When chemical potential is increased, the first gap closing at $\mu = -4t$ occurs at Γ-point. As shown in the Fig. 2.5(a),(b), the Berry curvature contribution near Γ-point changes sign as gap closes and re-opens, the Berry curvature contribution near X, Y, and M- points remains qualitatively unchanged. Overall the $\mathbb{Z}$ topological invariant computed from Eq. 2.21 takes the value $N = 1$. To understand the effect of this sign change near the gap closing, we describe the effective low energy Hamiltonian by expanding the H_{BdG} in Eq. 2.18 near Γ-point upto linear order and substituting $\mu = -4t + \delta$,

$$H_{BdG,\Gamma} \sim \begin{pmatrix} -\delta & \Delta(k_y - ik_x) \\ \Delta(k_y + ik_x) & \delta \end{pmatrix} \tag{2.22}$$

Now we consider a setup shown in Fig. 2.6, where the region $x > 0$ is defined by above Hamiltonian, while $x < 0$ is a trivial vacuum. For the low energy Hamiltonian, we replace the momentum label k with the differential operator to obtain a real space effective Hamiltonian,

$$H_{BdG,\Gamma}(\boldsymbol{r}) \sim \begin{pmatrix} -\delta(x) & \Delta(-i\partial_y - \partial_x) \\ \Delta(-i\partial_y + \partial_x) & \delta(x) \end{pmatrix} \tag{2.23a}$$

$$\Delta(x) = \Delta\Theta(x)\,, \quad \delta(x) = \delta\Theta(x) + V(x)\,. \tag{2.23b}$$

Here $\Theta(x)$ is the Heaviside step function and $V(x)$ can model confining potential at the interface. Since, the Hamiltonian is translationally invariant in y-direction, we seek solutions of the type

$$\psi(\boldsymbol{r}) \sim \mathrm{e}^{ik_y y}[u(x),\, v(x)]^T = \mathrm{e}^{ik_y y}[f(x) + ig(x),\, f(x) - ig(x)]^T. \tag{2.24}$$

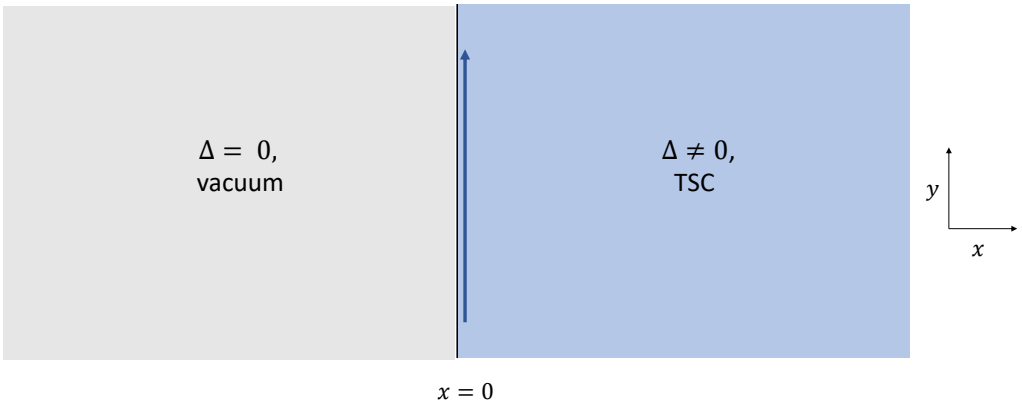

Figure 2.6: Setup showing the interface between a topological superconductor (TSC) and a trivial state: The $x > 0$ region is defined by the Hamiltonian H_{BdG} in Eq. 2.23, which is derived from low energy sector of the topologically non-trivial phase of a 2D spinless superconductor on square lattice described by the Hamiltonian in Eq. 2.17. The region on the left is vacuum. The blue arrow represents a chiral edge state.

Solutions in the energy gap, *i.e.* $|E| < \Delta$ are localized in x-direction. Here, we seek solutions localized at $x = 0$, which lie in the bulk gap. Solving the BdG equation at $x = 0^+$,

$$i[\Delta\partial_x + \delta(x)]\, f(x) = (E + \Delta k_y)\, g(x) \tag{2.25a}$$

$$i[\Delta\partial_x - \delta(x)]\, g(x) = (E - \Delta k_y)\, f(x) \tag{2.25b}$$

A solution with $\delta > 0$, that is localized at the interface $x = 0$, has energy eigenvalues,

$$E = \Delta k_y\,, \tag{2.26}$$

which from Eq. 2.25b immediately gives $g(x) = 0$, and from Eq 2.25a,

$$f(x) = f(0) \exp\left(-\frac{1}{\Delta}\int_0^x \delta(x)dx\right). \tag{2.27}$$

Since $\delta(x) > 0$, one can see that at the interface $x = 0$, this is the only localized solution. In other words, the solution obtained by eigenvalues $E = -\Delta k_y$

cannot lie at the interface $x = 0$, since it will diverge at large x. Further, under the unitary transformation,

$$\tilde{\psi}(\boldsymbol{r}) = \frac{1}{\sqrt{2}} \begin{pmatrix} 1 & 1 \\ 1 & -1 \end{pmatrix} \psi(\boldsymbol{r}) = \mathrm{e}^{ik_y y}[\sqrt{2} f(x),\, 0]^T\,, \tag{2.28}$$

the wavefunction takes only one non-zero component out of a generic two-component vector. Thus describes a chiral mode.

The presence of a single edge state in BdG Hamiltonian, which by construction has a doubled Hilbert space (due to the particle-hole redundancy) is non-trivial. Qualitatively, this again reinforces the idea of Majorana mode being equivalent to half an electron mode. The Majorana character of this edge state can be established more rigorously by writing the annihilation operator for the edge mode,

$$\hat{\psi}_{k_y} = \int dx\, dy\, [\mathrm{e}^{ik_y y} u(x) \hat{c}_{k_y} + \mathrm{e}^{ik_y y} v(x) \hat{c}^\dagger_{-k_y}]\,. \tag{2.29}$$

Since we have shown that $u(x) = v(x) = f(x)$ is purely real,

$$\hat{\psi}_{k_y} = \hat{\psi}^\dagger_{-k_y} = \int dx\, dy\, [\mathrm{e}^{ik_y y} f(x) \hat{c}_{k_y} + \mathrm{e}^{ik_y y} f(x) \hat{c}^\dagger_{-k_y}]\,. \tag{2.30}$$

This is precisely the relation the Majorana creation and annihilation operators obey.

If one changes the sign of $\delta(x)$, using Eq. 2.25, one can see that the state localized at $x = 0$ interface must have energy solutions $E = -\Delta k_y$. This implies that $f(x) = 0$ and $g(x)$ takes the non-zero values. The localized in-gap wavefunction must be obtained from Eq. 2.25b. This is just a solution with the opposite chirality. In other words, changing the sign of the diagonal entry in the low energy effective Hamiltonian in Eq. 2.22 changes the chirality of the edge state. One would expect presence of an edge state with opposite chirality at $x = 0$ interface when $\delta < 0$. However, $\delta < 0$ corresponds to the topologically trivial region I discussed above, and argued that it does not have an edge state. Here, we digress a little to discuss a possible source of confusion while working with effective low energy Hamiltonians. A careful calculation reveals that a general low energy massive Dirac Hamiltonian similar

to Eq. 2.22 only contributes $\pm 1/2$ to chirality depending on the sign of the mass term (coefficient of σ_z Pauli matrix). The only physical quantity is the difference in the chirality between the phases with the two opposite signs of mass term, which is conveniently ± 1 [49]. This simply means that the effective low energy Hamiltonian has a chiral edge state for one of the sign of mass term and no chiral edge state for the opposite sign of the mass term. The possible confusion can be resolved when one considers the fact that the low energy Hamiltonian is derived from some lattice Hamiltonian of the type in Eq. 2.18. As we discussed earlier the contribution to Chern number from other high symmetry points X, Y and M which are at higher energy (upto a sign) cancel precisely the contribution from the low energy part near Γ-point. In terms of edge state, it means that any chiral edge state that might be indicated by the low energy effective Hamiltonian when $\delta < 0$, is gapped out due to overlap with an edge state with opposite chirality present because of the contributions coming from higher energy. Overall, $\delta < 0$ does not have a chiral edge state, while $\delta > 0$ has a chiral edge state.

In general a low energy massive Dirac Hamiltonian is the simplest Hamiltonian in 2D that allows topological phase transition. One can choose the phase with one sign of mass term as topologically non-trivial with a chiral edge state and consequently the phase with the opposite sign of mass term is topologically trivial. We use this convention repeatedly throughout this thesis. At a deeper level, this consideration is ensured by contribution to topology from high energy points in the well regularized lattice Hamiltonian. A well regularized calculation of the Berry curvature requires computation over the full Brillouine zone, which is compact [49].

Region III ($0 < \mu < 4t$, topologically non-trivial)- When chemical potential μ is further increased, the next gap closing occurs at $\mu = 0$ at X and Y-points as shown in Fig. 2.4 (d). At this gap closing and the subsequent re-opening the contribution to the Chern number near Γ-point is qualitatively unchanged, while contribution near X and Y-points changes sign. Overall the $\mathbb{Z}$ topological invariant takes the value $N = -1$ in this phase.

The change in the nature of the edge state can be understood from the effective low energy Hamiltonian near the X-point,

$$H_{BdG,X} \sim \Delta k_y \sigma_x \, - \, \Delta k_x \sigma_y \, - \, \mu \sigma_z \, , \tag{2.31}$$

and near Y-point,

$$H_{BdG,Y} \sim -\Delta k_y \sigma_x + \Delta k_x \sigma_y - \mu \sigma_z \,. \tag{2.32}$$

Following a procedure similar to the one performed near Γ-point above, we can see that as the gap closes and re-opens, chiral edge states appear from the low energy sector near X and Y points. These new chiral edge states have chirality opposite to the chiral edge state coming from the Γ-point sector discussed above. Since the total contribution from X and Y points is twice the contribution from the Γ point, one of the new chiral edge state cancels the Γ-point edge state and the remaining one chiral edge state of the chirality opposite to the phase in region II ensures the overall change in sign of the topological invariant. Thus $N = -1$ in this region.

Region IV ($\mu > 4t$, topologically non-trivial)- The final gap closing occurs at M-point when chemical potential $\mu = 4t$ as shown in Fig. 2.4 (f). On the other side of this gap closing point the Berry curvature changes sign near M-points. Similar to the region I, the Berry curvature contribution near Γ-point and M-point combines to cancel the contribution near X and Y points. Overall, this phase is topologically trivial with no edge states.

2.3 Quantum anomalous Hall proximity coupled to s-wave superconductor

In this section, we consider a model quantum anomalous Hall Hamiltonian, proximity coupled to an s-wave superconductor and show the presence of topological superconductivity with the non-zero $\mathbb{Z}$-topological index [25].

The simplest low energy Hamiltonian that allows quantum anomalous Hall effect is a massive Dirac Hamiltonian in two dimensions (we consider a more realistic Hamiltonian for this effect in Chapter 3, Sec. 3.1),

$$H_D(\boldsymbol{k}) = \lambda \sigma_z + \hbar v_F (k_y \sigma_x + k_x \sigma_y) \,, \tag{2.33}$$

written in the basis $\hat{C}_{\boldsymbol{k}} = [\hat{c}_{\boldsymbol{k},\uparrow}, \hat{c}_{\boldsymbol{k},\downarrow}]$ and the Pauli matrices σ operate on spin. Here v_F is the Fermi velocity and the Dirac mass term λ in real system models the magnetic order.

The Hamiltonian is similar to the effective low energy H_{BdG} in Eq. 2.22. The only difference is the representation basis, which changes the nature of the edge state. As we have already discussed for Hamiltonian of this type, when $\lambda = 0$ the spectrum becomes gapless with Dirac crossing at $\boldsymbol{k} = 0$. Topologically, the either sides *i.e.* $\lambda > 0$ and $\lambda < 0$ are distinct. In this scenario we take $\lambda > 0$ as the topologically non-trivial phase and $\lambda < 0$ as topologically trivial. The topologically non-trivial phase has a chiral edge state. However, because the basis of the above Hamiltonian is electrons with opposite spin, the edge state is an electronic edge state, carrying quantized Hall conductance. Overall, the phase $\lambda > 0$ is a Chern insulator, with Chern number $C = 1$ and quantized Hall conductance. The phase $\lambda < 0$ is a trivial insulator[2].

We consider a scenario where a normal 2DES, which is described by the Hamiltonian H_D in Eq. 2.33, is proximity coupled to an s-wave superconductor. The proximity coupled system at the mean field level is described by the BdG Hamiltonian [25],

$$H_{BdG} = \begin{pmatrix} H_D(\boldsymbol{k}) & \hat{\Delta} \\ \hat{\Delta}^\dagger & -H_D^*(-\boldsymbol{k}) \end{pmatrix}, \tag{2.34}$$

where $\hat{\Delta} = i\Delta\sigma_y$, and the BdG Hamiltonian is written in the basis $\hat{\psi}_{\boldsymbol{k}} = [\hat{c}_{\boldsymbol{k},\uparrow}, \hat{c}_{\boldsymbol{k},\downarrow}, \hat{c}^\dagger_{-\boldsymbol{k},\uparrow}, \hat{c}^\dagger_{-\boldsymbol{k},\downarrow}]^T$. Under the unitary transformation

$$U = \frac{1}{\sqrt{2}} \begin{pmatrix} 1 & 0 & 0 & 1 \\ 0 & 1 & 1 & 0 \\ 1 & 0 & 0 & -1 \\ 0 & 1 & -1 & 0 \end{pmatrix}, \tag{2.35}$$

the BdG Hamiltonian transforms to a block diagonal form

$$\tilde{H}_{BdG} = U\, H_{BdG}\, U^{-1} = \begin{pmatrix} H_U & 0 \\ 0 & H_D \end{pmatrix}, \tag{2.36}$$

[2]Here the assumption is that for $\lambda < 0$, the contribution from higher energy high symmetry point ensure the topologically trivial insulator instead of Chern insulator of opposite chirality

where,

$$H_U = \begin{pmatrix} \Delta + \lambda & \hbar v_F(k_y - ik_x) \\ \hbar v_F(k_y + ik_x) & -\Delta - \lambda \end{pmatrix}, \tag{2.37a}$$

$$H_D = \begin{pmatrix} \lambda - \Delta & \hbar v_F(k_y - ik_x) \\ \hbar v_F(k_y + ik_x) & -\lambda + \Delta \end{pmatrix}, \tag{2.37b}$$

are two massive Dirac Hamiltonians with Different mass terms. This form is the most convenient way to understand the topological superconducting phase in close analogy to the discussion in Sec. 2.2.1.

2.3.1 Topological Phase diagram

The topologically non-trivial phase for a massive Dirac Hamiltonian is chosen to be the one with positive mass term. The topological characterization of $\tilde{H}_{BdG}$ obtained from Eq. 2.36 and Eq. 2.37 simply follows by adding topological invariants of the diagonal blocks H_U and H_D. We consider $\Delta > 0$ to be fixed and tune λ. The possible topological phases are characterized as follows [25]:

1. Region I ($\lambda > \Delta > 0$)- In this regime the bulk spectrum is gapped and the mass term in both H_U and H_D is positive. Hence both blocks are in their topologically non-trivial phase. Since both H_U and H_D have same chirality, the $\mathbb{Z}$ topological index takes the value $N = N_U + N_D = 2$, which is obtained by adding unit contribution from each block. The system has two chiral edge state, each block contributing one. This phase is topologically equivalent[3] to the normal quantum anomalous Hall effect, since the quantum anomalous Hall Hamiltonian in the limit $\Delta \to 0$ can be achieved without closing the bulk gap.

2. Region II ($-\Delta < \lambda < \Delta, \Delta > 0$) As λ is decreased, H_D has Dirac gap closing when $\lambda = \Delta$ as shown in Fig. 2.7. On the other side, when

[3]When $\Delta \neq 0$ the system here is not in quantum anomalous Hall phase, because it does not have quantized Hall conductance. However, it is topologically equivalent to quantum anomalous Hall phase, since the BdG quasiparticle wavefunction below zero energy have the same Chern number.

$\lambda < \Delta$, the gap reopens, and H_D has gone under topological phase transition and is in its trivial phase. As long as $\lambda > -\Delta$, H_U is still under its topologically non-trivial phase. In this regime $\mathbb{Z}$ index only has contribution from H_U and hence $N = 1$. This phase is topologically distinct from quantum anomalous Hall phase but similar to the model spinless p-wave superconductor in its topologically non-trivial phase (*i.e.* $-4t < \mu < 0$) discussed in Sec. 2.2.

3. Region III ($\lambda < -\Delta, \Delta > 0$)- As λ is further decreased, H_U has Dirac gap closing when $\lambda = -\Delta$ as shown in Fig. 2.7. On the other side, H_U has undergone topological phase transition and is in trivial phase. Overall, both H_U and H_D are trivial in this phase and system overall is trivial with no chiral edge states.

2.3.2 Edge state picture

The different topological phases can also be understood from the edge picture. This highlights the nature of edge states. In particular shows the presence of an isolated chiral Majorana edge mode when $N = 1$. In the $N = 2$ phase, both H_U and H_D block contribute one chiral edge state of the same chirality. The transformed Hamiltonian $\tilde{H}_{BdG}$ acts in the basis

$$\hat{\tilde{\psi}}_{\boldsymbol{k}} = U\,\hat{\psi}_{\boldsymbol{k}} = [\hat{\alpha}_{\boldsymbol{k}},\, \hat{\alpha}^{\dagger}_{-\boldsymbol{k}},\, \hat{\beta}_{\boldsymbol{k}},\, \hat{\beta}^{\dagger}_{-\boldsymbol{k}}]^T\,, \tag{2.38}$$

where

$$\hat{\alpha}_{\boldsymbol{k}} = \frac{\hat{c}_{\boldsymbol{k},\uparrow} + \hat{c}^{\dagger}_{-\boldsymbol{k},\downarrow}}{\sqrt{2}}\,, \qquad\qquad \hat{\beta}_{\boldsymbol{k}} = \frac{\hat{c}_{\boldsymbol{k},\uparrow} - \hat{c}^{\dagger}_{-\boldsymbol{k},\downarrow}}{\sqrt{2}}\,. \tag{2.39}$$

The annihilation operator for each chiral edge state in $N = 2$ takes the form

$$\hat{\phi}_U(k_y) = \int dx\, dy\, \mathrm{e}^{ik_y y}\mathrm{e}^{-\frac{\lambda+\Delta}{\hbar v_F}x}(\hat{\alpha}_{k_y} + \hat{\alpha}^{\dagger}_{-k_y})\,, \tag{2.40a}$$

$$\hat{\phi}_D(k_y) = \int dx\, dy\, \mathrm{e}^{ik_y y}\mathrm{e}^{-\frac{\lambda-\Delta}{\hbar v_F}x}(\hat{\beta}_{k_y} + \hat{\beta}^{\dagger}_{-k_y})\,, \tag{2.40b}$$

which clearly follow the relation for the chiral Majorana modes. Hence, the two edge states in $N = 2$ superconductor are simply two chiral Majorana

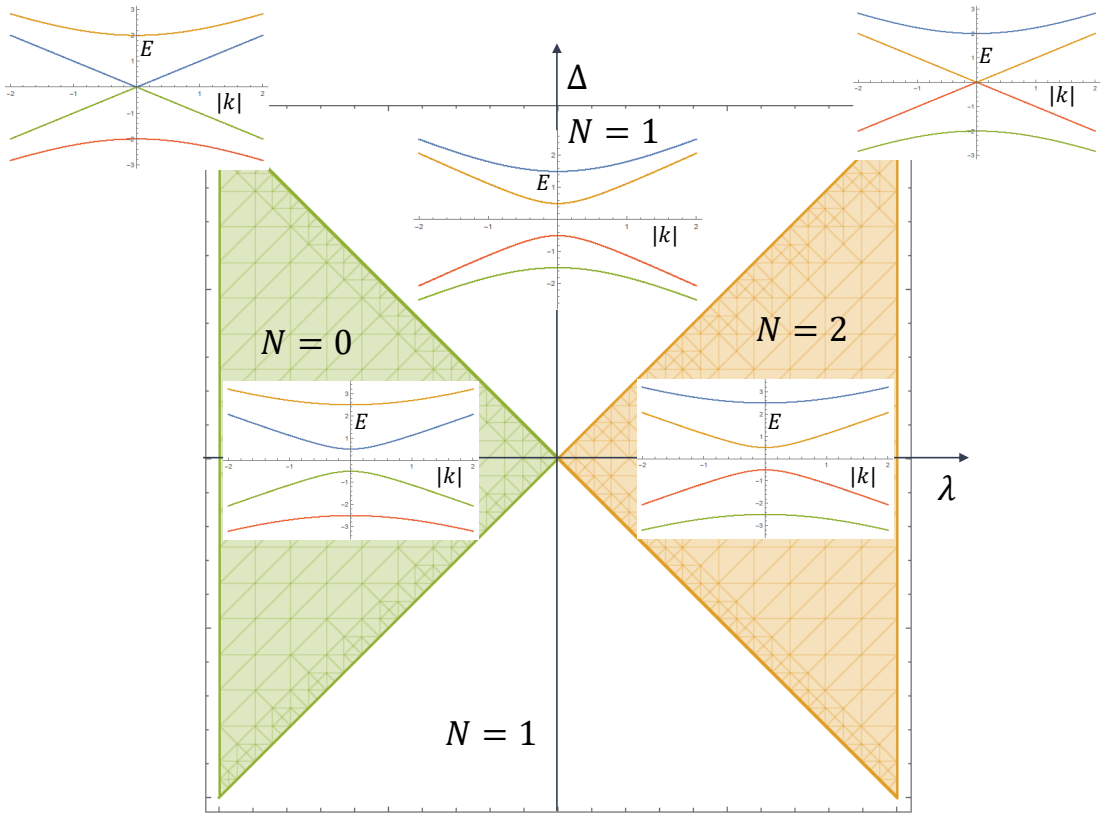

Figure 2.7: Topological phase diagram of a model QAH Hamiltonian proximity coupled to an s-wave superconductor: The axes represent superconducting pairing strength Δ and the mass term λ in the model quantum anomalous Hall Hamiltonian. The inset shows a typical bulk phase diagram in the respective topological phase. Dirac crossings appear at the boundary between two topologically distinct phases. topological superconducting phases with $N = 1$ and $N = 2$ are present.

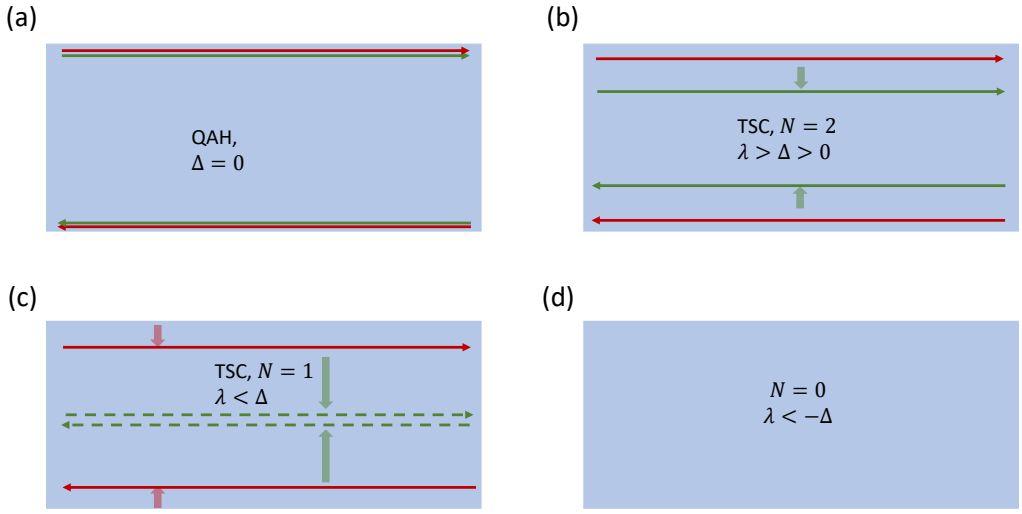

Figure 2.8: The edge state picture of a quantum anomalous Hall (QAH) proximity coupled to an s-wave superconductor: (a) In the limit of $\Delta \to 0$, the system is in quantum anomalous Hall phase with quantized Hall conductance carried by a single chiral electron edge state. However in the BdG doubled picture it is represented by two identical chiral Majorana edge modes. (b) As Δ is tuned in, the two chiral Majorana edge modes cease to be identical and one of them moves away from edge faster than the other owning to different exponential decay coefficient. (c) As $\lambda < \Delta$, one of the chiral Majorana edge mode is well in the bulk and due to avoided crossing from the strong overlap of its counterpart at the opposite edge, is gapped out at higher energy. Only single Majorana edge mode survives. (d) As $\lambda < -\Delta$, the other Majorana edge mode also goes into bulk and is gapped out by overlap from its counterpart at the other edge. The system becomes completely trivial with no chiral edge state.

edge modes of same chirality. Of course, this is nothing unexpected from the discussion in the previous section. Topologically, the phase with two chiral Majorana edge modes is identical to the quantum anomalous Hall phase. The simplest way to understand this is to recall that the Hamiltonian $\tilde{H}_{BdG}$ is under BdG doubled formulation. Hence two chiral Majorana states simply combine to give a single chiral edge state of complex fermion.

It is important to note that for a non-zero Δ, the two chiral Majorana modes are not identical. Instead, the extent of localization along x-direction differs as shown pictorially in Fig. 2.8(b). As λ is decreased, $\hat{\phi}_D$ mode spreads faster than $\hat{\phi}_U$ mode, and completely merges into bulk at $\lambda = \Delta$ by overlapping with its counterpart from the opposite edge as shown in Fig. 2.8(c).

Finally, at $\lambda = -\Delta$ the chiral mode $\hat{\phi}_U$ also merges in the bulk and the system becomes topologically trivial with no chiral edge states.

In conclusion, we have first established the simple model BdG Hamiltonian in 1D and 2D that can exhibit topological phase transitions and shown that the non-trivial region has boundary states whose creation and annihilation obey Majorana properties. We have then reviewed an earlier work [25], which demonstrates the topological superconducting phase for the simplest model Hamiltonian with the Chern insulator properties. More precisely, when a normal system with properties of the quantum anomalous Hall effect is proximity coupled to an s-wave superconductor, it can host topological superconducting phase with chiral Majorana edge modes. The phase with odd number of chiral Majorana edge modes (*i.e.* $N = \pm 1$) is of particular interest from the point of view of experiment, since it gives a distinct transport signature [50, 26]. In the remaining part of this thesis, the focus is on studies the above mentioned topological superconducting phases in detail, considering more realistic Hamiltonians to describe the Chern insulator phase.

Chapter 3

One-dimensional topological superconductivity and Majorana zero modes in quantum anomalous Hall based system

In this chapter[1] we study the quantum anomalous Hall system proximity coupled to an s-wave superconductor in more details. In chapter 2, we showed that when a model quantum anomalous Hall Hamiltonian (*i.e.* a single massive Dirac Hamiltonian written in the electron spin basis) is proximity coupled to an s-wave superconductor under appropriate conditions has a region of $\mathcal{T}$-symmetry broken topological superconducting phase.

We first consider a more realistic two layer model for the quantum anomalous Hall system. Experimentally, the quantum anomalous Hall effect is observed in magnetically doped thin films of a 3D TI such as Bi_2Se_3 [8, 51, 26]. The quantum anomalous Hall effect in this system can be explained by two coupled massive Dirac Hamiltonians, describing the two surface states [52, 53, 54]. We first study the topological phases of the bilayer model when it is proximity coupled to an s-wave superconductor in 2D. The continuum model of this system is already studied by Wang *et. al.* [50]. We extend the bilayer model on a lattice and consider its quasi 1D limit (when $L \gg W$). In the quasi 1D limit, we show that when the normal part is in its quantum anomalous Hall phase, the proximity coupled system mimics the low energy Hamiltonian of the Kitaev chain model, and in its non-trivial phase, has Majorana zero

[1]This chapter is partly based on the research article: Yongxin Zeng, Chao Lei, Gaurav Chaudhary, and Allan H. MacDonald, *Quantum anomalous Hall Majorana platform*, Phys. Rev. B **97**, 081102(R). Gaurav Chaudhary contributed to analytical results, analysis of the numerical results, discussion, and the manuscript writting. Parts of the text and some of the figures are reproduced from the above mentioned article.

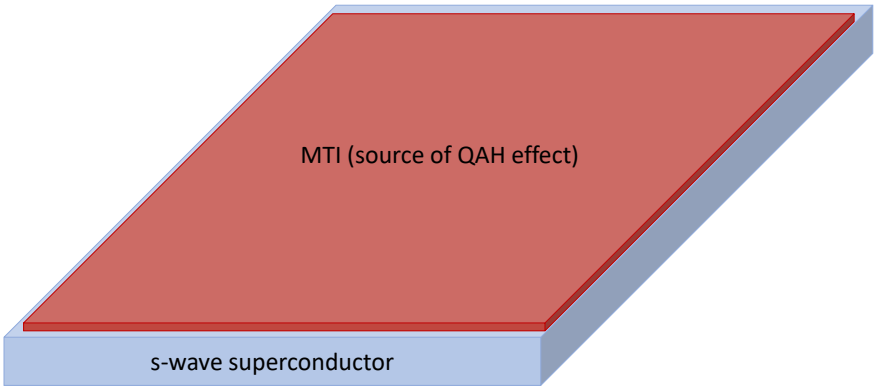

Figure 3.1: Thin film of a 3D magnetic TI (MTI) proximity coupled to an s-wave superconductor: When magnetic dopants are in ordered phase, the magnetic TI can exhibit quantum anomalous Hall (QAH) phase.

modes at the end [27]. Furthermore, the phase diagram of this coupled system has particularly broad regions of stability for both topologically trivial and non-trivial phases. We show such quasi 1D structures behave effectively as topological Kitaev chain. Experimentally quasi 1D structures can be defined via electrostatic gates on the parent 2D system. We also argue in favor of this design based on 1D structures on a base 2D system to be favorable for braiding and manipulating Majorana zero modes.

3.1 Model

Our model is motivated by Cr-doped Bi_2Se_3 thin films in which proximitized superconductivity has already been demonstrated experimentally [8, 26] , and which are close to the magnetic TI's, quantum anomalous Hall insulator-normal insulator phase boundary when 4-6 quintuple layers thick. A model setup is presented pictorially in Fig. 3.1. When written in the basis

$$\hat{C}_{\boldsymbol{k}} = [\hat{c}^t_{\boldsymbol{k},\uparrow}, \hat{c}^t_{\boldsymbol{k},\downarrow}, \hat{c}^b_{\boldsymbol{k},\uparrow}, \hat{c}^b_{\boldsymbol{k},\downarrow}]^T , \tag{3.1}$$

where $\hat{c}^s_{\boldsymbol{k}\sigma}$ annihilates an electron with momentum $\boldsymbol{k}$, spin $\sigma =\uparrow,\downarrow$ at surface $s = t/b$ (top/bottom), the effective low energy single particle Hamiltonian of the magnetic TI thin film at energies below the bulk gap is

$$H_0^{\text{eff}}(\boldsymbol{k}) = h_{\text{D}}(\boldsymbol{k})\,\sigma_0 \otimes \tau_z + m_k\,\sigma_0 \otimes \tau_x + \lambda\,\sigma_z \otimes \tau_0 + \lambda'\,\sigma_0 \otimes \tau_z\,. \tag{3.2}$$

Here all the length scales in the Hamiltonian are normalized by the lattice constant. The Pauli matrix τ_i acts on the surface and σ_i on the spin. In Eq. 3.2, $h_{\text{D}}(\boldsymbol{k}) = \hbar v_F(k_y\sigma_x - k_x\sigma_y)$ is the 2D Dirac Hamiltonian with Fermi velocity v_F, which describes the surface state of a thin film TI without the magnetic dopants; $m_k = m_0 + m_1(k_x^2 + k_y^2)$ accounts for hybridization between the top and the bottom surfaces, the effect of magnetic dopants is considered by including the mass term λ, which models an effective exchange field produced by the ferromagnetically ordered magnetic dopants; and λ' accounts for the energetic displacement between Dirac cones on the top and the bottom surfaces produced by vertical electric fields in the bulk of the TI. Later, in Sec. 3.3, we show that λ' is an important tuning knob for topological phases. As already discussed in chapter 2, when placed in proximity to an s-wave superconductor, the system is described by the BdG Hamiltonian $H(\boldsymbol{k}) = 1/2\sum_{\boldsymbol{k}} \hat{\psi}^\dagger_{\boldsymbol{k}} H_{\text{BdG}}(\boldsymbol{k})\hat{\psi}_{\boldsymbol{k}}$, where

$$H_{\text{BdG}}(\boldsymbol{k}) = \begin{pmatrix} H_0^{\text{eff}}(\boldsymbol{k}) - \mu & \hat{\Delta} \\ \hat{\Delta}^\dagger & -[H_0^{\text{eff}}(-\boldsymbol{k})]^* + \mu \end{pmatrix}, \tag{3.3}$$

with

$$\hat{\Delta} = \begin{pmatrix} i\Delta_t\sigma_y & 0 \\ 0 & i\Delta_b\sigma_y \end{pmatrix}, \tag{3.4}$$

and

$$\hat{\psi}_{\boldsymbol{k}} = [\hat{c}^t_{\boldsymbol{k}\uparrow},\, \hat{c}^t_{\boldsymbol{k}\downarrow},\, \hat{c}^b_{\boldsymbol{k}\uparrow},\, \hat{c}^b_{\boldsymbol{k}\downarrow},\, \hat{c}^{t\dagger}_{-\boldsymbol{k}\uparrow},\, \hat{c}^{t\dagger}_{-\boldsymbol{k}\downarrow},\, \hat{c}^{b\dagger}_{-\boldsymbol{k}\uparrow},\, \hat{c}^{b\dagger}_{-\boldsymbol{k}\downarrow}]^T\,. \tag{3.5}$$

Since the lattice constant is absorbed into the wavevectors in Eq. 3.2 to make them dimensionless, the terms m_0, m_1 and $\hbar v_F$ all have dimensions of energy.

One can obtain realistic values of v_F, m_0 and m_1 by comparing the model spectrum with density-functional theory (DFT) band structures of Bi_2Se_3

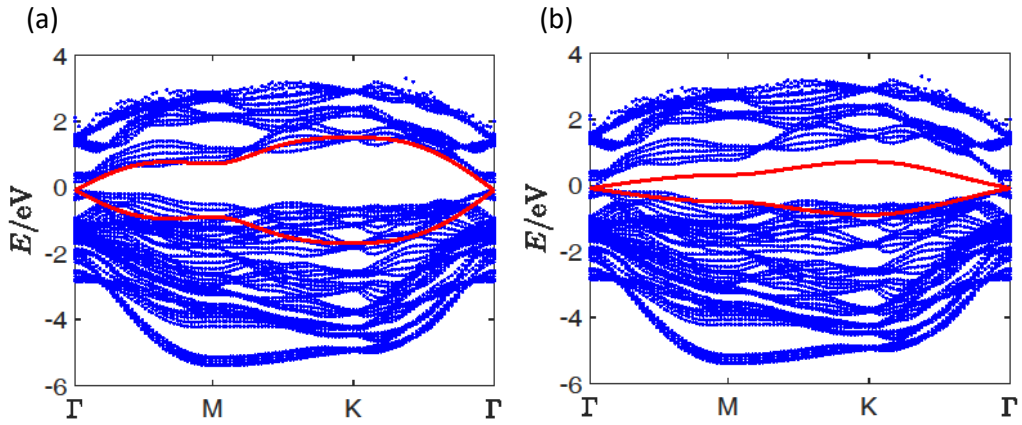

Figure 3.2: Band-structure of a 5-layer Bi_2Se_3 thin film : Blue dots are from DFT calculation, while red curves are from our effective lattice model when we choose $m_0 = 6$ meV and (a) $m_1 = 0.2$eV, $\hbar v_F = 0.7$eV, which coincide with matching lowest conduction band; (b) $m_1 = 0.1$eV, $\hbar v_F = 0.2$eV, which coincides by matching highest valence band. Figure reproduced from the article Phys. Rev. B **97**, 081102(R).

shown in Fig. 3.2. For a five-layer film one finds that the gap at Γ-point is about 12 meV, giving $m_0 = 6$ meV. Rough estimates for m_1 and v_F can be obtained by fitting to the DFT Dirac velocity v_F ($\sim 4 \times 10^5$m/s) and the DFT gaps at M and K points. By matching the lowest DFT conduction band with the upper band in our model, we find that $m_1 \sim 0.2$ eV and $\hbar v_F \sim 0.7$ eV as shown in Fig. 3.2(a). Notice that matching the highest DFT valence band with the lower band in our model gives different value of v_F as shown in Fig. 3.2(b). However, our main findings on topological robustness are independent of upper or lower band Fermi velocity as long as v and m_1 remains on larger energy scale compared to m_0 for a lattice model with lattice constant $a \approx 4$Å.

3.1.1 Lattice regularization

A regularized square-lattice version of Eq. 3.2 with nearest neighbor hopping [55] accurately and conveniently captures the physics of the topological phase transitions at the surface of the magnetic TI. Since later in this chapter our focus is on quasi 1D structures of the system discussed above, here we construct an underlying lattice model for the normal part described by Eq. 3.2. In the lattice model $k_{x/y}$ is replaced by $\sin k_{x/y}$ and k^2 by $2(2-\cos k_x-\cos k_y)$. We can rewrite the momentum-space Hamiltonian in the following form:

$$H_0(\boldsymbol{k}) = h_0 + (h_x e^{ik_x} + h_y e^{ik_y} + h.c.)\,. \tag{3.6}$$

Then we obtain a nearest-neighbor tight-binding model, where the on-site term is given by the matrix

$$h_0 = (m_0 + 4m_1)\,\sigma_0 \otimes \tau_x + \lambda\,\sigma_z \otimes \tau_0 + \lambda'\,\sigma_0 \otimes \tau_z\,, \tag{3.7}$$

and the hopping terms in x and y directions are given by the matrices

$$h_x = -\frac{i}{2}\hbar v_F\,\sigma_x \otimes \tau_0 - m_1\,\sigma_0 \otimes \tau_x\,, \tag{3.8a}$$

$$h_y = \frac{i}{2}\hbar v_F\,\sigma_y \otimes \tau_0 - m_1\,\sigma_0 \otimes \tau_x\,. \tag{3.8b}$$

To physically picture this lattice model with nearest neighbor hopping, one can imagine each atomic site having four orbitals: two of which are electron spin and two are layers. At small wave-vectors

$$H_0(\boldsymbol{k} \to \boldsymbol{0}) \approx H_0^{\text{eff}}(\boldsymbol{k})\,. \tag{3.9}$$

One can see that the inter-surface hybridization parameter m_1, which is largely irrelevant in the low energy Hamiltonian in Eq. 3.2, plays an essential role for the lattice Hamiltonian by preventing the appearance of unphysical states at low energies away from $\boldsymbol{k} = 0$. This facilitates the appearance of the quantum anomalous Hall effect by allowing non-zero Chern number in the appropriate regime. For $m_0 \ll m_1$ only the Γ-point avoided crossing is relevant at low energy, and H_0^{eff} is a faithful description of the above lattice Hamiltonian.

3.2 Topological classification

In this section, we show topological classification of the BdG Hamiltonian in both 1D and 2D. The focus here is to pedagogically understand all the possible topological phases. Hence for the most part we restrict to a specific case in the BdG Hamiltonian, where the topological phases can be understood analytically by comparing to the analysis in Sec. 2.1.1 and Sec. 2.2.1 in chapter 2. Later in Sec 3.3, we will discuss topologically non-trivial phase with the aim of a potential device.

3.2.1 Classification in 2D

The $\mathbb{Z}$-topological invariant for the magnetic TI/superconductor proximity system can be computed for the BdG Hamiltonian on lattice and calculating integral of the Berry curvature of all the negative energy Bogoliubov bands [56]. However, for a more physical understanding of the origin of different allowed values of the topological invariant, we first consider a special case of $\mu = \lambda' = 0$, and $\Delta_t = -\Delta_b = \Delta$. In this limit, the entire 8×8 BdG Hamiltonian of the system under the unitary transformation: $\tilde{\hat{\psi}}_{\boldsymbol{k}} = U\,\hat{\psi}_{\boldsymbol{k}}$, where the transformation matrix is

$$U = \frac{1}{2}\begin{pmatrix} 1 & 0 & 1 & 0 & 0 & 1 & 0 & -1 \\ 0 & 1 & 0 & -1 & 1 & 0 & 1 & 0 \\ 0 & -1 & 0 & 1 & 1 & 0 & 1 & 0 \\ 1 & 0 & 1 & 0 & 0 & -1 & 0 & 1 \\ 0 & 1 & 0 & 1 & 1 & 0 & -1 & 0 \\ 1 & 0 & -1 & 0 & 0 & 1 & 0 & 1 \\ -1 & 0 & 1 & 0 & 0 & 1 & 0 & 1 \\ 0 & 1 & 0 & 1 & -1 & 0 & 1 & 0 \end{pmatrix}, \tag{3.10}$$

can be block diagonalized into four 2×2 blocks, such that the transformed BdG Hamiltonian reads,

$$\begin{aligned} \tilde{H}_{BdG}(\boldsymbol{k}) &= U\,H_{BdG}(\boldsymbol{k})\,U^{-1} \\ &= \mathrm{diag}[\boldsymbol{h}_1 \cdot \boldsymbol{\sigma},\ \boldsymbol{h}_2 \cdot \boldsymbol{\sigma},\ \boldsymbol{h}_3 \cdot \boldsymbol{\sigma},\ \boldsymbol{h}_4 \cdot \sigma]\,. \end{aligned} \tag{3.11}$$

Here the 2×2 blocks are defined by the three component vectors

$$\boldsymbol{h}_1 = [\hbar v_F \sin k_y,\ -\hbar v_F \sin k_x, \\ m_0 + \lambda + \Delta + 2m_1(2 - \cos k_x - \cos k_y)]^T, \tag{3.12a}$$

$$\boldsymbol{h}_2 = [-\hbar v_F \sin k_y,\ -\hbar v_F \sin k_x, \\ -m_0 - \lambda + \Delta - 2m_1(2 - \cos k_x - \cos k_y)]^T, \tag{3.12b}$$

$$\boldsymbol{h}_3 = [\hbar v_F \sin k_y,\ \hbar v_F \sin k_x, \\ m_0 - \lambda - \Delta + 2m_1(2 - \cos k_x - \cos k_y)]^T, \tag{3.12c}$$

$$\boldsymbol{h}_4 = [-\hbar v_F \sin k_y,\ \hbar v_F \sin k_x, \\ -m_0 + \lambda - \Delta - 2m_1(2 - \cos k_x - \cos k_y)]^T, \tag{3.12d}$$

projected over the Pauli matrices. In the above transformed form, each 2×2 block is simply equivalent to one copy of the model spinless superconductor on a square lattice studied in detail in chapter 2. Each of the above copy has a different effective chemical potential and hopping strength. The $\mathbb{Z}$-topological invariant then is given by $N = \sum_{i=1}^{4} N_i$, where N_i can simply be deduced by comparing the Hamiltonian blocks $\boldsymbol{h}_i \cdot \sigma_i$ with the topological regions of the model studied in chapter 2.

Generally $\Delta_t \neq -\Delta_b$, and the nonzero values of λ' are also of our interest for tuning of topological phase. For a more general BdG Hamiltonian, one can not block diagonalize into 2×2 blocks. However, the topological invariants can still be calculated rather easily without performing the full Berry curvature calculation. It relies on the fact that topological invariant only changes when bulk gap closes. Hence one can start from the above discussed exactly solvable case and then slowly tune in any of the parameter of interest and track when the BdG spectrum becomes gapless.

The topological phase diagram shown in the Fig. 3.3 is obtained analytically for the specific case of $\mu = \lambda' = 0$ and $\Delta_t = -\Delta_b$. It shows presence of phases with $N = 0, \pm 1, \pm 2$. The phase with $N = \pm 1$ has single chiral Majorana edge state at the boundary of the system. For the experimental observation of chiral Majorana edge state, $N = \pm 1$ is the most interesting phase (see discussion in chapter 6). Interestingly, broad regions of $N = \pm 1$ phase appear at various energy scales on the phase diagram shown here.

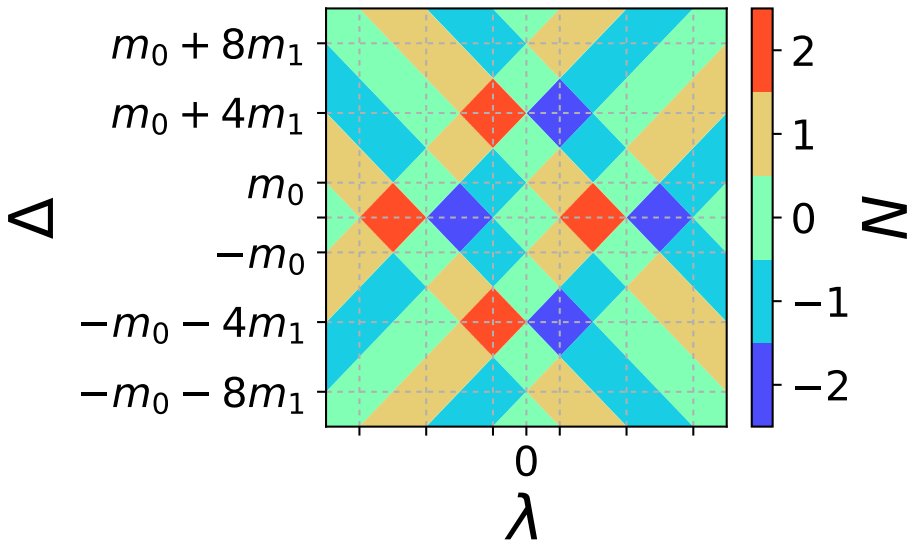

Figure 3.3: Lattice model Chern number N phase diagrams for 2D geometries with $\lambda' = \mu = 0$ and $\Delta_t = -\Delta_b = \Delta$: For visualization purposes. The figure is plotted at an unphysically small value of m_1/m_0. Realistically $m_1 \gg m_0$. Figure reproduced from the research article Phys. Rev. B **97**, 081102(R).

For any of the diagonal blocks $\boldsymbol{h}_i \cdot \boldsymbol{\sigma}$, as λ or Δ are tuned, depending on the specific values, the bulk gaps always close at one of the high symmetry point (Γ, X, Y, or M). For the simple case of $\mu = \lambda' = 0$ and $\Delta_t = -\Delta_b$ studied here, the gap closes at Γ point for $\pm\lambda \pm \Delta = m_0$. The gap closings at other high symmetry points (*i.e.* at X, Y, and M points) occur at energies which are integer multiples of m_1 higher in magnitude as can be seen in Fig. 3.3. Since $m_1 \gg m_0$, these gap closings occur at $1-2$ orders of magnitude higher energies and not generally accessible to drive a topological phase transition. Thus for our purpose we can simply take the limit $\boldsymbol{k} = 0$ in the H_{BdG} obtained from Eq. 3.3 and Eq. 3.6 to compute the topological phase diagram. Further for a realistic system, where superconductor is only on one side of the magnetic TI (see Fig. 3.1), $\Delta_t = 0$ and $\Delta_b = \Delta$ is the correct choice of parameters. If one considers only Γ point gap closing in the limit $\mu = \Delta_t = \lambda' = 0$, the topological phase boundaries can again be obtained analytically (See App. B). The low energy phase diagram is shown in Fig. 3.4, which is obtained by tracking the

gap closings and re-openings at Γ point. One can see that both for the special case of $\Delta_t = -\Delta_b$ as shown in Fig. 3.4(a) and for the realistic case of $\Delta_t = 0$ shown in Fig. 3.4(b), there are broad regions of interesting $N = \pm 1$ phase.

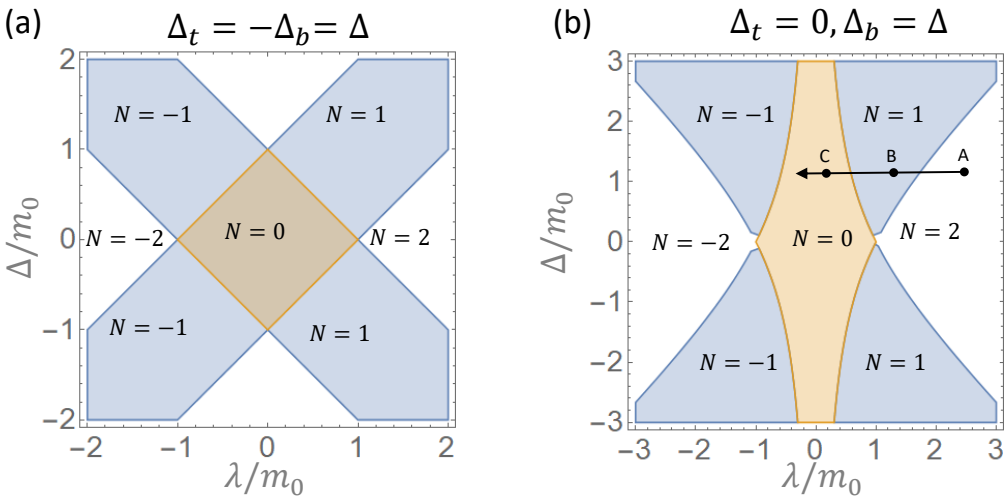

Figure 3.4: The topological phase diagram obtained by gap closings at Γ points: (a) calculated for the special case of $\mu = \lambda' = 0$ and $\Delta_t = -\Delta_b = \Delta$, (b) calculated for realistic scenario where $\Delta_t = 0$, $\mu = \lambda' = 0$. Broad regions of $N = \pm 1$ phase, which hosts single chiral Majorana edge state are present in both cases. The arrow in (b) shows a possible path an experimental system can take while tuning λ.

Experimentally, one can imagine λ being a controllable parameter by tuning the magnetization of the magnetic dopants. In Fig. 3.4(b), the arrow represents a possible experiment on this system, which we will discuss in detail in chapter 6. If one starts from $|\lambda| > m_0$ shown as the point A, where $N = 2$ (*i.e.* topologically a quantum anomalous Hall region) and slowly decreases λ to move towards trivial insulator state $N = 0$ shown as point C following the arrow, there is an intermediate region of $N = 1$ with single chiral Majorana edge state.

3.2.2 Classification in 1D

For a strictly 1D system, the Hamiltonian is obtained by taking k_y dependent terms of the 2D Hamiltonians studied above in Sec. 3.2.1 to zero. Similar to the 2D case, the limit $\mu = \lambda' = 0$, and $\Delta_t = -\Delta_b = \Delta$ is pedagogically interesting to understand the possible topological phases. In this limit, the transformed BdG Hamiltonian in its block diagonal form is simply

$$\tilde{H}_{BdG}(k_x) = \text{diag}[\boldsymbol{h}_1 \cdot \boldsymbol{\sigma},\, \boldsymbol{h}_2 \cdot \boldsymbol{\sigma},\, \boldsymbol{h}_3 \cdot \boldsymbol{\sigma},\, \boldsymbol{h}_4 \cdot \boldsymbol{\sigma}]^T\,, \tag{3.13}$$

where,

$$\boldsymbol{h}_1 = [0,\, -\hbar v_F \sin k_x,\, m_0 + \lambda + \Delta + 2m_1(2 - \cos k_x]^T\,, \tag{3.14a}$$
$$\boldsymbol{h}_2 = [0,\, -\hbar v_F \sin k_x,\, -m_0 - \lambda + \Delta - 2m_1(2 - \cos k_x)]^T\,, \tag{3.14b}$$
$$\boldsymbol{h}_3 = [0,\, \hbar v_F \sin k_x,\, m_0 - \lambda - \Delta + 2m_1(2 - \cos k_x)]^T\,, \tag{3.14c}$$
$$\boldsymbol{h}_4 = [0,\, \hbar v_F \sin k_x,\, -m_0 + \lambda - \Delta - 2m_1(2 - \cos k_x)]^T\,. \tag{3.14d}$$

Similar to the 2D case, the above 1D Hamiltonian is four model 1D spinless superconductor Hamiltonian studied in detail in Sec. 2.1.1 of chapter 2. The $\mathbb{Z}_2$ topological invariant of $\tilde{H}_{BdG}$ is then given by $\nu = \Pi_{i=1}^{4}\nu_i$, where ν_i is the $\mathbb{Z}_2$ invariant of the 2×2 block $\boldsymbol{h}_i \cdot \boldsymbol{\sigma}$ obtained by comparing it with the model Hamiltonian in chapter 2. The topological phase diagram of this special case in strictly 1D structure is shown in Fig. 3.5, which shows broad non-trivial regions.

The strict 1D limit, where chains are only one lattice site wide is not experimentally achievable. Our main interest is in the possibility of gate-defined quasi-1D topological regions embedded within the 2D film surface similar to the case of of narrow ribbons of semiconductor quantum wires [57, 47]. Keeping that in mind, next we study topological phase of quasi 1D systems, with some finite number of sites in y-direction. The ν_i for each diagonal block in this case cannot be obtained by simple comparison with model 1D spinless Hamiltonian. Instead one needs to follow the general recipe of calculating Pfaffian number at $k_x = 0, \pi$ discussed in Sec. 2.1.1 of chapter 2. The resulting topological phase diagram of quasi-1D structures with different width W are shown in Fig. 3.6. One can see, as the width of the quasi 1D structures increases, the individual topological regions start becoming smaller and there are rapid

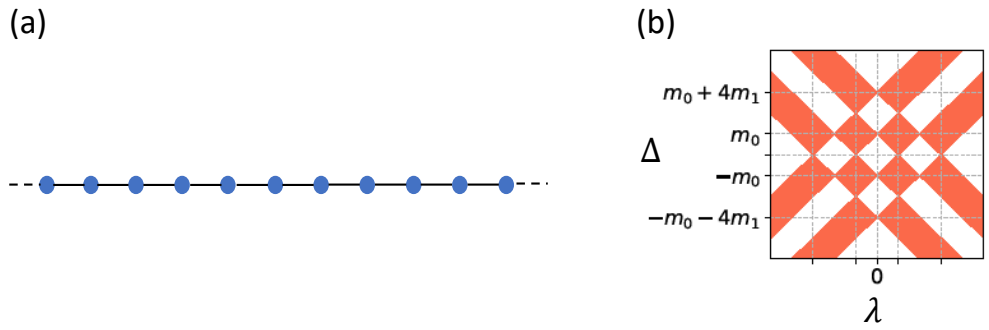

Figure 3.5: The topological phase diagram for strictly 1D system in the special case of $\mu = \lambda' = 0$ and $\Delta_t = -\Delta_b = \Delta$: (a) Shows the schematic of the 1D chain, where each site has four orbital owning to spin and layers, (b) The orange regions indicate topologically non-trivial regions where the $\mathbb{Z}_2$ invariant takes the values $\nu = -1$. This region has Majorana zero modes at the end of the 1D chain. Figure in panel (b) reproduced from the research article Phys. Rev. B **97**, 081102(R).

oscillations between topologically trivial and non-trivial regions. The rapid changes between different topological regions are potentially a limitation for an actual device. However, since $m_1 \gg m_0$, the actual width of these regions are still quite broad on a real energy scale.

Experimentally, the chemical potential μ and the magnetization energy λ are the most suitable tuning parameters. In Fig. 3.7 we show phase diagram for an experimentally achievable system, where superconducting pairing is only induced on one of the surface, hence $\Delta_t = 0$. The width of the quasi-1D stripe is fairly large at $W = 300$-lattice sites, which for a typical lattice constant $a \sim 4\mathring{A}$ is about 120nm. Stripes of width $W > 50$nm can be fabricated experimentally with good control. For these realistic parameters, Fig. 3.7 shows that the 1D topological classification of the quasi-1D structures is quite robust with broad regions of topological non-trivial regions. Another interesting feature is that unlike the 2D case, where $N = \pm 1$ topological phase is an intermediate phase between the quantum anomalous Hall phase and the trivial insulator phase, in the quasi 1D limit, the interesting $\nu = -1$ phase exists most strongly

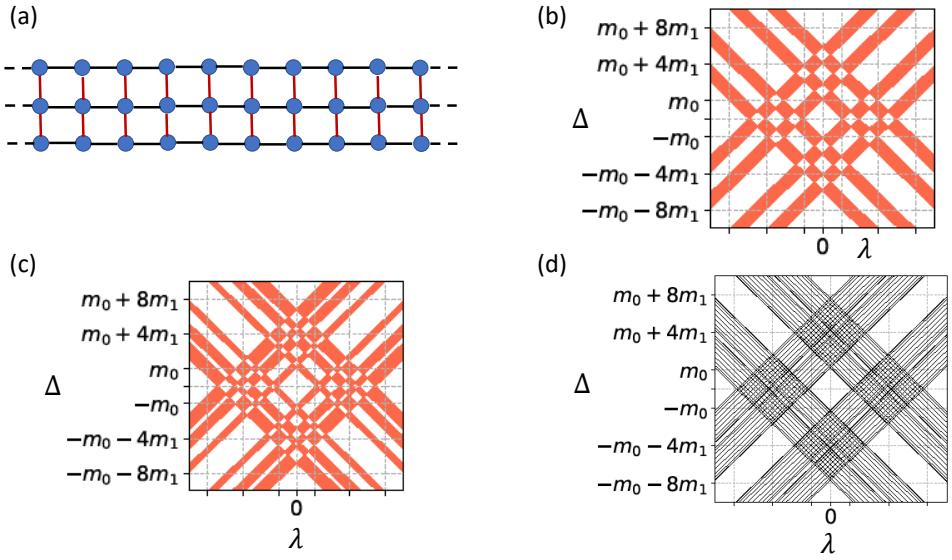

Figure 3.6: The $\mathbb{Z}_2$-Topological phase diagram for quasi-1D systems of different width along finite direction for the special case of $\mu = \lambda' = 0$ and $\Delta_t = -\Delta_b = \Delta$: (a) Shows a schematic of the lattice model, where each site has four orbitals owing to spin and layer index, (b) $W = 2$ atomic width aling y direction, (c) $W = 3$ atomic width along y-direction, and (d) $W = 10$ atomic width along y-direction. The shaded regions indicate topologically non-trivial regions where the $\mathbb{Z}_2$ invariant takes the values $\nu = -1$. Figures in the panel (b)-(d) are reproduced from the research article Phys. Rev. B **97**, 081102(R) .

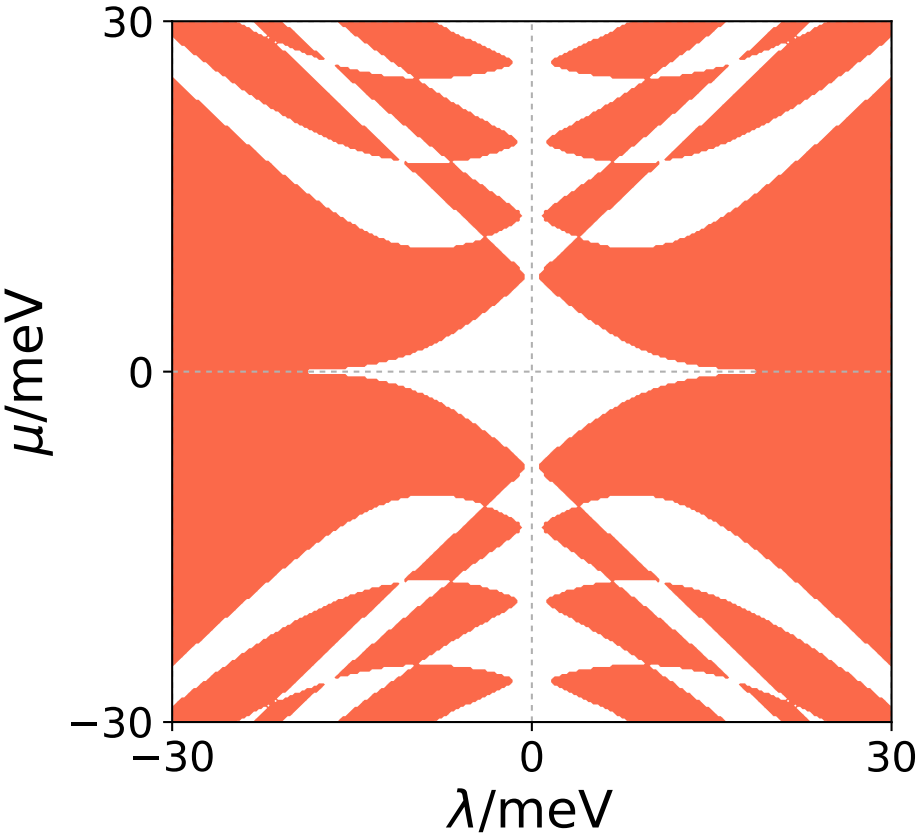

Figure 3.7: The $\mathbb{Z}_2$ quasi-1D phase diagram in (λ, μ) space for $\lambda' = 0$, $m_0 = 6$meV, $m_1 = 200$meV, $\Delta_b = 1$meV, $\Delta_t = 0$, Fermi velocity velocity $\hbar v_F = 700$meV, and ribbon width $W = 300$-sites. The orange regions are topologically non-trivial with $\nu = -1$ and support Majorana zero modes. Figure reproduced from the research article Phys. Rev. B **97**, 081102(R).

for large λ *i.e.* where the 2D limit of the normal part would be deep into its quantum anomalous Hall phase. Later in chapter 6, we show this difference from the 2D limit makes these quasi-1D structures potentially more reliable source of Majorana modes.

For weak pairing, the $\mathbb{Z}_2$ phase with $\nu = \pm 1$ depends on whether the number of normal state bands that cross the Fermi level is even or odd. The broad region of topologically nontrivial behavior at large λ and small μ in Fig. 3.7, *i.e.*

when the unproximitized magnetic TI is in a quantum anomalous Hall state, reflects the property that only a single quasi 1D band is present in this energy range at any value of W. The $\mathbb{Z}_2$ invariant is qualitatively more sensitive to λ, μ, W and other model parameters of quasi 1D structure at larger values of μ that lie within the gapped surface state bands. For a lattice model of a normal 2D p-wave superconductor, for example, there are $4W$ phase boundaries in the quasi-1D $\mathbb{Z}_2$ classification of structures of width W lattice sites. This sensitivity is not favorable for reliable realization of either trivial or non-trivial states. In the quantum anomalous Hall state there is at most a single band, but the Majorana zero modes present for finite length are protected only by exponentially small superconducting gaps ($\sim \Delta e^{-W/\xi}$), where $\xi \sim v/(\lambda - m_0)$ is the 2D edge state localization length in lattice constant units, making the $\mathbb{Z}_2$ classification academic. (For typical parameters $\xi \sim 10$nm) In order to obtain Majorana zero modes that are reasonably localized near quasi-1D ends it is necessary to have widths W that are not too large compared to ξ, and also to be able to conveniently tune between topologically trivial and non-trivial states. Since the exchange coupling parameter λ in Fig. 3.7 is fixed for a given magnetic TI sample and a given operating temperature, a different tuning parameter must be identified. Next, we show that an electric field between the two layers of magnetic TI can be used for this purpose.

3.3 The quantum anomalous Hall effect based Majorana platform

In this section, we discuss an experimentally tunable device for Majorana zero modes based on the quantum anomalous Hall system under consideration throughout this chapter. As shown in last section, Majorana zero modes can appear at the end of a quasi-1D structure of this system with broad regions of topological stability, however, challenge lies in tuning different topological phases or spatially defining regions of topologically trivial and non-trivial phase, where Majorana modes can be localized. For this purpose, we propose controlling Majorana zero modes in quasi 1D structures by placing a magnetic TI film that supports a quantum anomalous Hall state on a superconducting substrate and fabricating a top gate. A schematic of such device is shown in

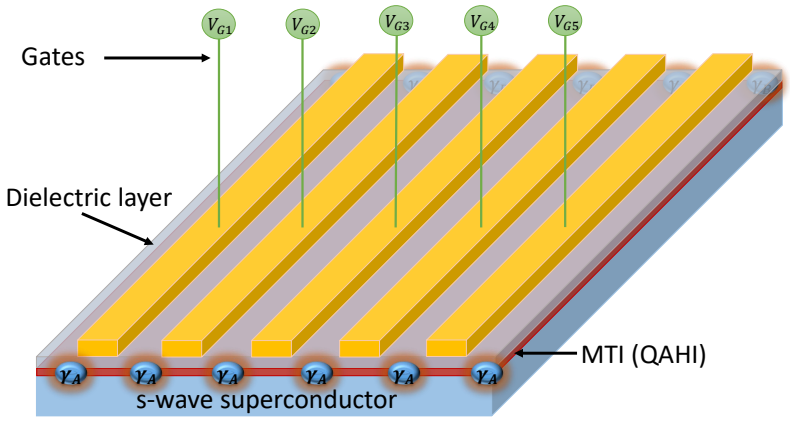

Figure 3.8: A simple device setup for quasi-1D topological superconductors: Majorana zero modes can be created locally by separating the surface of a magnetic TI (MTI) in the quantum anomalous Hall (QAH) state into alternating normal and topological regions using remote gates. Figure reproduced from the research article Phys. Rev. B **97**, 081102(R).

Fig. 3.8. Varying the gate field will alter the carrier density (and hence the chemical potential μ) of the magnetic TI, and also shift the energy of the top surface Dirac cone relative to the bottom surface. The latter effect is due to the unscreened portion of the gate electric field that survives in the interior of the TI and is represented in our model by the parameter λ'. Applying a gate voltage moves the system along a line in (μ, λ') space that depends on the effective bulk dielectric constant of the TI. As we now show a gate voltage can therefore tune the proximitized magnetic TI between $\mathbb{Z}_2$ index trivial given by $\nu = 1$ and non-trivial given by $\nu = -1$.

With the goal of gate controlling the energy difference λ' between the two surfaces of magnetic TI and using it as a tuning parameter to control topological phases, we study the topological phase diagrams as a function of λ'. Fig. 3.9 illustrates 2D Chern number phase diagrams in (λ',μ) space for magnetic TI on superconducting substrates with $\Delta_b = 0.2m_0$ and $\Delta_t = 0$, at three different values of exchange field λ. For $\lambda < m_0$ [left panel Fig. 3.9 (a)], the

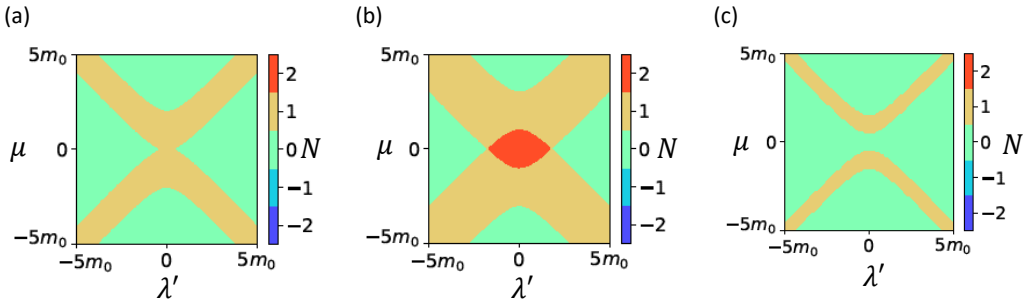

Figure 3.9: Phase diagram of a magnetic TI on a superconducting substrate in λ'-μ space. Here $\Delta_b = 0.2m_0$, $\Delta_t = 0$, and from left to right $\lambda = 0.5m_0$, m_0, and $2m_0$. Figure reproduced from research article Phys. Rev. B **97**, 081102(R).

unproximitzed magnetic TI is in a normal insulator state, but superconductivity that is sufficiently strong can still induce odd Chern number BdG states. Our main interest is in the case in the right panel [Fig. 3.9 (c)] where $\lambda > m_0$ so that the unproximitized magnetic TI is in a quantum anomalous Hall state at $\lambda' = 0$. Proximitized superconductivity of quantum anomalous Hall states is now routinely achieved experimentally [8, 26]. The quantum anomalous Hall state occurs at small $|\mu|$ only when $\sqrt{\lambda'^2 + m_0^2} < |\lambda|$; the gate field λ' efficiently converts a quantum anomalous Hall insulator with edge states into a normal insulator with no edge states in the gap, and no opportunity for $\mathbb{Z}_2$ states in the quasi 1D limit.

The energy displacement between the two layers of magnetic TI applied using gates is unfavorable for $N = 1$ topological superconducting state in 2D. Hence λ' also makes it unfavorable for Majorana zero modes to appear in quasi 1D limit [See Fig. 3.10c]. A controllable device to create Majorana zero modes then can be achieved by defining gate controlled quasi 1D regions on a base 2D proximity coupled system of magnetic TI and superconductor, such as shown in Fig. 3.8. In the limit when λ is tuned to high value throughout the 2D base (*i.e.* the unproximitized magnetic TI being deep in quantum anomalous Hall phase), and two nearby quasi 1D gates are turned on, the region immediately

below them has trivial classification of $\mathbb{Z}_2$ index. However, the quasi 1D region between the two nearby gates have non-trivial $\mathbb{Z}_2$ classification. Hence, Majorana zero modes can be bound at the end of the intermediate region.

Having shown a Majorana device in principle, next we explain why the quantum anomalous Hall based device has much larger regions of stability of topologically trivial and non-trivial phase and the quasi-1D limit can be reached at much larger length scale ($W \sim 100nm$) compared to semiconductor quantum wire based device.

For weak pairing, quasi 1D structures have non-trivial $\mathbb{Z}_2$ index give by $\nu = -1$ states when an odd number of subbands cross the Fermi level. In a quasi 1D structure formed from a semiconductor quantum well with strong Zeeman and spin-orbit coupling, or from a magnetic TI with $\lambda \ll m_0$, a series of closely spaced non-degenerate 1D sub-bands appear close to the extrema of the bulk 2D bands, as illustrated schematically in Fig. 3.10a. When the quasi 1D structure width increases, the spacing between subbands becomes smaller and the $\mathbb{Z}_2$ phase diagrams will have more closely spaced boundaries between $\mathbb{Z}_2$ index trivial *i.e.* $\nu = 1$ and non-trivial $\nu = -1$ phases. In the $\lambda \gg m_0$ quantum anomalous Hall case on the other hand, illustrated schematically in Fig. 3.10b, a single pair of bands crosses the Fermi level at all energies inside the bulk 2D gap, except for a narrow gapped region due to the avoided crossing between quantum anomalous Hall edge states localized on opposite sides of the ribbon. The system is therefore almost always nontrivial in the broad range $\mu \in (-E_b, E_b)$, where E_b is the bulk gap, independent of the quasi 1D structure width.

Figure 3.10c shows the $\mathbb{Z}_2$ phase diagram in (μ, λ') plane of $W = 300$ lattice sites, $m_0 = 6\,\mathrm{meV}, m_1 = 0.2\,\mathrm{eV}, v = 0.7\,\mathrm{eV}, \lambda = 12\,\mathrm{meV}, \Delta_b = 1\,\mathrm{meV}, \Delta_t = 0$ quasi 1D structure, which exhibits large adjacent trivial and nontrivial regions near $\mu = 0$. For these realistic parameters $|\lambda|$ is larger than m_0, but not much larger. Larger quantum anomalous Hall regions can be achieved by going to thicker films with smaller m_0 but only at the expense of reducing all relevant energy scales. quantum anomalous Hall edge states overlap strongly even at $W = 300$, so strongly in fact that the normal state gap produced by avoided crossing of edge states is comparable to m_0, creating a substantial $\mathbb{Z}_2$ index $\nu = 1$ region near $\mu = 0$. This region is however still bordered at $\lambda' = 0$ by a

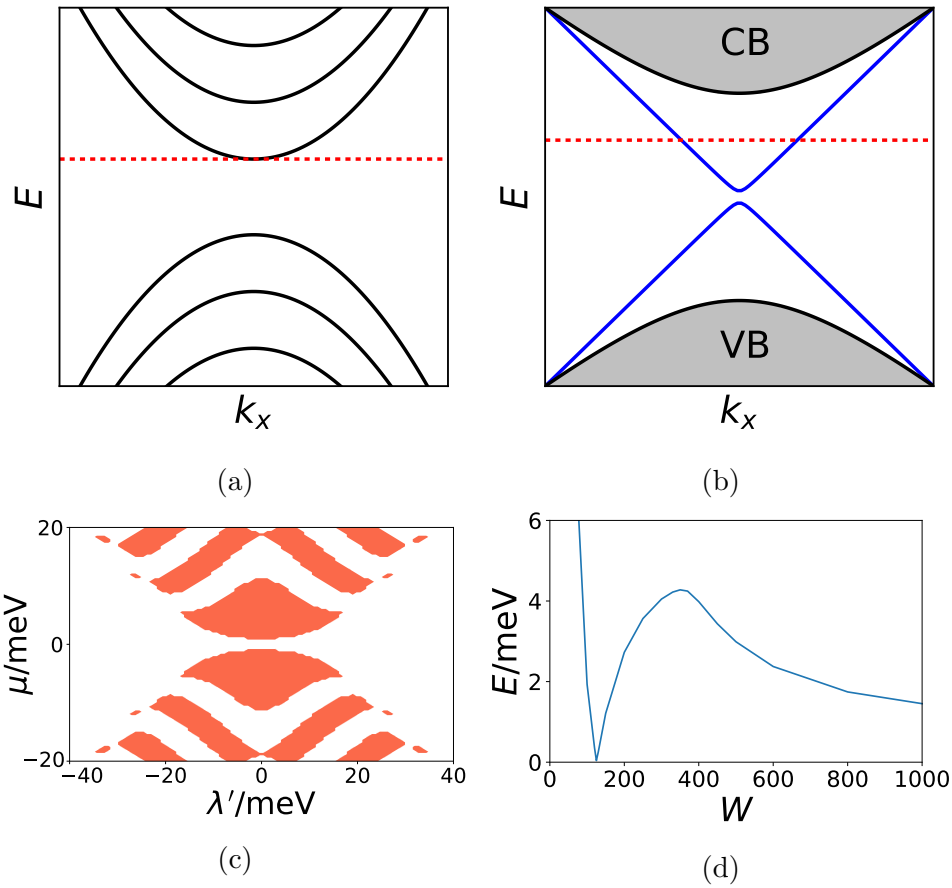

Figure 3.10: Topological phases and their robustness: (a) Bandstructure of a nanoribbon. When the Fermi level (the red dotted line) coincides with the bottom of a subband, a topological phase transition occurs; (b) Bandstructure in the quantum anomalous Hall regime. Grey regions are conduction and valence bands, blue curves are edge states with a small hybridization gap, and the red dotted line shows the Fermi level. When the chemical potential is inside the bulk gap and outside the hybridization gap, with superconductor the system should always be nontrivial. (c) Phase diagram in λ'-μ space for a quasi-1D chain with $W = 300, m_0 = 6\,\text{meV}, m_1 = 0.2\,\text{eV}, v = 0.7\,\text{eV}, \lambda = 12\,\text{meV}, \Delta_b = 1\,\text{meV}, \Delta_t = 0$; (d) Relation between gap and width, with $\mu = 5\,\text{meV}, \lambda' = 0$ and other parameters the same as in (c). Figure reproduced from the research article Phys. Rev. B **97**, 081102(R) .

large $\mathbb{Z}_2$ index $\nu = -1$ region that can be identified with pairing of quantum anomalous Hall edge states. The gate field λ' sweeps this state into a large adjacent $\mathbb{Z}_2$ index $\nu = 1$ region, which can be identified with a proximity coupled ordinary insulator.

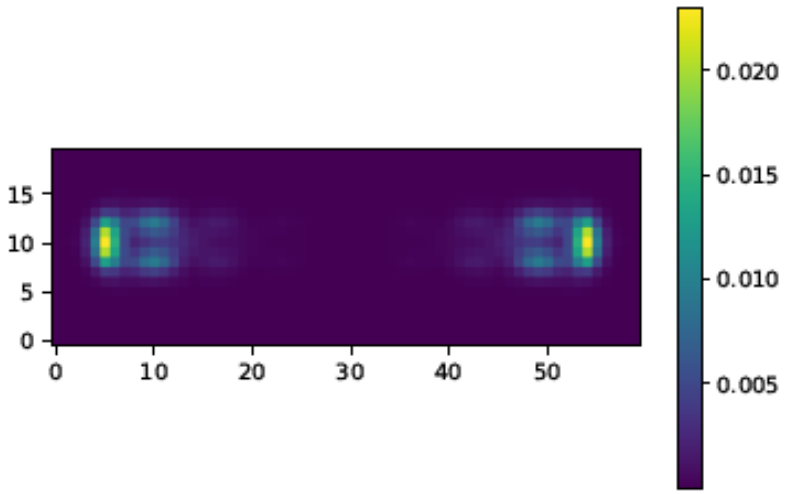

Figure 3.11: Spatial distribution of the lowest energy eigenstate, where a 50×5 quasi-1D region is embedded in a 60×20 system, and $m_0 = 1$, $m_1 = 2$, $\hbar v_F = 2$, $\lambda = 2$, $\mu = 1$, $\Delta_b = 1$, and $\Delta_t = 0$. Inside and outside the quasi-1D region, $\lambda' = 0$ and 4 respectively. Figure reproduced from the research article Phys. Rev. B **97**, 081102(R) .

Figure 3.10d plots the quasi 1D width dependence of the gap at $k_x = 0$, $\lambda' = 0$, and $\mu = 5\,\text{meV}$ out to $W \sim 1000$ in lattice constant units. Here we notice that there is only one gap closing as a function of W which signals a phase transition between a small W, where $\mathbb{Z}_2$ index is trivial with $\nu = 1$; state associated with a large avoided crossing gap between quantum anomalous Hall edge states, and a large W, where $\mathbb{Z}_2$ index is $\nu = -1$; state associated with pairing of quantum anomalous Hall edge states. The gaps remain large out

to $W \sim 1000$ lattice constants, corresponding to a physical length $\sim 400\,\text{nm}$, partly because the edge state localization length is enhanced by the relatively high velocity of quantum Hall edge states compared to the velocity of states present near the bottom of a bulk 2D band. As the system becomes wider, the quantum anomalous Hall edge states have less overlap and the gap is eventually reduced to very small values.

Because of the bulk-edge correspondence of topological states we expect Majorana zero modes to appear not only in very thin stripes, but also in wide films in which quasi 1D regions are formed that have local model parameters in the topologically non-trivial range. Fig. 3.11 shows the localized Majorana zero modes at the end of a topological quasi 1D region embedded in the larger region. This verfies the presence of zero energy localized modes corresponding to $\mathbb{Z}_2$ index having nontrivial $\nu = -1$ value.

3.3.1 Creating and manipulating Majorana zero modes

Apart from the advantage associated with broad regions of topologically distinct phase, the quantum anomalous Hall based device for Majorana modes is potentially more suitable for performing an elementary topological quantum computation operation. Majorana modes have non-Abelian exchange statistics [13] in 2D, which is the fundamental reason behind their interest in topological quantum computation. For any useful application braiding two Majorana is essential. Thus, even if Majorana modes are created at the end of 1D structure, the braiding operation requires moving one Majorana around the other, which requires the operation to be done in 2D, because one cannot exchange them by simply moving along one direction without them annihilating each other. The fact that our proposed device has a base 2D platform makes it easier to achieve any of the proposed braiding architecture [58, 59].

Fig. 3.12 shows the famous T-junction architecture proposed by Alicea *et. al.* [58] on our proposed quantum anomalous Hall based system. Since gates can be defined with a good precision at arbitrary position on the 2D base, the T-junction can be defined and manipulated as shown in the Fig 3.12(a)-(d). Additionally, multiple of such regions or quasi 1D structures can be defined over the entire 2D base (See Fig. 3.8), which gives it a potential advantage over

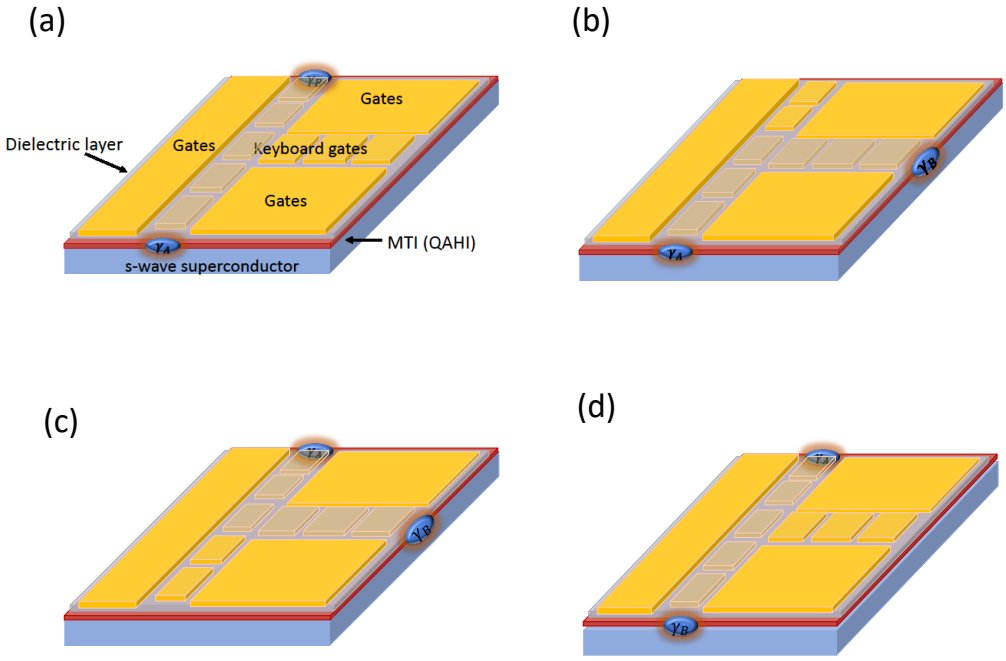

Figure 3.12: A schematic of braiding two Majorana zero modes via exchanging their position: The gates are represented by golden rectangular regions. The solid golden regions indicate gates turned on ($i.e. \lambda' \neq 0$) and the transparent golden regions indicate gates turned off ($i.e.\ \lambda' = 0$). (a) Two Majorana zero modes γ_A and γ_B are at the end of the straight quasi 1D topological wire represented with turned off gates. (b) As the gates on the top are turned on and on the right are turned off γ_B Majorana moves to the right end. (c) The gates at the bottom are turned on and at the top are turned off, γ_A Majorana moves to the top end. (d) Finally, gates at the right are turned on, and at the bottom are turned off, γ_B Majorana moves to the bottom. (a) and (d) have same topological quasi 1D structure but the Majoranas are exchanged.

semiconductor quantum wire device. Since in semiconductor quantum wire system, to achieve large scale architecture on has to deposit many quantum wires on some base in precise way with desired relative orientation, which can be difficult to achieve.

3.4 Conclusion

In this chapter, we have studied the topological phases of a magnetic TI thin film proximity coupled to an s-wave superconductor in 1D and 2D.

In 2D this system has been studied previously [50], and shows the presence of chiral topological superconducting phase. Our focus is on quasi 1D structures based on this system, which can be used to bind Majorana zero modes [27]. Besides, showing the extraordinary stable topological superconducting phase in quasi 1D limit of this system, we highlight the potential flexibility of this system in achieving an actual device to braid Majorana. Topological quantum computation requires flexible Majorana braiding that relies on branched structures like T-junctions [18]. Although conceptually simple, T-junctions based on semiconductor quantum wires are difficult to build because of challenges in depositing aligned semiconductor quantum wires. In this chapter, we have demonstrated the possibility of using gate arrays to write Majorana zero modes onto the surface of a 2D magnetic TI placed on a superconducting substrate. It has some similarities with systems [60, 61] in which a gate array writes quantum wires onto a quantum well by periodically depleting all carriers, or varying the number of locally occupied subbands between even and odd values, but has advantages in this case as well because i : it is not necessary to apply a magnetic field to break degeneracies at time-reversal invariant points in 1D momentum space and because ii : there can be a large energy separation between the quasi-1D bands formed by quantum Hall edge states and higher energy subbands, providing a large target for efforts to tune to $\mathbb{Z}_2 = -1$ superconductors. Additionally, this system also provides an ideal platform for building the Majorana box qubits recently proposed in Refs. [59, 62] because i : it is easy to define arbitrary number of parallel gate-controlled quasi-1D topological superconducting wires as shown in Fig. 3.8, and ii : because large topological stability ranges allows geometrical capacitance[62] to be changed

without changing topological states.

Chapter 4

Topological superconductivity in the quantum Hall regime

In this chapter[1] we study the chiral topological superconducting phase in 2D, when an s-wave superconductor is proximity coupled to a quantum Hall system, obtained under Landau quantization of the 2DES.

In chapter 2 and 3, we have shown that chiral topological superconductors are expected to appear as an intermediate states when a quantum anomalous Hall system is proximity coupled to an s-wave superconductor and made to go under topological Chern insulator to trivial insulator transition of the unproximitized system. Since, quantum Hall state is also Chern insulator (topologically identical to the quantum anomalous Hall state), the natural question arises, if the same is true for quantum Hall system? We find that the appearance of topological superconducting phases with an odd number of Majorana edge modes is dependent on the structure of the system's vortex lattice [41]. More precisely, vortex lattices containing odd number of superconducting flux quanta per unit cell, always support an even number of chiral edge channels and are therefore adiabatically connected to the normal quantum Hall insulators. We discuss strategies to engineer chiral topological superconductivity in proximity-coupled quantum Hall systems by manipulating vortex lattice structure.

[1]This chapter is based on the research article: Gaurav Chaudhary and Allan H. MacDonald, *Vortex Lattice Structure and Topological Superconductivity in the Quantum Hall Regime* , arXiv:1903.12249. Allan H. MacDonald suggested and supervised the research. Gaurav Chaudhary performed the analytical and numerical calculations. Both authors contributed to discussion and manuscript writting. Parts of the text and figures are reproduced from the above mentioned research article.

The focus in this chapter is on chiral Majorana edge modes unlike the last chapter, where main focus was on Majorana zero modes. Experimentally the chiral Majorana edge modes have been more elusive. A recent experiment [26], however, has identified possible signatures of the chiral Majorana edge states in a transport study of a thin film of magnetic TI that is proximity coupled to an s-wave superconductor [26]. The distinct transport signature related to the chiral Majorana state relies on the presence of phase with odd number of chiral Majorana edge states, since for the phase with even number of chiral Majorana modes, the transport signature would be identical to a quantum Hall system (See chapter 6 for related discussion). As we have already discussed in chapter 3, in their normal state, magnetic TI can be tuned between Chern insulator states that exhibits a quantized anomalous Hall effect which changes sign upon magnetization reversal. In thin films, magnetized TI can also become normal insulators. The Chern insulator is formed when interactions between surface state quasiparticles and the magnetic order parameter are dominant and the normal insulator state when hybridization between the top and bottom surfaces of the film are dominant. When coupled to an s-wave superconductor the Chern insulator state yields even-$\mathbb{Z}$ topological superconductors, whereas the normal state generates a topologically trivial superconductor. If one naively models magnetization reversal by smoothly changing the coupling between quasiparticle spins and the magnetic order parameter between positive and negative values, odd-$\mathbb{Z}$ superconducting states that support isolated Majorana edge modes appear as an intermediate phase (See Sec. 3.2 in chapter 3). The transition between normal states with different Chern numbers is normally tuned by using an external magnetic field to drive magnetization reversal, which generates an intermediate state that typically contains a magnetic domain pattern. This complicates the interpretation of any experiment [26, 63, 64, 65, 66] (See also discussion in chapter 6). In this chapter, we theoretically explore the possibility of following an alternative and potentially simpler route to engineer chiral Majorana edge modes, namely by looking near plateau transitions in ordinary quantum Hall systems.

Since the quantum Hall effect usually requires fairly strong external magnetic fields it has until recently generally been viewed as being incompatible with superconductivity. Observing topological superconductivity in quantum

Hall system has recently been identified as an important direction for theoretical and experimental work for several reasons: i) to realize parafermions which are generalization of Majorana edge modes obtained when the fractionalized edge modes of fractional quantum Hall systems have induced topological superconductivity [67], ii) to achieve better tunability and control of multiple chiral Majorana edge modes involving higher Chern numbers, and iii) because of the on going debate on whether or not a half-integer quantum Hall plateau is a unique signature of Majorana edge modes or can alternately be induced by disorder [63, 64, 65, 66]. Since quantum anomalous Hall edge modes are not typically quantized as perfectly as the quantum Hall edge modes in realistic disordered systems even in the absence of superconductivity, it seems that progress can be made by looking for half integer quantized Hall plateaus in quantum Hall systems. Some theoretical progress in this direction has already been made in a study of systems that are proximity coupled to a parent p-wave superconductor [68].

With this motivation, we seek to identify the circumstances necessary to achieve topological superconductivity in the quantum Hall regime. quantum Hall/superconductor proximity systems are hybrid-2D systems with the superconductor thin film in mixed states when under perpendicular magnetic field. We show here that vortex lattice properties influences the topological properties of quantum Hall/s-wave superconductor hybrid systems. We attribute this feature to the flatness to single particle Landau levels, which lead to bulk quasiparticle dispersion in the superconducting state that is largely determined by the vortex lattice periodicity. We show that the structure of the vortex lattice plays an important role in chiral Majorana edge mode formation by determining the degeneracy of band crossings which can potentially drive topological phase transitions between states with even and odd-$\mathbb{Z}$ topological indices. The most important findings of this chapter apply when small number of Landau levels host superconducting pairing from an s-wave superconductor. In this limit, the details of origin of Landau levels (such as arising from Dirac electron or quadratic band) are not important for possible topological superconducting phases. Instead, the vortex lattice structure plays the main role.

The chapter is organized as follows. Section 4.1 describes a model that

includes Landau quantization along with proximity superconductivity. Section 4.2 discusses vortex lattice states in 2D and their relationship to electronic structure in the superconducting state. Section 4.3, discusses topological phases from the point of view of bulk quasiparticle spectra, considering single Landau level limit, then a minimal model containing only two Landau levels, and then more generally including many Landau levels with a Debye cutoff. For the purpose of illustrating the most important results, the two Landau level model is the most important case, as well as experimentally achievable. Section 4.4 calculates the edge spectrum and demonstrates a transition between ordinary quantum Hall edges and edges that support chiral Majorana edge modes as the bulk topological phase is changed. Section 4.5 discusses possible experiments that are motivated by the theoretical results. Section 4.6 contains conclusion and brief discussion.

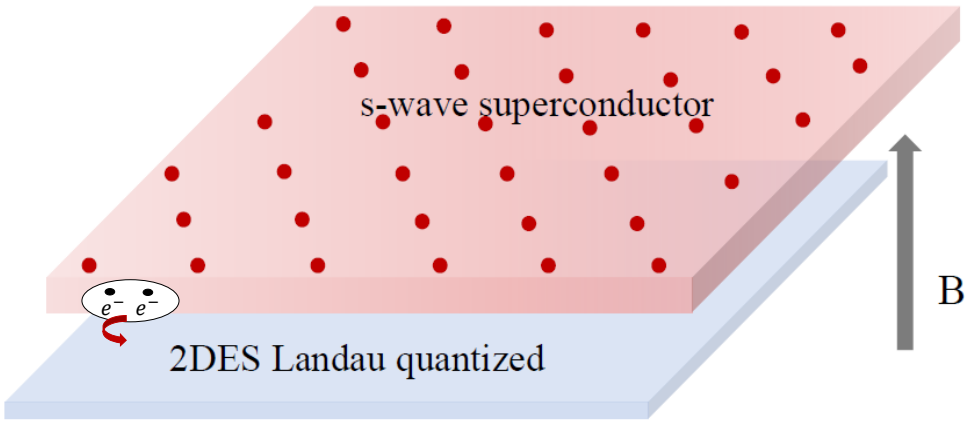

Figure 4.1: Quantum Hall system proximity coupled to an s-wave superconductor: Because of the perpendicular magnetic field, the superconductor exists in the Abrikosov vortex lattice phase. The Cooper pair tunneling back and forth between the superconductor and Landau quantized normal part indicates the proximity effect.

4.1 Pairing in Landau levels

In this section we discuss proximity pairing in the Landau levels of a two dimensional system. The Landau level spectrum depends on the zero field dispersion of the system. Here, we consider a linear band crossing (Dirac) model to describe the non-interacting system in all the calculations. 2D Dirac systems, for example the surface states of 3D TIs, are attractive as hosts for the physics we address because their linear band dispersion leads to large Landau level separations and quantum Hall physics at relatively weak magnetic field strengths that are more often comparable with superconducting pair potentials. However, most of the results are general and equally applicable to ordinary non-relativistic two-dimensional electron gas (2DEG) systems described by quadratically dispersing bands as we discuss in the App. E. We are interested in proximitized superconductivity when these systems are close to quantum Hall plateau transitions. A simple setup of the system is represented pictorially in Fig. 4.1.

The BdG Hamiltonian of the proximity coupled system under consideration is

$$H_{BdG} = \begin{pmatrix} \hat{H}_0(\boldsymbol{\pi}) & \hat{\Delta}(\boldsymbol{r}) \\ \hat{\Delta}^\dagger(\boldsymbol{r}) & -\hat{H}_0^*(-\bar{\boldsymbol{\pi}}) \end{pmatrix}, \tag{4.1}$$

Here, $\hat{H}_0(\boldsymbol{\pi}) = -v_F \boldsymbol{\pi} \cdot \boldsymbol{\sigma}$ is the Dirac Hamiltonian operator of an isolated surface state of a 3D TI and v_F is the Dirac velocity. The Pauli matrices σ_i act on electron spin. It is important in our calculations that the s-wave pair potential

$$\hat{\Delta}(\boldsymbol{r}) = \begin{pmatrix} 0 & \Delta(\boldsymbol{r}) \\ -\Delta(\boldsymbol{r}) & 0 \end{pmatrix}, \tag{4.2}$$

introduced through proximity coupling is unavoidably non-uniform due to vortex lattice formation when flux penetrates the adjacent superconductor. H_{BdG} in Eq. 4.1 is written in the basis, $\hat{\psi}_{\boldsymbol{r}} = (\hat{c}_{\boldsymbol{r}\uparrow}, \hat{c}_{\boldsymbol{r}\downarrow}, \hat{c}^\dagger_{\boldsymbol{r}\uparrow}, \hat{c}^\dagger_{\boldsymbol{r}\downarrow})$, where $\hat{c}_{\boldsymbol{r}\uparrow}$ annihilates a spin-up electron at position $\boldsymbol{r}$. The perpendicular magnetic field $\boldsymbol{B} = B\hat{z}$ is introduced using the Landau gauge vector potential $\boldsymbol{A} = (-By, 0)$ which allows for a simple description of the edge modes on which we focus much of our attention. The electron and hole subspace kinetic momentum operators

are then defined as $\boldsymbol{\pi} = \boldsymbol{p} - eA$ and $\bar{\boldsymbol{\pi}} = \boldsymbol{p} + eA$ respectively, where $\boldsymbol{p} = -i\hbar\boldsymbol{\nabla}$ is the canonical momentum operator.

The BdG Hamiltonian of the 2D Dirac vortex lattice state can be conveniently diagonalized in the Landau level basis. We define the Landau level lowering and raising operators in the electron subspace of H_{BdG} as $\hat{a} = (-\hat{\pi}_x + i\hat{\pi}_y)\ell/\sqrt{2}\hbar$ and $\hat{a}^\dagger = (-\hat{\pi}_x - i\pi_y)\ell/\sqrt{2}\hbar$ respectively. In the absence of pairing, Hamiltonian diagonalization reduces to the familiar Dirac Landau level problem. The eigenvalues and eigenvectors in absence of pairing are as follows:

$$\xi_N = \epsilon_0 S_N \sqrt{|N|B}\,, \tag{4.3a}$$

$$\psi_{N,Y}(\boldsymbol{r}) = \mathcal{N}_N \begin{pmatrix} S_N \phi_{|N|-1,Y}(\boldsymbol{r}), & \phi_{|N|,Y}(\boldsymbol{r}) \end{pmatrix}^T . \tag{4.3b}$$

where the normalization factor,

$$\mathcal{N}_N = \begin{cases} \frac{1}{\sqrt{2}} & N \neq 0\,, \\ 1 & N = 0\,. \end{cases} \tag{4.4}$$

Here, $\epsilon_0 = v_F\sqrt{2e\hbar}$, S_N is the sign of N^{th} Dirac Landau level index, $Y = k_x\ell^2$ is a guiding center label, $\ell = \sqrt{\hbar/eB}$ is the magnetic length, $\phi_{n,k_x\ell^2}(\boldsymbol{r}) = (\mathrm{e}^{ik_x x}/\sqrt{L_x})\,\varphi_n(y/\ell - k_x\ell)$ is a n^{th} Landau level wave function of the non-relativistic 2DEG, and $\varphi_n(y)$ is a one dimensional harmonic oscillator eigenfunction.

The single particle states in the hole block of H_{BdG} can be constructed similarly using hole space Landau level raising and lowering operators, $\hat{\bar{a}}^\dagger = \hat{\bar{\pi}}_x - i\hat{\bar{\pi}}_y$ and $\hat{\bar{a}} = \hat{\bar{\pi}}_x + i\hat{\bar{\pi}}_y$ respectively, giving the following eigenvalues and eigenvectors:

$$\bar{\xi}_N = -\epsilon_0 S_N \sqrt{|N|B}\,, \tag{4.5a}$$

$$\bar{\psi}_{N,Y}(\boldsymbol{r}) = \mathcal{N}_N \begin{pmatrix} S_N \bar{\phi}_{|N|-1,Y}(\boldsymbol{r}), & \bar{\phi}_{|N|,Y}(\boldsymbol{r}) \end{pmatrix}^T , \tag{4.5b}$$

where $\bar{\phi}_{N,Y} = \phi^*_{N,-Y}$.

Next task is to calculate the matrix element of the pair potential in the Landau level basis. The pair potential carries the information about the vortex

lattice structure(the details on this are discussed in next section.) For the convenience in calculating the matrix element of the pair potential $\Delta(\boldsymbol{r})$, the Bogoliubov quasiparticle amplitude can be expanded over the ordinary 2DEG Landau level basis:

$$u_\sigma^\nu(\boldsymbol{r}) = \sum_{N,Y} u_{\sigma,N,Y}^\nu \phi_{N,Y}(\boldsymbol{r})\,, \tag{4.6a}$$

$$v_\sigma^\nu(\boldsymbol{r}) = \sum_{N,Y} v_{\sigma,N,Y}^\nu \bar{\phi}_{N,Y}(\boldsymbol{r})\,. \tag{4.6b}$$

Here $u_\sigma^\nu(\boldsymbol{r})$ and $v_\sigma^\nu(\boldsymbol{r})$ are respectively the spin σ electron and hole amplitudes of the ν-th BdG quasiparticle.

The matrix elements of the pair potential in the non-relativistic 2DEG-Landau level basis are given by

$$\mathcal{G}_{Y,Y'}^{N,M} = \int d\boldsymbol{r}\, \Delta(\boldsymbol{r}) \phi_{|N|,Y}^*(\boldsymbol{r}) \bar{\phi}_{|M|,Y'}(\boldsymbol{r})\,. \tag{4.7}$$

To evaluate the above expression, we first define center-of-mass (COM) and relative degrees of freedom, using the Landau level lowering operators,

$$\hat{a}_R = \frac{\hat{a}_1 + \hat{a}_2}{\sqrt{2}}\,, \quad \hat{a}_r = \frac{\hat{a}_1 - \hat{a}_2}{\sqrt{2}}\,, \tag{4.8}$$

where $\hat{a}_1$ and $\hat{a}_2$ are the Landau level lowering operators of individual electrons of the pair. In the transformed COM and relative coordinates, the wavefunctions ϕ^R and ϕ^r are identical to the single-particle wavefunctions except that the characteristic lengths are scaled to account for the changes of charge and mass. The effective magnetic lengths are $\ell^R = \ell/\sqrt{2}$ and $\ell^r = \sqrt{2}\ell$, for the COM and relative eigenstates respectively. Using this transformation the pairing matrix elements can be evaluated with the result:(See App. C for a derivation.)

$$\mathcal{G}_{Y,Y'}^{N,M} = \sum_{j=0}^{\infty} \mathcal{B}_j^{N,M} \chi_{|N|+|M|-j}(Y_r) F_j\, \delta_{Y_C',Y_C}\,. \tag{4.9}$$

Here Y_C and Y_r are COM and relative guiding centers respectively and the $\delta_{Y_C,Y_C'}$ term captures conservation of COM guiding center during a scattering

event, and

$$\chi_j(Y) = \varphi_j\left(-\frac{Y}{\sqrt{2}\ell}\right) \tag{4.10}$$

is associated with relative Landau level wavefunction. The F_j pair-potential strength parameter in Eq. 4.9 are dependent on the details of the vortex lattice of the host superconductor and the proximity coupling process, but are expected to be dominated by the $j = 0$ (minimum center-of-mass kinetic energy) term. The $\mathcal{B}_j^{N,M}$ define the unitary transformation of pair states from single-particle to COM and relative coordinates:

$$\mathcal{B}_j^{N,M} = \sum_{m=0}^{j} (-)^{M-m} \sqrt{\frac{{}^jC_m \, {}^MC_m \, {}^NC_{j-m} \, {}^{N+M-j}C_{M-m}}{2^{N+M}}}\,, \tag{4.11}$$

where ${}^nC_k = n!/[k!(n-k)!]$ is a binomial coefficient, N and M are single-particle Landau level indices, and j, $N + M - j$ are the COM and relative Landau level indices [69, 70] In vortex lattice states the COM Landau level decomposition is dominated by the $j = 0$ channel over a broad range of perpendicular magnetic field strengths, as can be verified using semi-classical solutions of the non-linear Ginzburg-Landau equation [71, 69]. Truncating the pair Hilbert space to $j = 0$ simplifies the BdG calculations described below, mainly by reducing the number of parameters needed to specify the pair potential to one strength parameter.

4.2 Vortex lattice states

As mentioned above, the thin film superconductor responsible for proximitized superconductivity will form a vortex lattice phase over a broad range of perpendicular magnetic field below H_{c2}. Figure 4.2 shows some typical vortex lattices considered in this chapter. We will show that the vortex lattices shown in Fig. 4.2 (a)-(b) fall in the same class and do not allow odd $\mathbb{Z}$ topological superconducting phase, while vortex lattices shown in Fig. 4.2(c)-(d) can allow odd $\mathbb{Z}$ topological superconducting phase. As we will explain further below, the way in which translational symmetry is used to block-diagonalize the BdG Hamiltonian depends on the precise lattice structure. Assuming that the COM

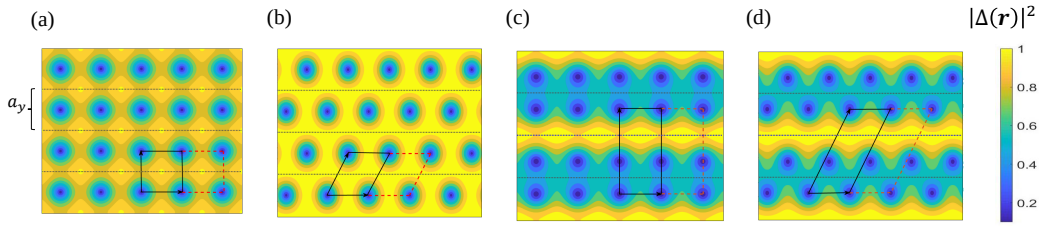

Figure 4.2: Vortex lattice structure in two-dimensions: The contributions to the BdG Hamiltonian from adjacent guiding centers couple distinct sets of pairs as explained in the main text. The solid-black arrows indicate primitive vortex lattice vectors: $\vec{a}_1$ and $\vec{a}_2$. The unit cell area they define is indicated by the solid black-lines. The extended area enclosed by including the dashed-red line is the unit cell in which the BdG Hamiltonian is diagonalized, the dotted horizontal lines indicate the positions of the guiding centers $Y = ta_y$ at which the pair amplitude is non-zero. (a)-(b) Two examples of $q = 1$ (see main text) odd-flux vortex lattices which have $|\Delta_t| = |\Delta_{t+1}| = \Delta_0$. (c)-(d) Two examples of $q = 2$ even-flux vortex lattices in which $|\Delta_t| \neq |\Delta_{t+1}|$. Figure reproduced from the research article arXiv:1903.12249.

Landau level index is $j = 0$, and choosing a Landau gauge with guiding center orbitals extended along one of the primitive lattice vectors of the vortex lattice, it can be shown that the pair amplitude can be non-zero only on a set of equally spaced pair guiding centers: $Y = ta_y$, where t is an integer. For short-range interactions the resulting pair potential has the form [70],

$$\Delta(\boldsymbol{r}) = \sum_t \Delta_t \, \phi_{0,\sqrt{2}ta_y}(\sqrt{2}\boldsymbol{r}) \, . \tag{4.12}$$

Here $t \in \mathcal{Z}$ varies over integers and the dependence of Δ_t on t determines the vortex lattice structure.

In general, the pair potential can not have full lattice translational symmetry and the vortex lattice translational symmetry can only be defined on the translational symmetries of the magnitude of the pair potential in Eq. 4.12. Such functions are called quasi-periodic. For translation λa_x in the x-direction

where λ varies continuously and qa_y in the y-direction where $q \in \mathcal{Z}$,

$$|\Delta(x+\lambda a_x, y+qa_y)| = [\sum_{t,t'} \Delta^*_{t'+q}\Delta_{t+q} \mathrm{e}^{2i(t-t')\lambda\frac{a_x a_y}{\ell^2}} \times \varphi_0\left(\frac{\sqrt{2}}{\ell}(y-t'a_y)\right)\varphi_0\left(\frac{\sqrt{2}}{\ell}(y-ta_y)\right)]^{1/2}. \tag{4.13}$$

For $\lambda = 1$ and $q = 0$ the translation is by a_x in the x-direction. When $a_x a_y = \pi\ell^2$, the magnitude of the pair potential is invariant under this translation, *i.e.* $|\Delta(x+a_x, y)| = |\Delta(x, y)|$. In fact with our gauge choice the pair potential itself is invariant for a pure x-translation by a_x, without taking the absolute value. It follows that $\vec{a}_1 = a_x\hat{x}$ is one of the two primitive lattice vectors of the vortex lattice. For $q \neq 0$, the magnitude of the pair potential after translation along the y-direction is

$$|\Delta(x+\lambda a_x, y+qa_y)| = [\sum_{t,t'} \Delta^*_{t'+q}\Delta_{t+q} \mathrm{e}^{2i(t-t')\lambda\pi} \times \varphi_0\left(\frac{\sqrt{2}}{\ell}(y-t'a_y)\right)\varphi_0\left(\frac{\sqrt{2}}{\ell}(y-ta_y)\right)]^{1/2}. \tag{4.14}$$

In general translational symmetry in the y-direction must be accompanied by translation in the x-direction; *i.e.* the second vortex lattice primitive vector need not be perpendicular to the first. Further, for this particular Landau gauge choice, only the absolute value of the pair potential can be made invariant under the second translation, while the actual pair potential picks up a phase. When Δ_t is independent of t, invariance occurs for $q = 1$ and $\lambda = 0$ so that the second translation vector is $a_y\hat{y}$ and the vortex lattice is rectangular (the special case of $a_x = a_y$ in this class is the square vortex lattice). We define q as the minimum non-zero integer required to satisfy $|\Delta(x+\lambda a_x, y+qa_y)| = |\Delta(x, y)|$. For general λ and q, periodicity is achieved when

$$\Delta_{t+q} = \mathrm{e}^{-i2\pi\lambda t}\mathrm{e}^{i\theta}\Delta_t\,, \tag{4.15}$$

is satisfied for some value of θ. For example $q = 1$ and $\lambda = 1/2$ yields

$$\Delta_t = \mathrm{e}^{-i\pi(t-1)}\mathrm{e}^{i\theta}\Delta_{t-1} = \mathrm{e}^{-i\frac{\pi}{2}t^2}\mathrm{e}^{i(\frac{\pi}{2}+\theta)t}\Delta_0\,, \tag{4.16}$$

which defines a triangular vortex lattice. The specific choice of $\theta = -\pi/2$ gives the familiar expression $\Delta_t = \exp(-i\pi t^2/2)\Delta_0$ often used for a triangular vortex lattice. The second primitive lattice vector is then $\vec{a}_2 = \lambda a_x \hat{x} + q a_y \hat{y}$. The vortex lattice unit cell has area $\hat{z} \cdot (\vec{a}_1 \times \vec{a}_2)$, and contains q superconducting flux quanta. Below, we refer to vortex lattices as even or odd, depending on whether q is even or odd. Theoretically, $q = 1$ odd vortex lattices are the most commonly studied.

In anticipation of the vortex lattice symmetry properties explained in the previous paragraph, we partition guiding centers Y into discrete and continuous contributions by writing $Y = sa_y + y$ where $s \in \mathcal{Z}$ and $y \in [0, a_y)$. Since we are considering pairing in Dirac systems in the quantum Hall limit, we express H_{BdG} first in the Dirac-Landau level guiding center basis. The BdG equations then take the form

$$(\xi_N - \mu)u_{N,s}(y) + \sum_{M,s'} \mathcal{F}^{N,M}_{s,s'}(y) v_{M,s'} = E u_{N,s}(y)\,, \tag{4.17a}$$

$$\sum_{M,s'} (\mathcal{F}^{M,N}_{s',s}(y))^* u_{M,s'}(y) + (\mu - \xi_N) v_{N,s}(y) = E v_{N,s}(y)\,. \tag{4.17b}$$

Here we have transformed from expansion over non-relativistic 2DEG-Landau levels in Eq. 4.6 to the Dirac-Landau levels. Consequently, for $j = 0$ pairing we find that (See appendix C, Eq. C.7)

$$\mathcal{F}^{N,M}_{s,s'}(y) = \sum_t \Delta_t \mathcal{D}^{N,M}_0 \delta_{s+s',2t} \chi_{|N|+|M|-1}((s-s')a_y + 2y)\,, \tag{4.18}$$

with

$$\mathcal{D}^{N,M}_0 = S_M \mathcal{B}^{|N|,|M|-1}_0 - S_N \mathcal{B}^{|N|-1,|M|}_0\,. \tag{4.19}$$

Note that s-wave pair potentials do not pair electrons that are both in $N = 0$ Dirac-Landau levels, which are spin-polarized. However, an electron in the zeroth Dirac-Landau level ($N = 0$) does pair with electrons from higher Dirac-Landau levels ($M \neq 0$).

Equation 4.17 organizes the degrees of freedom into guiding center stripes, with each stripe labeled by an integer s, and the guiding centers within a stripe labeled by a continuous variable y. We note in Eq. 4.18 that pairing is allowed

only between stripes that have indices that are both odd or both even ($\delta_{s+s',2t}$ term). This property implies that odd and even stripe indices decouple in the BdG equation; *i.e.* we can block diagonalize the entire BdG Hamiltonian into two susbsystems distinguished by whether the stripe index is even or odd. We prove in the next paragraph that when $|\Delta_t| = |\Delta_{t+q}|$ and q is odd, the even and odd s subsystem spectra are identical. This distinction between vortex lattice classes plays a major role in distinguishing topological superconducting phases. We will show that only the even flux vortex lattices allow odd-$\mathbb{Z}$ chiral topological superconducting phases.

For an odd value of q, we can write $q = 2p + 1$, where $p \in \mathcal{Z}$. We now examine how the pairing matrix elements in the odd subsystems are related to the pairing matrix elements in the even subsystems. From Eq. 4.15 and Eq. 4.18

$$\mathcal{F}^{N,M}_{2n+1,2m+1} = \mathrm{e}^{-i2\pi\lambda(n+m-2p)}\mathrm{e}^{i\theta}\mathcal{F}^{N,M}_{2(n-p),2(m-p)}\,, \tag{4.20}$$

where n, $m \in \mathcal{Z}$. Note that $s = 2n + 1$ and $s' = 2m + 1$ are odd subsystem stripe indices, and $2(n - p)$ and $2(m - p)$ are even subsystem stripe indices. Using Eq. 4.17, the BdG eigenvalue equations for the odd subsystem can be written as,

$$\begin{aligned}(\xi_N - \mu)u_{N,2n+1}(y) \; + \; & \sum_{M,m}[\mathcal{F}^{N,M}_{2(n-p),2(m-p)}(y) \\ & \times \mathrm{e}^{-i2\pi\lambda(n+m-2p)}\mathrm{e}^{i\theta}v_{M,2m+1}] = Eu_{N,2n+1}(y)\,, \qquad (4.21a)\\ \sum_{M,m}[(\mathcal{F}^{M,N}_{2(m-p),2(n-p)}(y))^*\mathrm{e}^{i2\pi(n+m-2p)i}\mathrm{e}^{-i\theta}u_{M,2m+1}(y)] & \\ + (\mu - \xi_N)v_{N,2n+1}(y) = Ev_{N,2n+1}(y)\,. \qquad (4.21b)\end{aligned}$$

After the unitary transformation $(\bar{u}_{N,2n+1},\, \bar{v}_{N,2n+1})^T = S_n(u_{N,2n+1},\, v_{2n+1})^T$ with

$$S_n = \begin{pmatrix} \mathrm{e}^{i\theta/2}\mathrm{e}^{2i\pi\lambda(n-p)} & 0 \\ 0 & \mathrm{e}^{i\theta/2}\mathrm{e}^{-2i\pi\lambda(n-p)}, \end{pmatrix} \tag{4.22}$$

the BdG eigenvalue equations are transformed to,

$$(\xi_N - \mu)\bar{u}_{N,2n+1}(y) + \sum_{M,m} \mathcal{F}^{N,M}_{2(n-p),2(m-p)}(y)\bar{v}_{M,2m+1} = E\bar{u}_{N,2n+1}(y)\,, \quad (4.23a)$$

$$\sum_{M,m}[(\mathcal{F}^{M,N}_{2(m-p),2(n-p)}(y))^*\bar{u}_{M,2m+1}(y)] + (\mu - \xi_N)\bar{v}_{N,2n+1}(y) = E\bar{v}_{N,2n+1}(y)\,, \quad (4.23b)$$

which are identical to those of the even subsystem. Hence, the odd and even subsystems for an odd-q vortex lattice are equivalent. It is easy to see this degeneracy between odd and even subsystem is in general lifted in case of even-q vortex lattices, since there is then no similarity relation like Eq. 4.20.

In the limit $\Delta(\boldsymbol{r}) \to 0$, the system has continuous magnetic translation symmetry. In anticipation of the symmetries of the class of vortex lattice states that we wish to consider, we can exploit the discrete magnetic translational symmetry that remains by choosing unit cells that contain integer numbers of *electron* magnetic flux quanta. To be concrete we choose $A_x A_y = 2q\pi\ell^2$, where $A_x = 2a_x$ and $A_y = qa_y$. With this choice the BdG problem for any general vortex lattice can be block diagonalized in a magnetic Bloch state basis set:

$$\phi_{N,n,\boldsymbol{k}}(\boldsymbol{r}) = \sqrt{\frac{qa_y}{L_y}} \sum_t \mathrm{e}^{ik_y(qt+n)a_y}\mathrm{e}^{i\pi\lambda qt(t-1)/2}\mathrm{e}^{i(\pi\lambda n - \theta/2)t}\phi_{N,k_x\ell^2+(qt+n)a_y}(\boldsymbol{r})\,. \quad (4.24)$$

where integer $n \in [0, .., q-1]$ and $\boldsymbol{k} = (k_x,\, k_y)$ is a Bloch wave vector with $k_x \in [0,\, \pi/a_x)$ and $k_y \in [0,\, 2\pi/qa_y)$. The pairing in magnetic Bloch basis is a $q \times q$ matrix for every pair of Landau level indices N, M of pairing electrons:

$$\mathcal{F}^{N,M}_{n,m}(\boldsymbol{k}) = \mathcal{D}^{N,M}_0 \sum_t \Delta_{qt+(m+n)/2}\, \mathrm{e}^{-i\pi\lambda qt(t-1)}\mathrm{e}^{-i(2\pi\lambda n-\theta)t}\mathrm{e}^{ik_y a_y(2qt+n-m)} \times \chi_{|N|+|M|-1}((2qt+n-m)a_y + 2k_x\ell^2)\,. \quad (4.25)$$

Since Δ_t is only non-zero on integer values of t, the pairing matrix element in $\boldsymbol{k}$-space is only non-zero when n and m are either both even or both odd. Based on the arguments used to prove the degeneracy for odd-flux vortex lattice, *i.e.* $q = 2p+1$ from the real space picture, the degeneracy can also be proven in the $\boldsymbol{k}$-space picture here. More precisely, in the even-odd block diagonalized

system, the odd system with $n = 2s + 1$ and $m = 2s' + 1$ at $\boldsymbol{k} = (k_x, k_y)$ is degenerate with the even system with $n = 2(s - p)$ and $m = 2(s' - p)$ at $\boldsymbol{k} = (k_x, k_y + \frac{\pi}{2qa_y})$. The algebra and linear transformation to show that follows exactly like Eq.4.20-4.23. Now, we have formally proven that for the system in consideration here, 2D vortex lattices have distinct classification into odd-flux and even-flux vortex lattice. Where only the even-flux vortex lattice can host odd-$\mathbb{Z}$ topological superconducting phase.

To simplify the further discussion related to degeneracy in the spectrum, first note that irrespective of type of vortex lattice, the pairing matrix element in Eq. 4.25 has an important translational property:

$$\mathcal{F}^{N,M}_{n,m}(k_x, k_y + \pi/a_y) = \mathcal{F}^{N,M}_{n,m}(k_x, k_y)\,. \tag{4.26}$$

For $q = 1$ vortex lattices the period is half the reciprocal lattice vector. This implies that the BdG spectrum at a point $\boldsymbol{k_0} = (k_{x0}, k_{y0})$ is identical to the spectrum at $\boldsymbol{k_1} = (k_{x0}, k_{y0} + \pi/a_y)$. For the simplest even flux vortex lattices (*i.e.* $q = 2$), the reciprocal space lattice vector length along k_y is equal to π/a_y, and this degeneracy is not present.

4.3 Bulk picture

Having established all the necessary framework and formal proofs related to distinction between the BdG spectral degeneracies of even and odd flux vortex lattices, next we focus on some numerical results. We discuss how spectra depend on the number of Landau levels contained within a pairing window. We will discuss the cases of pairing within one Landau level, two Landau levels, and many Landau levels separately. Since the main goal is to address the connection between vortex lattice structures and the topological phases, we study $q = 2$ vortex lattices as the simplest example of the even flux vortex lattices and compare with $q = 1$ odd-flux vortex lattices. In addition, we restrict our attention to the $\lambda = 0$ and $\lambda = 1/2$ cases, which for $q = 1$ give square and triangular vortex lattices respectively. The generality of the results obtained from these specific choice of parameters is ensured by the formal proof presented in last section. For the most part, we will be solving

the BdG matrix equation:

$$(\xi_N - \mu)u_{N,n}(\boldsymbol{k}) + \sum_{M,m} \mathcal{F}^{N,M}_{n,m}(\boldsymbol{k}) v_{M,m}(\boldsymbol{k}) = E(\boldsymbol{k}) u_{N,n}(\boldsymbol{k})\,, \tag{4.27a}$$

$$\sum_{M,m} (\mathcal{F}^{N,M}_{n,m}(\boldsymbol{k}))^* u_{M,m}(\boldsymbol{k}) + (\mu - \xi_N) v_{N,n}(\boldsymbol{k}) = E(\boldsymbol{k}) v_{M,m}(\boldsymbol{k})\,, \tag{4.27b}$$

for $q = 1$ and $q = 2$. For the case of $q = 1$ we will often not use subscript n, m indices.

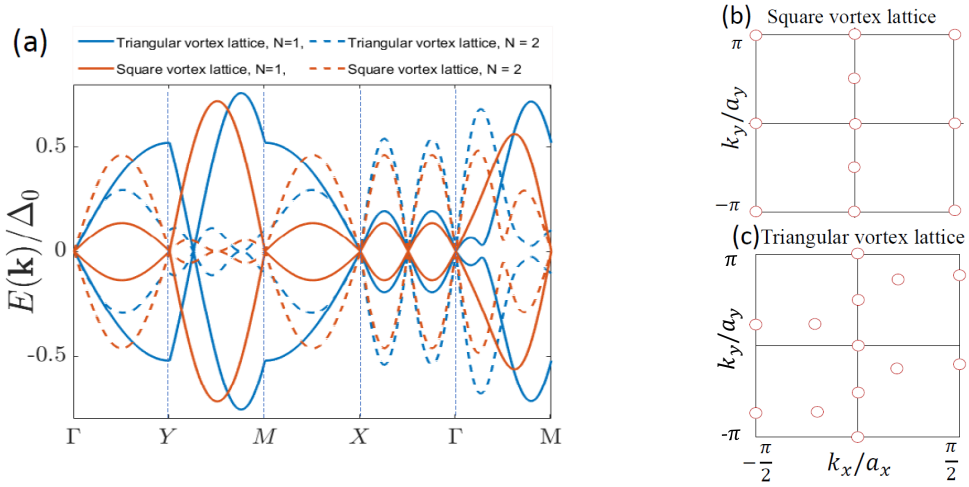

Figure 4.3: (a) Bogoliubov quasiparticle spectrum with the BdG operator projected onto the $N = 1$ and $N = 2$ Landau levels for triangular (blue) and square (red) vortex lattices. (b)-(c) Band- touching Dirac point positions for pairing in $N = 1$ Dirac Landau levels for square and triangular vortex lattices. The band touching points at $(k_{x0},\, k_{y0})$ are equivalent to those at $(k_{x0}, k_{y0} + \pi/a_y)$. Figure reproduced from the research article arXiv:1903.12249.

4.3.1 Pairing within a single Landau level

The simplest example of superconductivity in the quantum Hall regime is the case in which only one Landau level lies within the pairing window. This limit is relevant if a regime can be achieved in which the Landau level separation is larger than the Debye pairing window energy E_D of the parent

superconductor and at the same time magnetic field weaker than its upper critical field H_{c2}. This is, of course, not a regime that is frequently achieved, but is more accessible when the proximitized system has a Dirac spectrum with widely spaced low energy Landau levels that a parabolic system with equally spaced Landau levels. Because of Landau level truncation, the BdG spectrum in this limit is simply given by

$$E(\boldsymbol{k}) = \pm\sqrt{(\xi_N - \mu)^2 + |\mathcal{F}^{N,N}(\boldsymbol{k})|^2}\,. \tag{4.28}$$

When the relevant Landau level energies are aligned with the chemical potential, quasiparticle energies vanish whenever $\mathcal{F}^{N,N}(\boldsymbol{k}) = 0$. The positions in momentum space at which the energies vanish are then related to the zeros of the Hermite polynomials associated with the pairing Landau level, as noted previously [72] in relation to spinless pairing in the zeroth-Landau level. Since the spectrum in this limit is always gapless at some isolated $\boldsymbol{k}$ points, the relevant the system is in a "semi-metallic" phase of the Bogoliubov quasiparticles. For the simplest case of pairing in the $N = 1$ Dirac Landau level, all the band touching points are Dirac like as seen in Fig. 4.3. If pairing is in $N > 1$ Dirac Landau level, as illustrated in Fig. 4.3(a), both linear and quadratic band touching points occur. For odd q flux lattices each band touching point that appears in the interval $[-\pi/qa, 0)$ are replicated in the interval $[0, \pi/qa)$, as explained in the previous section.

To further explore the topological nature of the physics in this regime we first assume μ to be slightly away from ξ_N, so that spectrum becomes gapped. Next, we write an effective 2×2 low energy effective Hamiltonian describing the system near the previously (when $\xi_N \approx \mu$)band touching points,

$$H^{\text{eff}}_{BdG} \sim \begin{pmatrix} -\mu & (\alpha k_y \pm i\beta k_x)^\gamma \\ (\alpha k_y \mp i\beta k_x)^\gamma & \mu \end{pmatrix}. \tag{4.29}$$

Here k_x, k_y are measured relative to some point $\boldsymbol{k}_0$ in BZ, where $\mathcal{F}^{N,N}(\boldsymbol{k}_0) = 0$, we have chosen the zero of energy to be the single-particle energy of the relevant Landau level and the $\pm$ sign allows either chirality for the Dirac points, and the power γ is lowest order for which

$$\left.\frac{\partial^\gamma \mathcal{F}^{N,N}(\boldsymbol{k})}{\partial k^\gamma_{x/y}}\right|_{\boldsymbol{k}=\boldsymbol{k}_0} \neq 0\,, \tag{4.30}$$

for example $\gamma = 1$ for Dirac band touching and $\gamma = 2$ for quadratic band touching in the limit $\mu = \xi_N$. In Eq. 4.29 and α and β are constants that depend on the Fermi velocity of the low energy Bogoliubov quasiparticle at $\boldsymbol{k}_0$. The use of different α and β allows for the anisotropies in band touching point velocities that can be seen in Fig. 4.3(a). The Landau level is partially occupied when $|\mu| \lesssim \Delta_0$. For Dirac band touching, the low energy H^{eff}_{BdG} in Eq. 4.29 resembles the BdG matrix of a spinless p-wave superconductor near the critical point of topological phase transition. The two topologically distinct phases are distinguished by the sign of μ. When μ is tuned through zero, gaps close and reopen and the system experiences topological phase transitions at which the total Chern number changes. In finite systems, the number of edge state channels also changes, as we discuss later. For odd q, Dirac points appear in pairs and both Chern numbers, and as we show explicitly later, the numbers of edge channels change by an even integers when these Dirac points appear. The quadratic band touching points relevant to pairing in higher Landau levels can be analyzed in a similar way.

4.3.2 Two Landau-level model

In the previous section we discussed topological phase transitions driven by varying the chemical potential μ in a system with a single Landau level in the pairing window. In real physical systems it is the carrier density that is controlled by gate voltages, not μ, and μ changes irregularly with magnetic field strength. For example at $T = 0$ and in the absence of pairing, μ changes discontinuously, jumping from being pinned at one Landau level energy to begin pinned at another. The minimal model that incorporates that consequence of the strongly peaked densities of states of Landau level systems is a model with two Landau levels in the pairing window. A $q = 1$ two Landau level system has a 4×4 BdG Hamiltonian which makes it possible to obtain closed form expressions for eigenvalues, which are however not especially transparent. However, the important insight is that by tuning Δ or Landau level gap one can close and open BdG gaps.

In the absence of superconductivity, the system is always a gapped quantum Hall insulator. In principle, the gap closings and topological phase transitions can be driven either by varying the pairing strength Δ_0, or by using

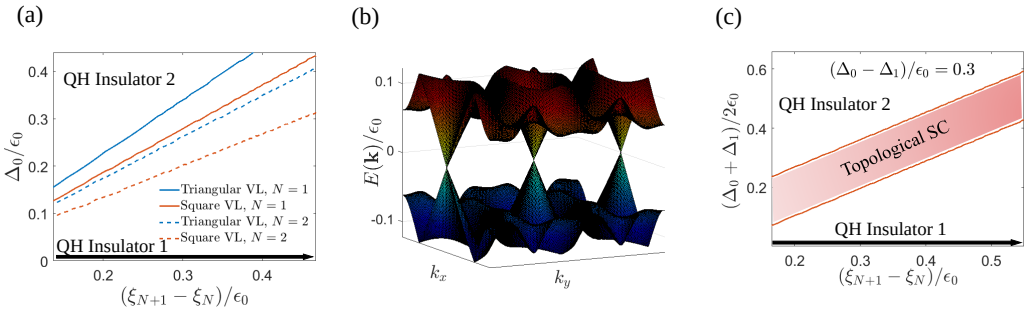

Figure 4.4: Model with two Dirac Landau levels : Energies are shown in the $\epsilon_0 = v_F\sqrt{2e\hbar}$ units and ξ_N is N^{th} Landau level energy. (a) Superconducting pairing strength Δ_0 that leads to the first gap closing as a function of Landau level separation for two Landau level models of the $q = 1$ vortex lattices in Fig. 4.2 (a)-(b). In these calculations the μ has been placed halfway between Landau levels so that the lower Landau level is completely occupied and the higher Landau level empty in the absence of pairing. Band touchings are accompanied by transitions between a quantum Hall (QH) insulator 1 and another QH insulator 2 state, both of which have an even number of chiral Bogoliubov edge states. (b) Quasi-particle spectrum at a gap closing point for $q = 1$ square vortex lattice. In this case there are two Dirac like gap closing points in the first Brillouine zone. (c) When the vortex lattice symmetry is lowered by setting the pairing strength Δ_t to different values in odd and even stripe regions, giving the vortex lattice illustrated in Fig. 4.2 (c)-(d), an intermediate chiral topological superconductor (SC) [red region] phase appears with an odd number of chiral Majorana edge modes. Figure reproduced from the research article arXiv:1903.12249.

magnetic fields to tune the energy separation between Landau levels, as shown in Fig.4.4 (a). The value of Δ_0 at which gap closes, scales with the Landau level separation. The circumstance is closely analogous to the case of proximity superconductivity induced in the surface states of magnetically doped TIs, the system that hosts the only established experimental example of a quantum anomalous Hall state. In that case an intermediate topological superconducting phase appears when the surface state exchange fields are reversed to drive the system between two different quantum Hall insulators [25]. Based on this analogy one would expect that the first gap closing to occur as Δ_0 increases to convert the quantum Hall insulator into a chiral topological superconductor odd-$\mathbb{Z} = 1$. Here though the topological phase diagram depends on the type of vortex lattice. In Fig. 4.4 (a) the gap closing lines mark phase transitions between quantum Hall Insulators. The $\Delta_0 \to 0$ limit in this case is a quantum Hall state with a full $N = 1$ Landau level, and as we discuss later in Sec. 4.4, two chiral edge states in the doubled BdG Hilbert space. Once the pairing is turned on the system no longer has quantized Hall conductance, however, it is still adiabatically connected to a quantum Hall insulator and has two edge channels as long as the gap does not close. The difference compared to the quantum anomalous Hall case appears when the gap closes and reopens. In the quantum anomalous Hall model the Dirac-like gap closings occur only at the Γ-point in momentum space and are generically accompanied by odd integer changes in the topological $\mathbb{Z}$-index. One of the two BdG doubled quantum Hall edge states survives. This is the single chiral Majorana edge mode, and is expected to yield a half quantized conductance plateau in transport experiments [73]. The BdG spectrum is determined by $\mathcal{F}^{N,M}(\boldsymbol{k})$. As mentioned earlier, for odd flux vortex lattice, each energy has even number of $\boldsymbol{k}$s. Band crossings therefore always occur in pairs as illustrated in Fig. 4.4 (b). This leads to the important conclusion that in the quantum Hall transition for odd-flux vortex lattices, the $\mathbb{Z}$-index always changes by an even integer, and the number of edge channels changes by two or multiples of two. This conclusion will be confirmed using explicit edge state calculations in Sec. 4.4.

To achieve a chiral topological superconducting phase with an odd number of edge modes, one needs to break this degeneracy between the even and odd s subsystems. The simplest way is to allow different pairing amplitudes, Δ_0

and Δ_1, for even and odd index stripes. With this choice

$$\mathcal{E}^{N,M}_{s,s'}(y) = \Delta_0 \mathrm{e}^{i\theta(s+s')^2} \mathcal{D}^{N,M}_0 \chi_{|N|+|M|-1}((s-s')a_y + 2y)\,, \tag{4.31a}$$

$$\mathcal{O}^{N,M}_{s,s'}(y) = \Delta_1 \mathrm{e}^{i\theta(s+s')^2} \mathcal{D}^{N,M}_0 \chi_{|N|+|M|-1}((s-s')a_y + 2y)\,. \tag{4.31b}$$

The $\boldsymbol{k}$-space picture is modified by block diagonalizing the BdG matrix Eq. 4.27 in the odd and even system and halving the Brillouine zone along k_y such that $k_y \in [0, \pi/a_y)$, since this lowers the translation symmetry, such that the smallest repeating unit cell now contains two electronic flux quanta. The matrix takes the following form,

$$M_{BdG}(\boldsymbol{k}) = \begin{pmatrix} M^o_{BdG}(\boldsymbol{k}) & 0 \\ 0 & M^e_{BdG}(\boldsymbol{k}) \end{pmatrix}. \tag{4.32}$$

A change in topological index from even to odd cases occurs when a gap closes in only one of the two blocks. Once the degeneracy between odd and even system is broken, the gap closings generically occur at different values of magnetic field in the even s and odd s blocks. The region between the subsystem gap closings is shaded in red in Fig. 4.4 (c). We identify this region as having a chiral topological superconductor state and an odd number of Majorana edge modes.

4.3.3 General model with Debye cut-off

In a realistic model the number of Landau levels in the pairing window increases with decreasing magnetic field strength. In the normal state the number of Landau level below the Fermi level is inversely proportional to magnetic field and successive crossings between the Landau levels and the Fermi energy leads to gap changes and jumps in Hall conductance. Here we show that for finite pairing there are extra gap closing points associated with each Landau level crossing, implying extra topological phase transition points. However, for the case of odd-q vortex lattices, all these phase transitions involve simultaneous gap closing at two different points in momentum space and connect one quantum Hall insulator state with another. Once the pairing amplitude is allowed to take different values in even and odd striped regions, yielding a $q = 2$ vortex lattice, band crossings occur singly. In the example illustrated in

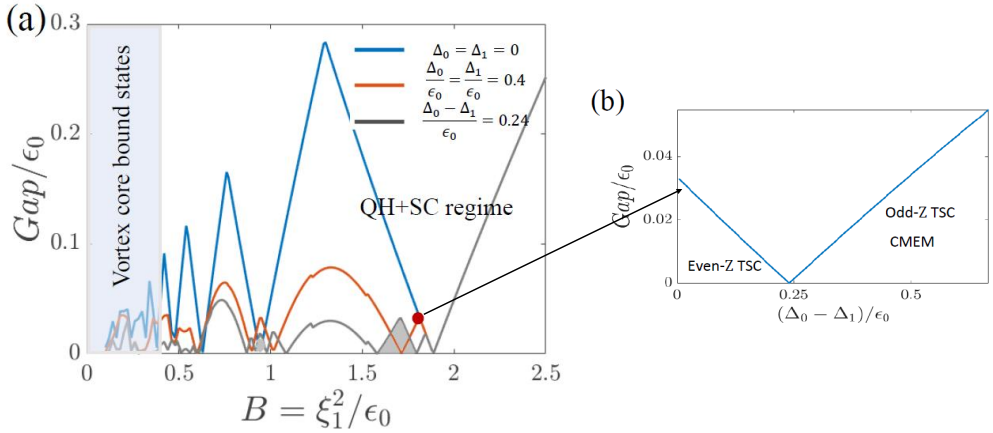

Figure 4.5: Bogoliubov quasiparticle gaps (in the $\epsilon_0 = v_F\sqrt{2e\hbar}$ units), (a) as a function of magnetic field strength. Here $\mu = 1.35\epsilon_0$ and a hard Debye cutoff window of $E_D = 1.1\epsilon_0$ is fixed. As the magnetic field is varied the Landau levels which host pairing change. The blue curve shows Landau level energies relative to the Fermi level in the limit of no pairing. The gap vanishes when the relevant Landau level crosses the Fermi energy. The plot shows Dirac Landau levels with decreasing indices crossing the Fermi level, reaching index $N = 1$ at the last zero of the blue curve. The red curve plots gaps as a function of magnetic field strength in a $q = 1$ vortex-lattice, *i.e.* for a case with equal pairing strength in even s and odd s channels. Extra gap closings occur as paired Landau levels cross through the Fermi level, but occur in pairs so that the transitions are between one quantum Hall (QH) insulator and another. The grey line calculations is for an $q = 2$ vortex lattice in which the pairing strength is different for even and odd values of s. Even q allows a chiral topological superconductor (TSC) phase to emerge in the regions that are shaded gray. In the shaded blue region towards on left hand side of the figure, the Landau level structure is destroyed by pairing and the low energy states are most simply viewed as hybridized vortex core bound states. (b) Gap as a moving from odd-flux to even-flux vortex lattice by tuning $\Delta_0 - \Delta_1$. Starting from an even-$\mathbb{Z}$ phase shown by red dot in (a), as $\Delta_0 - \Delta_1$ is tuned keeping everything else fixed, extra gap closing occurs, beyond which, one reaches odd-$\mathbb{Z}$ phase. The odd-$\mathbb{Z}$ phase can be further broadened with tuning $\Delta_0 - \Delta_1$. Figure reproduced from the research article arXiv:1903.12249.

Fig. 4.5 the gray regions show the fields strengths where the ground state is a chiral topological superconductor. The extent of the chiral topological superconducting phases can be tuned by varying $\Delta_0 - \Delta_1$. At weak magnetic fields, the Landau level gap is much smaller than Δ_0, there are many Landau levels within the Debye pairing window, and the low energy quasiparticles are best viewed as bands formed by hybridizing vortex core bound states associated with different vortices. In case of Dirac model, these vortex core bound states at weak magnetic field are Majorana zero modes[74, 75], since the Dirac model proximity coupled to an s-wave superconductor under time reversal symmetry is the famous Fu-Kane model [22]. For the 2DEG case at weak field limit, the low energy vortex core bound states are not Majorana. In that sense, the low field sector indicated by the shaded blue region in Fig. 4.5 is dramatically different for Dirac model and ordinary 2DEG model when proximity coupled to an s-wave superconductor, but is not the focus of this work (See Appendix E for comparison between Dirac and ordinary 2DEG). However, the high field sector in quantum Hall regime is qualitatively same.

4.4 Edge state picture

In this section we discuss the BdG spectrum of finite width stripes to establish bulk-edge correspondence and demonstrate the presence of chiral Majorana edge modes. In the continuum Dirac model we employ, we have defined the stripes by adding a smooth confining potential around the edge of the sample and truncating the Hilbert space to the two Dirac Landau levels. In doing so, we have assumed that edge states from Landau levels which are not in the pairing window but may be active at the Fermi level do not play a role. The BdG equations then take the following form:

$$\left[\xi_N - \mu + U_s(k_x)\right] u_{N,s}(k_x) \; + \sum_{M,s'} \mathcal{F}^{N,M}_{s,s'}(k_x) v_{M,\boldsymbol{Y'}} = E u_{N,s}(k_x)\,, \tag{4.33a}$$

$$-\left[\xi_N - \mu - U_s(-k_x)\right] v_{N,s'}(y) \; + \sum_{M,\boldsymbol{Y'}} (\mathcal{F}^{N,M}_{s,s'}(k_x))^* u_{M,s'}(k_x) = E v_{N,s'}(k_x)\,. \tag{4.33b}$$

Here, the smooth confining is specified by letting

$$U_s(k_x) = \begin{cases} 0 & |s| \leq S_{bulk}\,, \\ U_0(sa_y + k_x\ell^2) & |s| > S_{bulk}\,. \end{cases} \tag{4.34}$$

Here U_0 sets the strength of confining potential and $S_{bulk} \in \mathcal{Z}$ sets the width of the bulk part of the stripe.

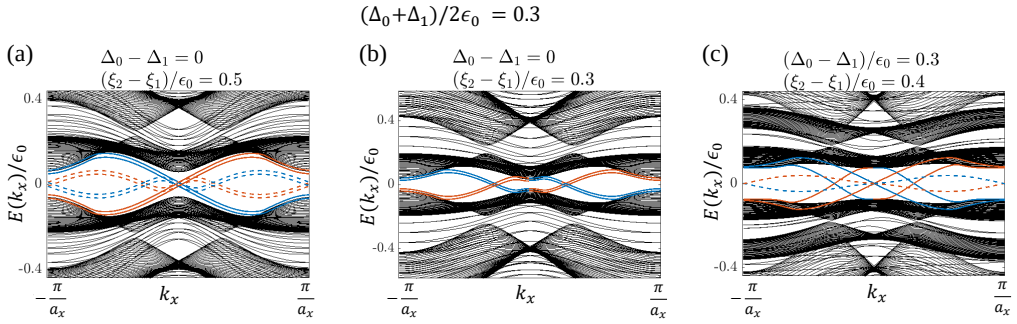

Figure 4.6: Stripe geometry spectrum (in $\epsilon_0 = v_F\sqrt{2e\hbar}$ units) showing edge states in the gaps between Landau levels. States localized at opposite edges are distinguished by color (blue and red). Note that some edge states appear that are not related to the bulk topology. These are not present at all energies, do not flow between bulk bands, and are distinguished by drawing them with dashed lines. (a) Triangular $q = 1$ vortex lattice. At this magnetic field strength the system has two chiral modes on each edge, corresponding to BdG doubling of the $N = 1$ quantum Hall effect. (b) Triangular $q = 1$ vortex lattice at a weaker magnetic field. The system now has four chiral modes on each edge, corresponding to a BdG doubling of the $N = 2$ quantum Hall effect. (c) For a $q = 2$ vortex lattice, $(\Delta_0 \neq \Delta_1)$ there is intermediate gap closing point as magnetic field is varied which opens up an interval of field over which the system hosts three chiral modes on each edge. This phase is topologically connected to chiral topological superconductivity. Figure reproduced from the research article arXiv:1903.12249.

The stripe state calculations shown in Fig. 4.6 correspond to the bulk calculations for the model that retains only the $N = 1$ and $N = 2$ Landau levels. The edge states shown in Fig. 4.6 accurately describe the system when

$\Delta_0 \not\gg \xi_{N+1} - \xi_N$ and the two Landau level model remains valid. Our calculations contain 100 integer s indices. In the absence of pairing the system is a quantum Hall insulator, with edge states at the Fermi level coming from the occupied Landau levels. In the BdG-doubled Hilbert space, these modes are doubled but retain the same chirality due to the combination of particle-hole inversion and momentum label reversal in the hole block of the BdG equations. For weak pairing regime the quantum Hall gaps remain open. The two chiral edge state branches plotted as solid red and blue lines in Fig. 4.6(a), are localized on the left and right edges respectively, and evolve from $N = 1$ Landau level edge states. For the odd q vortex lattices, the bulk calculations discussed in Sec. 4.3.2 and Fig. 4.4 (a) show a topological phase transition. On the other side of the gap closing point the system again has even number of chiral edge states as shown by four chiral edge states in Fig. 4.6(b). This evolution is similar to ordinary quantum Hall edge state evolution, as the magnetic field is decreased, the number of edge states increase, and for finite stripe widths are eventually become indistinguishable from bulk states as $\boldsymbol{B} \to 0$. To induce a topological superconducting phase with odd number of Majorana edge mode, we allow even and odd stripes to take different pairing amplitudes, which breaks the degeneracy between the two subsystems. As the magnetic field strength is decreased, the even and odd subsystem gap closing points move away from each other and the intermediate phase is a topological superconductor that hosts three Majorana edge modes as shown in Fig. 4.6(c).

4.5 Experimental outlook

The relationship established between the vortex lattice configuration and the topological classification of superconducting states evolves from the factor of two difference the magnitudes of the electron and superconducting flux quanta, and from magnetic translation group properties. It is not dependent on the underlying zero-magnetic field electronic structure. We have focused on two-dimensional Dirac bands here because they lead to large Landau level separations at relatively weak magnetic fields, and therefore seem to have the best chance of being compatible with proximity superconductivity in resolved Landau levels.

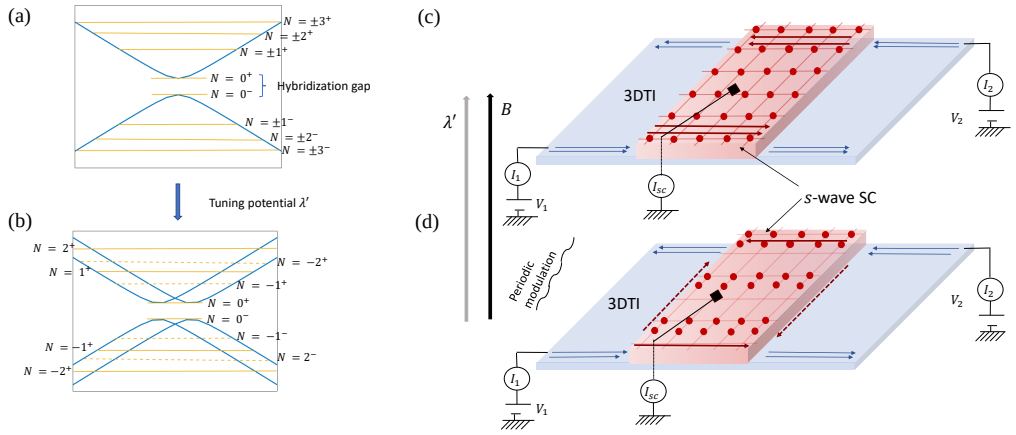

Figure 4.7: Experimental setup for topological superconductivity in the quantum Hall regime (a) Schematic of Landau levels of surface state of a thin film 3D TI with a hybridization gap between two layers. The spectrum is doubly degenerate, (b) The Landau level degeneracy can be broken by a displacement field between the two layers leading to normal state Landau level transitions with odd integer Hall conductance differences, (c) A quantum Hall system proximity coupled to a superconductor (SC) in a $q = 1$ vortex lattice phase, (d) periodic in plane field, the vortex lattice structure can be modified to $q = 2$ vortex lattice. An odd $\mathbb{Z}$ phase emerges in the central superconductor covered region. Figure reproduced from the research article arXiv1903.12249.

Indeed, the first major experimental challenge in exploring this relationship lies in achieving Landau quantization in the regime where superconductivity still survives. When the Landau level separation in a two-dimensional system is comparable to other energy scales, like the proximitized superconducting gap, we can expect edge states to have relatively short localization lengths and to be experimentally accessible via transport experiments. This circumstance is generally referred to as the quantum Hall regime. Dirac systems with large Fermi velocities are ideal for achieving the quantum Hall regime without destroying superconductivity. For monolayer graphene ($v_F \sim 10^6 m/s$) and the Dirac surface states of a 3D TI ($v_F \sim 5\times 10^5 m/s$), the largest Landau level gap already exceeds $10meV$ at $B \sim 1T$. Moreover, superconductivity has recently been successfully induced in both graphene [76, 77, 78, 79] and TIs [23, 80, 24].

The next challenge is to eliminate double degeneracies that the system might possess in the normal state, for example degeneracies associated with spin, since these degeneracies tend to favor even-$\mathbb{Z}$ topological phases. Monolayer graphene has spin and valley degeneracy and very weak intrinsic spin-orbit coupling. Because of these, quantum Hall transitions in monolayer graphene occur in multiples of four (*i.e.* $\sigma_{xy} = e^2(4N+2)/h$) unless spin and valley symmetries are spontaneously broken [81, 82, 83, 84]. This makes monolayer graphene unfavorable for an odd-$\mathbb{Z}$ topological superconductivity phase in the quantum Hall regime. The surface states of a 3D TI thin film are effectively spinless due to strong spin-orbit coupling. However there are two surface states, from top and bottom surfaces, and these supply an extra degeneracy. A gate displacement field will induce a potential difference between top and bottom surfaces, λ', which lifts this final degeneracy and leads to single particle Landau level energies

$$\xi_N^{\pm} = \pm\sqrt{\left(\frac{\lambda'}{2} + S_N \epsilon_0 \sqrt{|N|B}\right)^2 + \lambda^2}\,. \tag{4.35}$$

Here, λ is the hybridization energy between top and bottom layer surface states and $S_N = \pm$ is the surface-dependent Dirac chirality. The potential difference λ' breaks the degeneracy of the N^{th} Landau level by splitting it into N^+ and N^- levels. For a typical 5-6 quintuple layers] thick 3D TI, the layer hybridization energy $\lambda \sim 5-8$ meV allowing a value of λ' on the same scale

to induce clear Landau level separations at around $1T$ field, where thin film Nb-superconductor is well below its H_{c2}.

We propose an external magnetic field generalization, illustrated schematically in Fig. 4.7 (c)-(d), of the magnetized TI experiment of He *et. al.* [26] in which a thin Nb film was deposited on a a thin film of a Cr doped 3D TI, in our proposal the TI is not doped. The working principle of the transport device shown in FIg. 4.7 is discussed in detail in chapter 6 in context of the quantum anomalous Hall normal system. The edge transport equations remain unchanged in the quantum Hall case. In the case of interest here, we propose the entire system is placed under a perpendicular magnetic field, such that the surface states of the 3D TI are in the quantum Hall regime. The edge states indicated in Fig. 4.7 (c), correspond to BdG doubling of the single edge channel expected when one surface state conduction is below the Fermi level. The two edge state channel configuration in the bare TI region is equivalent to one quantum Hall edge state in the absence of pairing. In the region covered with the superconductor, there are two corresponding Bogoliubov edge states. In Fig. 4.7 (d) we imagine that the vortex lattice configuration has been manipulated by spatially varying magnetic field strength, the thickness of the superconducting film, or any other property in a manner that is commensurate with the natural vortex lattice so as to convert from a $q = 1$ vortex lattice to a $q = 2$ vortex lattice. For example a weak in-plane magnetic field, which is made to go through a nearby (but not proximity coupled to the system) bulk superconductor to achieve a spatially periodic magnetic field profile can be used to control the vortex lattice structure in the active system. This is equivalent to tuning $\Delta_0 - \Delta_1$, as studied theoretically in our model calculations. Beyond a critical value of $\Delta_0 - \Delta_1$, the surface that is covered by superconductor can host only one Bogoliubov edge state, as shown in Fig. 4.7 (d). In this configuration, one of the two edge states from the BdG doubled space in the bare TI region is reflected from the superconducting region and the other is transmitted. As argued by Chung *et. al.* [73], such a reduction should lead to a half-quantized longitudinal conductance plateau in two terminal transport measurement. When the Majorana mode is induced by magnetization reversal, it has been argued [64, 65] that a similar half-quantized conduction can result simply from strong disorder. In the present case, vortex lattice manipulation does not introduce additional disorder, in particular in the un-proximitized

regions of the TI. A clear half quantized conductance plateau measured in this way would therefore be a compelling signature of a Majorana edge mode and more importantly an effective 2D spinless $p \pm ip$ superconducting phase.

4.6 Discussion and Conclusion

In this chapter we studied a quantum Hall system obtained under a perpendicular magnetic field, proximity coupled to an s-wave superconductor. We focused our attention to 2D topological superconductivity and possible chiral Majorana edge modes in this regime. We find that vortex lattices with odd number of superconducting flux through the smallest unit cell can not host odd $\mathbb{Z}$ topological superconducting phase. The emphasis on odd $\mathbb{Z}$ phases is put because the topological superconductors with even $\mathbb{Z}$ phases are topologically equivalent to quantum Hall insulator and in the two terminal transport experiments proposed here and in Ref. [73] do not provide a distinct signature for Majorana.

The regime discussed in this chapter is distinct from the usually considered isolated Majorana regime, where the isolated vortices in an effective chiral topological superconductor with p-wave pairing symmetry host a bound Majorana zero-modes [85, 86, 74, 75]. In an external magnetic field a vortex lattice [74, 75] forms and the Majorana modes start to overlap to form low energy Majorana mini-bands, that are initially well separated from higher energy excitations of the superconductor. The limit considered here is reached at still stronger magnetic fields, at which the vortices overlap substantially and the vortex core spectrum is not well separated from rest of other excitations. Moreover, in this limit, most of our results generally apply for Landau levels emerging from non-relativistic 2DEG as well as Dirac electrons. This is important, because in the weak field limit, the ordinary 2DEG coupled to an s-wave superconductor is not an effective p-wave superconductor. We have established a relationship between a classification we introduce for vortex lattice structures, and the topological classifications of superconducting phases which applies in this quantum Hall regime. Even though Majorana mini-bands can no longer be distinguished in the bulk, Majorana edge channel modes are present when the superconducting state has an odd $\mathbb{Z}$ topological

index. Achieving superconductivity in the Landau level regime is becoming more commonplace [87, 88, 89], but it is still a challenge. There are theoretical predictions of superconductivity in two dimensions beyond the semicalssical H_{c2} [90, 91, 92, 69], with T_c increasing with magnetic field. Theoretically, such re-entrant superconducting phase is possible because of very high density of state in the isolated Landau level regime of the parent superconductor with effective attractive interactions. However, such phase is not observed experimentally, possibly due to Pauli breakdown and disorder. In our, experimental proposal, the Landau level gap of the normal part is large enough even at moderate magnetic field that the parent superconductor can exist in vortex lattice phase well below its H_{c2}. Although most easily probed by edge-sensitive transport experiments, the relationship between vortex lattices and topological classification has a bulk origin, related ultimately to the difference between the electron and Cooper-pair magnetic flux quanta.

The work in this chapter establishes important role the vortex lattice plays in topological classification of the topological superconductors. It also opens some possible future directions of research in this field. One important future direction is to study the effect of disordered vortex lattice, and possibility of using disorder to induce odd-$\mathbb{Z}$ topological index in the topological superconducting regime. Another important direction is to study the role of vortex lattice in determining 1D topological superconducting phases such as studied in chapter 3 for quantum anomalous Hall systems.

Chapter 5

Reentrant superconductivity in strong magnetic field

In this chapter[1] we study reentrant superconductivity in strong magnetic field for some simple multiple-band systems [93]. The particular focus is on systems with Dirac or quadratic band touching. We evaluate the sum of particle-particle ladder diagrams for electrons in Landau levels interacting with each other via $\delta(\boldsymbol{r})$ function attractive interaction. The attractive interaction effectively models a generic Cooper pairing of electrons. For example, for a BCS superconductor, it is simply related to the electron-phonon coupling. The divergence in the sum of ladder diagrams signals Cooper instability [94], hence can be identified as the transition between normal metal and the superconducting condensate. Overall, we obtain the magnetic field (B) versus temperature (T) phase diagram of transition between superconductor and normal metal, taking into account Landau quantization of the pairing electrons.

In the semiclassical limit, when the Landau level gaps are much smaller than the Fermi energy E_F, the results are in agreement with the semiclassical $B-T$ phase diagram, that can be obtained from the Ginzburg-Landau theory. Near the semiclassical upper critical magnetic field H_{c2} and beyond, the quantum oscillations start to appear in the phase diagram [95, 96]. The quantum oscillations are indication of Landau quantization becoming stronger and comparable to the Fermi energy scale. The most interesting phenomena occurs in the extreme quantum limit (*i.e.* $B \gg H_{c2}$), such that there are very few Landau levels in the Debye energy window E_D around the Fermi level. In this limit, the Cooper instability re-enters every time a Landau level gets close

[1]This chapter is based on unpublished research article: Gaurav Chaudhary, Michael R. Norman, Allan H. MacDonald *et.al.*(under preparation).

enough to the Fermi level. Moreover for the stronger magnetic fields (when lower Landau levels get close to the Fermi level), the reentrant superconducting dome is larger and has a higher critical temperature T_c. This happens because of the large density of state available at the Landau level for attractive pairing interaction. This would mean that in conventional clean materials superconductivity should persist up to fields much higher than the semiclassical H_{c2}. This remarkable phenomena is called reentrant superconductivity and has been theoretically studied in detail for conventional superconductors with $E_F \gg E_D$ [97, 91, 98, 69, 99, 100, 101, 102, 103, 104, 105]. However, this phenomena has not been experimentally observed.

The difficulty in experimentally achieving the reentrant phase can be attributed to the following reasons:

1. Usually the Fermi energy E_F is much higher in superconductors and sets the dominant energy scale. For the low lying Landau levels (where the reentrant phase is the strongest) to coincide with the Fermi level, in most superconducting materials may require magnetic field upto $100T$ or more, which are beyond practical accessibility.

2. In the conventional spin singlet superconductors, the Zeeman splitting of the Landau level at high field can result into scenario such that the two pairing electrons (which are of opposite spin) can never simultaneously come close to the Fermi level. This results in suppression of reentrant phase.

3. One can imagine applying additional in plane field to bring N^{th} spin up Landau level and $(N+1)^{th}$ spin down Landau level at the Fermi level simultaneously to enhance the reentrant phase. But such consideration requires even higher magnetic field, which was already beyond practical limit in most materials.

4. Finally, impurity scattering can destroy the reentrant phase.

The recent advances in the observation of superconductivity in MATBG and other moiré materials [36, 106, 107, 108] however can potentially provide an interesting system to revisit this problem. The moiré superconducting

systems are extremely low density superconductors[2]. Hence, Fermi energy is often not the highest relevant energy scale. The low lying Landau levels can be accessed at low magnetic field. This in itself takes care of the three of the four above mentioned issues with observing reentrant superconductivity. Hence, the possibility of reentrant superconductivity in these recent materials is at the heart of the theoretical calculations presented in this chapter.

The earlier theory work on reentrant superconductivity often assumed a single quadratic band to describe the system[3]. However, the lowest bands in the moiré systems are more complicated and in case of twisted bilayer graphene, the low energy sector is a two band system even when spin and valley degree are ignored. With this in mind, we extend the theory to cases of simple two-band systems with band touching of arbitrary order. As specific cases, numerical results are presented for Dirac model and quadraic band touching model. We show that for certain considerations for pairing interactions (such as $\delta(\boldsymbol{r})$-function interaction between electrons of opposite valley in context of twisted bilayer graphene), the sum of particle-particle ladder diagrams reduce to algebraic equations for a class of multiple-band systems. These algebraic equations can be solved easily to obtain the $B-T$ phase diagram which shows reentrant superconducting behavior in the quantum limit.

The chapter is organized as follows. Section 5.1 discusses the Landau level model and the pairing model considerations. Section 5.2 is the technical section that evaluates the ladder sum and can be skipped to avoid technical details. Section 5.3 contains the main scientific results of $B-T$ superconducting phase diagrams with focus on parameters relevant to the MATBG. Section 5.4 is the discussion section.

We mention that this chapter does not discuss topological superconductivity and Majorana modes. However, the ideas related to the superconductivity under broken $\mathcal{T}$-symmetry are in line with rest of the thesis. Moreover, the

[2]The MATBG has shown superconductivity at carrier densities as low as $n \sim 5 \times 10^{11}\text{cm}^{-2}$. In contrast bilayer of $NbSe_2$ shows superconductivity at carrier densities of more than 10^{15}cm^{-2}.

[3]The single quadratic band refers to bands with no spin orbit coupling, where each band is doubly degenerate due to spin.

technical aspects of superconducting pairing between Landau quantized electrons are similar to the one employed in chapter 4 are borrowed here.

5.1 Pairing in the Landau levels

Let us consider a simple Hamiltonian that can describe a two-band system with band touching feature:

$$H_+(\boldsymbol{\pi}) = \begin{pmatrix} 0 & \alpha(-\pi_x + i\pi_y)^\gamma \\ \alpha(-\pi_x - i\pi_y)^\gamma & 0 \end{pmatrix}, \tag{5.1}$$

where γ dictates the type of band touching [for example Dirac system is described by $\gamma = 1$ and quadratic band touching is described by $\gamma = 2$) and α dictates the parameters which shape the band (for example α is equal to the Fermi velocity v_F for Diarc system and $\alpha = 1/(2m^*)$ for quadratic band touching system, where m^* is the effective mass of the electron]. We choose to introduce the perpendicular magnetic field $\boldsymbol{B} = B\hat{z}$ using the Landau gauge vector potential $\boldsymbol{A} = (-By, 0)$. The electron kinetic momentum operators are then defined as $\boldsymbol{\pi} = \boldsymbol{p} - e\boldsymbol{A}$, where $p = -i\hbar\nabla$ is the canonical momentum operator.

One can define electron creation and annihilation operators

$$\hat{a} = \frac{(-\pi_x + i\pi_y)\ell}{\sqrt{2}\hbar}, \qquad \hat{a}^\dagger = \frac{(-\pi_x - i\pi_y)\ell}{\sqrt{2}\hbar}, \tag{5.2a}$$

such that the Hamiltonian in Eq. 5.1 can be expressed as

$$H_+(\hat{a}, \hat{a}^\dagger) = \begin{pmatrix} 0 & \alpha(\sqrt{2}\hbar\hat{a}/\ell)^\gamma \\ \alpha(\sqrt{2}\hbar\hat{a}^\dagger/\ell)^\gamma & 0 \end{pmatrix}. \tag{5.3}$$

For graphene (mono-layer or bilayer), if the above Hamiltonian describes the low energy physics at valley K, then the Hamiltonian acting in valley K' is simply

$$H_-(\hat{a}, \hat{a}^\dagger) = \begin{pmatrix} 0 & -\alpha(\sqrt{2}\hbar\hat{a}^\dagger/\ell)^\gamma \\ -\alpha(\sqrt{2}\hbar\hat{a}/\ell)^\gamma & 0 \end{pmatrix}. \tag{5.4}$$

The N^{th} Landau level eigenvalues are

$$\xi_{N,\gamma} = S_N \beta \left(\frac{\sqrt{2}\hbar}{\ell} \right)^{\gamma} \sqrt{(|N| + \gamma - 1)(|N| + \gamma - 2)...|N|}\,, \tag{5.5}$$

where S_N is the sign of N. The corresponding N^{th} Landau level wavefunctions at valley K (denoted by superscript '+') and valley K' (denoted by the superscript '$-$') are respectively,

$$\psi^{+}_{N,Y,\gamma}(\boldsymbol{r}) = \mathcal{N}_N \begin{pmatrix} S_N \phi_{|N|-1,Y}(\boldsymbol{r}), & \phi_{|N|+\gamma-1,Y}(\boldsymbol{r}) \end{pmatrix}^T, \tag{5.6a}$$

$$\psi^{-}_{N,Y,\gamma}(\boldsymbol{r}) = \mathcal{N}_N \begin{pmatrix} \phi_{|N|+\gamma-1,Y}(\boldsymbol{r}), & -S_N \phi_{|N|-1,Y}(\boldsymbol{r}) \end{pmatrix}^T. \tag{5.6b}$$

The terms appearing in the above Landau level wavefunctions are already defined in Chapter 4 and re-stated here for convenience:

$$\mathcal{N}_N = \begin{cases} \frac{1}{\sqrt{2}} & N \neq 0\,, \\ 1 & N = 0\,, \end{cases} \tag{5.7}$$

is the normalization factor, $Y = k_x \ell^2$ is a guiding center label, $\ell = \sqrt{\hbar/eB}$ is the magnetic length, $\phi_{n,k_x\ell^2}(\boldsymbol{r}) = (\mathrm{e}^{ik_x x}/\sqrt{L_x})\,\varphi_n(y/\ell - k_x \ell)$ is a n^{th} Landau level wave function of the non-relativistic 2DEG, and $\varphi_n(y)$ is a one dimensional harmonic oscillator eigenfunction. One can verify by substituting $\gamma = 1$, the above Eqs. 5.5, 5.6, and 5.7 reduce to the Dirac case considered in Chapter 4(See Eq. 4.3).

The instability towards the formation of a Cooper pair is associated with the divergence in the sum of particle-particle ladder diagrams illustrated in Fig. 5.1. In order to calculate the ladder sum of the diagrams, we need to construct two-body eigenstates, which can be represented either as the product of two single-particle eigenstates, or as the product of the COM and relative coordinate eigenstates. It is important to know the connection between these two representations, since the free-electron propagators are written in terms of the individual electron eigenstates, while the interaction line only depends on the relative coordinates. This connection has already been used in Chapter 4, which is restated in the rest of this section for convenience of the reader. In a

non-relativistic 2DEG of single band, the single-particle Hamiltonian can be conveniently written in either forms as:

$$H_{2DEG} = \hbar\omega_c(\hat{a}_1^\dagger\hat{a}_1 + \hat{a}_2^\dagger\hat{a}_2) = \hbar\omega_c(\hat{a}_R^\dagger\hat{a}_R + \hat{a}_r^\dagger\hat{a}_r)\,. \tag{5.8}$$

Here $\omega_c = eB/m^*$ is the cyclotron frequency, $\hat{a}_1$ and $\hat{a}_2$ are the annihilation operators for individual electrons and $\hat{a}_R = (\hat{a}_1 + \hat{a}_2)/\sqrt{2}$ and $\hat{a}_r = (\hat{a}_1 - \hat{a}_2)/\sqrt{2}$ are annihilation operators for the COM and relative coordinate eigenstates respectively. The two-particle eigenstates in the non-relativistic 2DEG can be written in the COM and relative coordinate eigenstates by using the transformation [70],

$$\phi_{N,X+Y/2}(\boldsymbol{r}_1)\phi_{M,X-Y/2}(\boldsymbol{r}_2) = \sum_{j=0}^{N+M} \mathcal{B}_j^{N,M}\phi_{j,X}^R(\boldsymbol{R})\phi_{N+M-j}^r(\boldsymbol{r}), \tag{5.9}$$

where

$$\mathcal{B}_j^{N,M} = \sum_{m=0}^{j}(-)^{M-m}\sqrt{\frac{{}^jC_m\ {}^MC_m\ {}^NC_{j-m}\ {}^{N+M-j}C_{M-m}}{2^{N+M}}}\,. \tag{5.10}$$

In the above equation, j and $N+M-j$ are the Landau level indices for COM and relative coordinates respectively. The expression for the COM and relative eigenstates $\phi_{n,X}^R$ and $\phi_{n,X}^r$ are identical to the individual electron eigenstate $\phi_{n,X}$, except that the effective magnetic lengths take values $\ell^R = \ell/\sqrt{2}$ and $\ell^r = \sqrt{2}\ell$, respectively. Moreover, the COM and relative coordinates are $\boldsymbol{R} = (\boldsymbol{r}_1 + \boldsymbol{r_2})/2$, and $\boldsymbol{r} = \boldsymbol{r}_1 - \boldsymbol{r}_2$. Finally, the coefficients $\mathcal{B}_j^{N,M}$ give the amplitude for having kinetic energy $\hbar\omega_c(j+1/2)$ in the COM motion when the individual particles have definite kinetic energies $\hbar\omega_c(N+1/2)$ and $\hbar\omega_c(M+1/2)$.

Before evaluating the ladder sum in next section, we mention that in Eqs. 5.8-5.10, we have used the non-relativistic 2DEG single band to introduce the transformation. However, our interest in this chapter is in Dirac and quadratic band touching systems. The generalization is presented next.

5.2 Evaluation of the ladder sum

As a physical basis of this calculation, one can imagine two electrons in same layer and opposite valley in the MATBG [109] (We mention that the

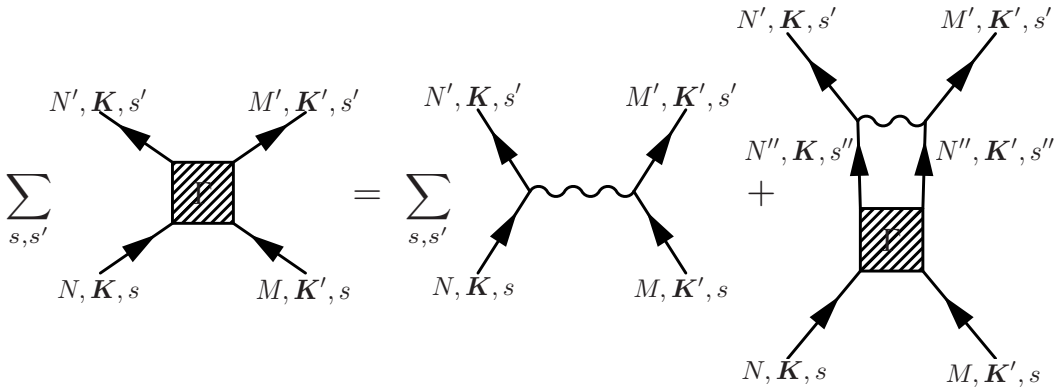

Figure 5.1: Diagrammatic illustration of the particle-particle ladder sum: The wavy line represents the irreducible interaction and the solid lines are the non-interacting electron Green's function in the presence of an external magnetic field. The indices s, s' indicate the orbital index, in which the interactions are assumed to be diagonal. For example in a simple bilayer graphene model, s, s' stand for the two layers.

calculations are valid to many other models, such as attractive interaction between electrons at same sub-lattice and opposite valleys of a monolayer graphene [110]) interacting via some attractive interaction. The spin is not considered here, but due to negligible spin-orbit coupling, it is straightforward to include spin. We evaluate the Ladder diagram in a representation of Landau gauge writing,

$$\begin{aligned}\Gamma_\gamma(\boldsymbol{r}_1\boldsymbol{r}_2;\boldsymbol{r}_1'\boldsymbol{r}_2';i\omega) = \sum_{Y_c,Y_c'}\sum_{N,M,Y_r}\sum_{N',M',Y_r'}&\Gamma_\gamma(N,M,Y_r;N',M',Y_r';i\omega)\\ &\times\psi^{+}_{N,Y_c+Y_r/2,\gamma}(\boldsymbol{r}_1)\psi^{-}_{M,Y_c-Y_r/2,\gamma}(\boldsymbol{r}_2)\\ &\times\psi^{+*}_{N',Y_c'+Y_r'/2,\gamma}(\boldsymbol{r}_1')\psi^{-*}_{M',Y_c'-Y_r'/2,\gamma}(\boldsymbol{r}_2')\,. \end{aligned}\tag{5.11}$$

Here the guiding center labels with subscript 'c' denote COM guiding center and with subscript 'r' denote relative guiding center. To simplify the notation we will make the usual assumption that the effective interaction is independent of frequency. Then the frequency sum over $i\omega''$ in the integral equation for Γ may be performed and we obtain equation for scattering am-

plitude:

$$\begin{aligned}\Gamma_\gamma(n,m,Y_r;n',m',Y_r') &= \langle n,Y_r/2;m,-Y_r/2|\hat{V}|n',Y_r'/2;m',-Y_r'/2\rangle_\gamma \\ &+ \sum_{n'',m'',Y_r''} \mathcal{K}^\gamma_{n'',m''}\langle n,Y_r/2;m,-Y_r/2|\hat{V}|n'',Y_r''/2;m'',-Y_r''/2\rangle_\gamma \\ &\times \Gamma_\gamma(n'',m'',Y_r'';n',m',Y_r') \\ &= \langle n,Y_r/2;m,-Y_r/2|\,\hat{V} \\ &\times [\mathbf{1} - \sum_{n'',m'',Y_r''} \mathcal{K}^\gamma_{n'',m''}|n'',Y_r''/2;m'',-Y_r''/2\rangle\langle n'',Y_r''/2;m'',-Y_r''/2|\,\hat{V}]^{-1} \\ &\times |n',Y_r'/2;m',-Y_r'/2\rangle\,. \end{aligned} \tag{5.12}$$

Here $\hat{V} = -V_0\delta(\boldsymbol{r})\sigma_0$. Above, we have changed the Landau level indices to lower case. The quantity $\mathcal{K}^\gamma_{n,m}$ above results from the sum over intermediate electron pair states. For a two-dimensional system

$$\mathcal{K}^\gamma_{n,m}(i\eta)_{\eta\to 0} = \frac{\tanh[\beta(\xi_{n,\gamma}-E_F)/2] + \tanh[\beta(\xi_{m,\gamma}-E_F)/2]}{2(\hbar i\eta - \xi_{n,\gamma} - \xi_{m,\gamma} + 2E_F)}\,, \tag{5.13}$$

where $\beta = 1/(k_BT)$ and k_B is the Boltzmann constant. Notice, we have kept the index γ for the sake of generality to different band models in our case. The first term on the right-hand side of the Eq. 5.12 is the two-particle matrix element of the effective electron-electron interaction. For a $\delta(\boldsymbol{r})$-function attractive interaction, it can be calculated to give the relation below (See the App. F for detail):

$$\begin{aligned}\langle n,Y_r/2;m,-Y_r/2|\,V\,|n',Y_r'/2;m',-Y_r'/2\rangle &= -\frac{V_0}{L_x}\mathcal{N}_n\mathcal{N}_m\mathcal{N}_{n'}\mathcal{N}_{m'} \\ &\times \sum_j \phi^r_{|n|+|m|+\gamma-2-j}(-Y_r)\phi^r_{|n'|+|m'|+\gamma-2-j}(-Y_r') \\ &\times [S_nS_{n'}\mathcal{B}_j^{|n|-1,|m|+\gamma-1}\mathcal{B}_j^{|n'|-1,|m'|+\gamma-1} \\ &+ S_mS_{m'}\mathcal{B}_j^{|n|+\gamma-1,|m|-1}\mathcal{B}_j^{|n'|+\gamma-1,|m'|-1}]\,. \end{aligned} \tag{5.14}$$

Finally, using the above expression for the interaction matrix element, the kernel Γ_γ in Eq. 5.12 can be evaluated by summing over interactions of all order. Importantly, the ladder sum simplifies to the sum of different COM

channels j, (See the App. F for the details on evaluation of the following expression):

$$\Gamma_\gamma(n,m,Y_r;n',m',Y_r') = -\frac{V_0}{L_x}\mathcal{N}_n\mathcal{N}_m\mathcal{N}_{n'}\mathcal{N}_{m'}\sum_j \mathcal{A}_{j,\gamma}(n,m;n',m') \times \phi^r_{|n|+|m|+\gamma-2-j}(-Y_r)\phi^r_{|n'|+|m'|+\gamma-2-j}(-Y_r')\,, \quad (5.15)$$

where,

$$\mathcal{A}_{j,\gamma}(n,m;n',m') = \frac{1-D_{j,\gamma}}{(1-D_{j,\gamma})^2-Q_{j,\gamma}^2}\Big(S_nS_{n'}\mathcal{B}_j^{|n|-1,|m|+\gamma-1}\mathcal{B}_j^{|n'|-1,|m'|+\gamma-1} + S_mS_{m'}\mathcal{B}^{|n|+\gamma-1,|m|-1}\mathcal{B}_j^{|n'|+\gamma-1,|m'|-1}\Big) + \frac{Q_{j,\gamma}}{(1-D_{j,\gamma})^2-Q_{j,\gamma}^2}\Big(S_mS_{n'}\mathcal{B}_j^{|n|+\gamma-1,|m|-1}\mathcal{B}_j^{|n'|-1,|m'|+\gamma-1} + S_nS_{m'}\mathcal{B}^{|n|-1,|m|+\gamma-1}\mathcal{B}_j^{|n'|+\gamma-1,|m'|-1}\Big)\,, \quad (5.16)$$

and

$$D_{j,\gamma} = -\frac{V_0}{\pi\ell^2}\sum_{n,m}\mathcal{K}^\gamma_{n,m}\left(S_n\mathcal{N}_n\mathcal{N}_m\mathcal{B}_j^{|n|-1,|m|+\gamma-1}\right)^2, \quad (5.17a)$$

$$O_{j,\gamma} = -\frac{V_0}{\pi\ell^2}\sum_{n,m}\mathcal{K}^\gamma_{n,m}S_nS_m\left(\mathcal{N}_n\mathcal{N}_m\right)^2\mathcal{B}_j^{|n|-1,|m|+\gamma-1}\mathcal{B}_j^{|n|+\gamma-1,|m|-1}\,. \quad (5.17b)$$

The different COM kinetic energy channels separate because the partitioning of the quantized energy into COM kinetic energy and relative-motion kinetic energy does not change between scattering events. This property can be understood by noting that the COM kinetic energy is constant for the single band non-relativistic electrons executing cyclotron orbits of arbitrary radius when the electron positions coincide at some point in their orbits. Mathematically, it can been seen through the simple translation of H_{2DEG} in Eq. 5.8. In a two-band systems of Eq. 5.1, the transformation has different property and the ladder sum in its general form does not separate into sum of different COM channels. The simplification we used in our interaction model, which considers only inter-valley and intra-layer interaction is responsible for

the simple separation of the ladder sum into COM channels. Importantly the above mentioned approximation is likely to be the correct approximation for bilayer graphene systems at small twist angles.

5.3 Magnetic field vs Temperature phase diagram

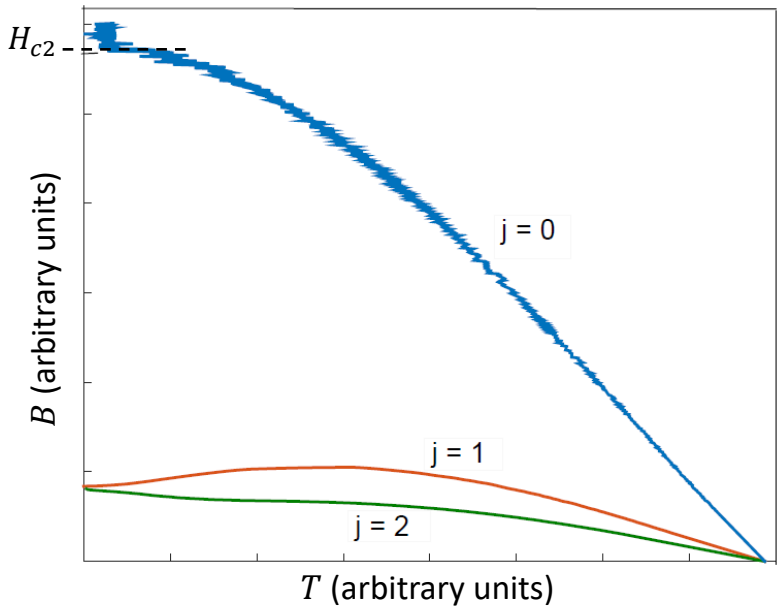

Figure 5.2: A representative normal metal-superconductor phase diagram below semiclassical H_{c2}: The Cooper instability is calculated using particle-particle ladder diagram sum which takes into account Landau quantization of the electrons. Apart from some quantum-oscillating features, the phase diagram agrees with semiclassical Ginzburg-Landau theory below H_{c2}.

The divergence of $\mathcal{A}_{j,\gamma}$ signals the occurrence of an instability of the system toward the formation of Cooper pairs in COM channel j. Hence as a function of the magnetic field and temperature the trajectory of its divergence provides the phase diagram between normal metal phase and superconducting condensate. From Eq. 5.16, it is clear that the divergence occurs when

$$D_{j,\gamma} \pm Q_{j,\gamma} = 1\,, \tag{5.18}$$

which translates to finding the solution to

$$\frac{g}{\pi\ell^2\rho(E_F)}\sum_{n,m}\mathcal{K}^{\gamma}_{n,m}S_n\left(\mathcal{N}_n\mathcal{N}_m\right)^2\mathcal{B}_j^{|n|-1,|m|+\gamma-1} \times\left[S_n\mathcal{B}_j^{|n|-1,|m|+\gamma-1}\pm S_m\mathcal{B}_j^{|n|+\gamma-1,|m|-1}\right]=-1\,, \quad (5.19)$$

where $\rho(E_F)$ is the normal state density of states at the Fermi energy. Next, using the above expression in Eq. 5.19, we discuss the semiclassical and extreme quantum limit of the Copper instability.

Majority of the superconductors have very high Fermi energy compared to the Debye energy. In the conventional superconductor with $E_F \gg E_D$ and magnetic field below semiclassical H_{c2}, one can assume the single band limit of the pairing and Landau level indices n, m of the pairing electrons to be very high, such that $n+m=T$ and $n-m=t$. In the limit $T \gg |t|$, the transformation coefficients can be simplified as [111]

$$\begin{aligned}\mathcal{B}_j^{n,m} &= \mathcal{B}_j^{(T+t)/2,(T-t)/2} \\ &\sim \left(\frac{2}{T\pi}\right)^{1/4}\left(\frac{1}{2^j j!}\right)^{1/2} H_j(t/\sqrt{2T})\,\mathrm{e}^{-t^2/(4T)}\,,\end{aligned} \quad (5.20)$$

where H_j is the j^{th} Hermite polynomial. The resultant relation that provides the Cooper instability for small γ simplifies to (starting from Eq. 5.19):

$$\frac{g}{2\pi\ell^2\rho(\mu)}\sum_{T,t}\mathcal{K}^{\gamma}_{(T+t)/2,(T-t)/2}\left(\frac{2}{t\pi}\right)^{1/2}\left(\frac{1}{2^j j!}\right)H_j^2(t/(\sqrt{2T}))\,\mathrm{e}^{-t^2/(2T)}=-1\,. \quad (5.21)$$

For $j=0$ superconducting channel, the above relation gives the well known semiclassical expresstion for the critical temperature T_c. The Fig. 5.2 shows a representative case of the phase diagram calculated using the ladder sum derived above for the three lowest COM momentum pairing channels. For a system with $E_F \gg E_D$ and magnetic field not exceeding the semiclassical H_{c2}, the phase diagram here agrees with the conventionally shown $B-T$ phase diagrams, apart from some small quantum oscillation features, which show that the effect of Landau quantization start to appear close to H_{c2}. In the low field region the Ginzburg-Landau theory predicts $Hc \propto H_{c2}/(2j+1)$ for

different COM channels j, which is also in agreement here. The fact that $j = 0$ channel has highest T_c shows absence of the Fulde–Ferrell–Larkin–Ovchinnikov (FFLO) phase [112, 113] for conventional pairing in weak field limit. The qualitative shape of the curve is also largely independent of the type of band structure, however the critical temperature and the field dependence on Femri level depends on band detail, mainly because of the dependence of density of states dependence on the band model.

In strong magnetic field beyond the semiclassical case, we can assume the single Landau level limit, where the landau level closest to the Fermi level dominates the Cooper instability. Under this limit, assuming the dominant Landau level n is arbitrarily close to the Fermi level, the instability is obtained as finding solution to the relation:

$$T_c \sim \frac{g\mathcal{N}_n^4 eB[\mathcal{B}_j^{|n|-1,|n|+\gamma-1}(\mathcal{B}_j^{|n|-1,|n|+\gamma-1} \pm \mathcal{B}_j^{|n|+\gamma-1,|n|-1})]}{8k_B\pi\hbar\rho(E_F)}\,. \tag{5.22}$$

One can see that the T_c increases linearly with magnetic field for the reentrant phase. Hence lower Landau levels potentially have dominant reentrant phase. Another non-trivial feature is the appearance of two Cooper instability channels with same T_c in the reentrant phase, which is unlike the conventional phase below the semiclassical H_{c2}. More specifically, for the reentrant phase of n^{th} Landau level, the Cooper instability channel with $j = 0$ and $j = 2|n| - \gamma$ have equal T_c. The Copper channel with $j = 2|n| - \gamma$ has COM in higher Landau level. Hence it is potentially an FFLO phase.

Next, we discuss the phase diagram for three different band models, *i.e.*, single quadratic band model, a Dirac band model ($\gamma = 1$), and a quadratic band touching model ($\gamma = 2$). The parameters of the model are kept such that they resemble the observed superconductivity in the MATBG [36, 106], and the focus is to show reentrance of superconductivity for magnetic field beyond semiclassical H_{c2}.

5.3.1 Single band 2DEG

The simplest case of quadratically dispersing single band in absence of spin-orbit coupling is considered in the earlier works [69, 103]. Notice that

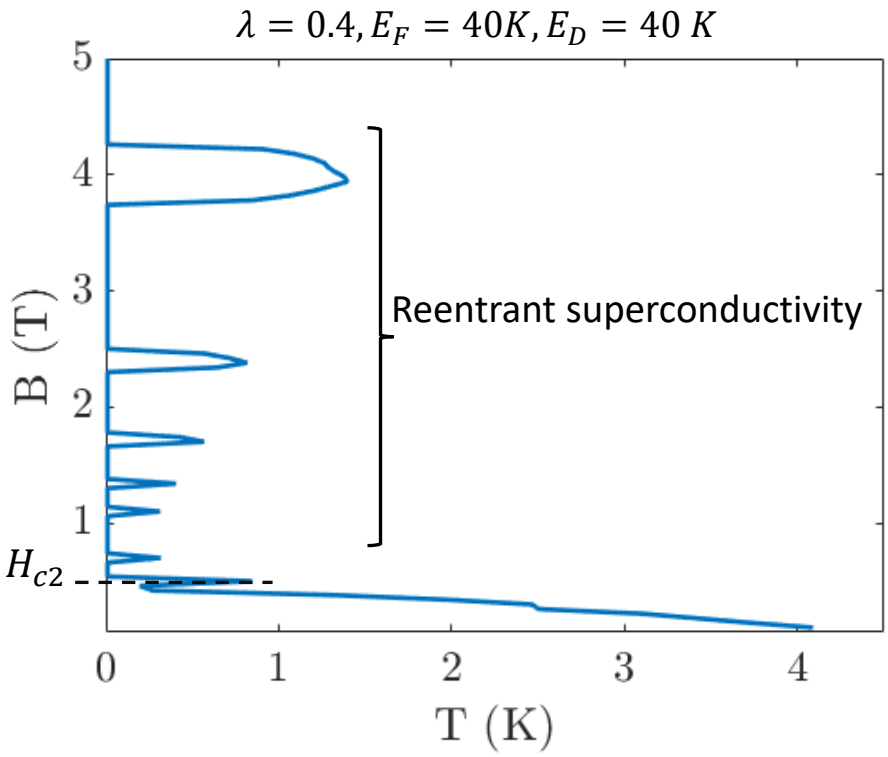

Figure 5.3: The $B-T$ phase diagram for a single quadratically dispersing band model: The parameters are chosen to match the MATBG. The system shows the domes of reentrant superconductivity with each Landau level crossing the Fermi level.

our evaluation of ladder sum was for the two-band system, hence not directly applicable to this case. However, the single band system is relatively simple and the Copper instability equation looks similar to the Eq. 5.19, with some minor changes. The reader may refer to the Ref. [69] or the App. F for the derivation of the ladder diagram sum for this case. Here we merely state the relation:

$$\frac{g}{4\pi\ell^2\rho(E_F)}\sum_{n,m}\mathcal{K}^{\gamma}_{n,m}\,(\mathcal{B}^{n,m}_{j})^2 = 1\,, \tag{5.23}$$

and the reentrant phase in single Landau level limit has critical temperature relation:

$$T_c \sim \frac{ge\hbar B(\mathcal{B}_j^{N,N})^2}{16m^* k_B}\,. \tag{5.24}$$

Here, we have used the constant density of states

$$\rho(E) = \frac{m^*}{\pi\hbar^2}\,, \tag{5.25}$$

for the quadratic band in 2D. To match the observed superconductivity in the MATBG [106] below H_{c2}, the electron effective mass $m^* = 0.2m_e$, Fermi level $E_F = 40K$ and Debye energy $E_D = 40K$ is used. The numerically obtained phase diagram with these parameters is shown in Fig. 5.3, which shows reentrant behavior.

5.3.2 Dirac band touching

For the Dirac band touching model, the Fermi velocity is renormalized such that the band width of the Dirac spectrum in the moiré mini-Brillouine zone matches the band width of the lowest bands of the MATBG. The actual value used is $v_F^* = 0.027v_F$, where v_F is the monolayer graphene's Fermi velocity. The numerically obtained phase diagram is shown in Fig. 5.4, which shows the reentrant phase.

5.3.3 Quadratic band touching

The band details of the quadratic band touching case are very similar to the single non-relativistic 2DEG band. However, the presence of two bands allows consideration of the case with $E_D > E_F$, which is potentially the case in the experiment. Moreover, the quadratic band touching case is likely to be the closest yet simple enough band model for the magic angle case. The numerically obtained $B - T$ phase diagram is shown in Fig. 5.5, obtained at same parameters as the single 2DEG band but with twice the Debye energy. The phase diagram shows reentrant superconductivity.

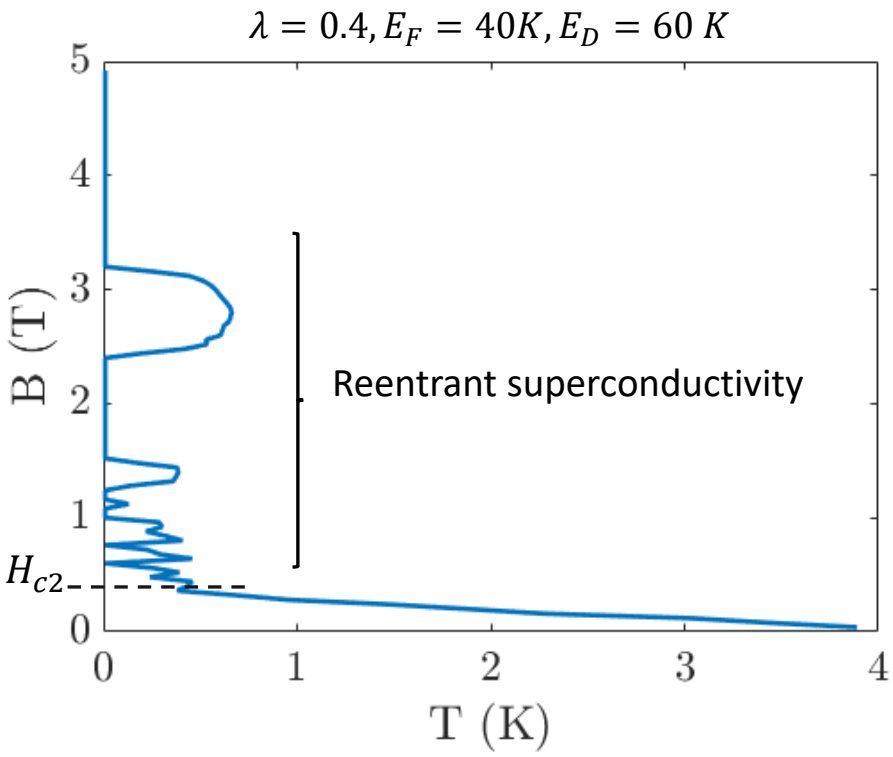

Figure 5.4: The $B-T$ phase diagram for a Dirac band touching model: Fermi velocity $v_F^* = 0.027 v_F$, where v_F is the monolayer graphene Dirac velocity to match the MATBG. The system shows the domes of reentrant superconductivity with each Landau level crossing the Fermi level.

5.4 Discussion and conclusion

In conclusion, we have derived exact particle-particle ladder diagram sum for electrons occupying Landau levels of a class of two band models and interacting with each other via $\delta(\boldsymbol{r})$ function attractive interactions. Specifically the band models considered are models with any arbitrary order n band touching. A simplification employed is that interaction is diagonal in the orbital basis. This model is likely to be relevant in the bilayer graphene systems, if the superconductivity is due to conventional electron-phonon coupling.

The divergence in the ladder sum of attractive interaction model signals

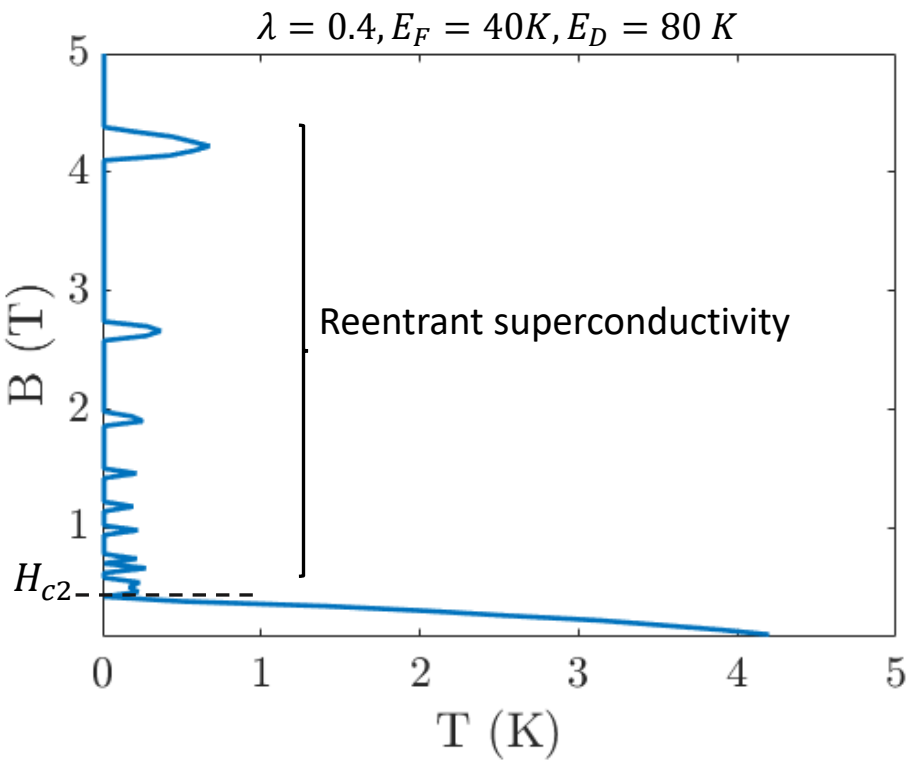

Figure 5.5: The $B - T$ phase diagram for a quadratic band touching model: The parameters are chosen to match the MATBG. The system shows the domes of reentrant superconductivity with each Landau level crossing the Fermi level.

Cooper instability at mean field level. The solutions of the ladder sum show presence of reentrant superconducting phase well beyond semiclassical H_{c2}. This reentrant phase has not been experimentally observed. However, it is unclear if there is a fundamental reason for it to not exist or the limitations are related to the achieving required experimental conditions. At purely theoretical level, our calculations are related to finding mean-field solutions to electrons interacting via attractive interactions in Landau level. Where our calculations reveal that at purely mean field level, just like in the semiclassical limit of low magnetic field, the Landau quantized electrons can also show Copper instability. However some of the qualitative features of this emergent

superconducting phase can be different from the conventional situation, such as possible emergence of FFLO phase. At a more physical level, there may be some additional effect coming into play when one reaches this regime, which suppresses the reentrant phase due to some reasons not considered in our calculations. Optimistically, it is possible that the reason this phase has not been observed is purely due to inability to achieve the very high magnetic field required to reach this regime in conventional high density BCS superconductors. If that is the only limitation, we show that experimental progress can be achieved in recently discovered superconductivity in moiré materials, where the reentrant phase is achieved at relatively moderate magnetic field (below $10T$ for example in our calculations). This can potentially uncover new class of exotic superconducting phases.

Finally, there has been recent efforts in understanding the single particle flat bands of the MATBG in close analogy with the Landau levels [114, 115, 116]. Depending how close this analogy is, it is worthwhile to understand the nature of the superconducting phases emerging from electrons in Landau level. Our calculations also make progress in that direction.

Chapter 6

Experimental progress, interpretations, and discussion

In this thesis, we have focused on superconductivity when electrons in their non-interacting limit are in some Chern insulator phase, namely, either the quantum Hall or the quantum anomalous Hall phase. The main focus is on proximity coupled systems, where a trivial insulator induces superconductivity in a non-interacting system exhibiting quantized Hall conductance.

The quantum Hall based systems require strong external magnetic field, where we have shown the importance of the vortex lattice physics. Although the quantum Hall based systems can potentially show new exotic topological superconducting phases [117, 67], the magnetic field requirement makes it difficult to achieve. Significant progress has been achieved in proximity inducing superconductivity in quantum Hall edge states [118, 88, 89, 119]. The progress in the field of thin film superconductors with very high upper critical magnetic field is a promising development for the future experiments in this direction [120].

The quantum anomalous Hall effect does not require strong external magnetic field and over the last few years there has been significant progress in high quality magnetic TI samples with exceptional quantization of the Hall conductance plateau [51]. The progress made in proximity inducing superconductivity in the quantum anomalous Hall system has led to some interesting experimental advances recently [26, 37], which is discussed in this chapter.

6.1 A quantum anomalous Hall/superconductor based transport device

A proposal to detect chiral Majorana edge modes in a quantum anomalous Hall/superconductor based device via a transport experiment was first put forward by Chung *et. al.* [73]. In this section, we review their theoretical proposal.

Consider a two terminal transport experiment in a device shown schematically in Fig. 6.1(a). To understand the edge transport, the device can be divided into three 2D bulk regions. The central region has an s-wave superconductor covering the quantum anomalous Hall system, which induces superconducting gap via proximity effect. The topological characterization of this region is already done in chapter 3. As shown in Sec. 3.2.1, the central region can exhibit $N = 0, 1$, and 2 topological superconducting phase via suitable tuning of the parameters. The two regions on the either side can exhibit quantum anomalous Hall effect and can only show $N = 0, 2$ phases, *i.e.* a trivial insulator and a quantum anomalous Hall insulator respectively. Hence depending on the scenario, in the Majorana representation (BdG doubled basis), the edge states can have the configurations as shown in Fig. 6.1 (b)-(d).

Assuming the edge state configuration shown in the Fig. 6.1 (b)-(d) is achievable in the experiment, then because at the edge any electronic transport is via coherent transport of the Majorana, we can write,

$$\begin{pmatrix} \hat{b}_{1e} + \hat{b}^\dagger_{1e} \\ \hat{b}_{2e} + \hat{b}^\dagger_{2e} \end{pmatrix} = \begin{pmatrix} r & 0 \\ 0 & r' \end{pmatrix} \begin{pmatrix} \hat{a}_{1e} + \hat{a}^\dagger_{1e} \\ \hat{a}_{2e} + \hat{a}^\dagger_{2e} \end{pmatrix} , \tag{6.1a}$$

$$\begin{pmatrix} \hat{b}_{1e} - \hat{b}^\dagger_{1e} \\ \hat{b}_{2e} - \hat{b}^\dagger_{2e} \end{pmatrix} = \begin{pmatrix} 0 & t \\ t' & 0 \end{pmatrix} \begin{pmatrix} \hat{a}_{1e} - \hat{a}^\dagger_{1e} \\ \hat{a}_{2e} - \hat{a}^\dagger_{2e} \end{pmatrix} . \tag{6.1b}$$

Here the operator $\hat{a}_{je}$ annihilates an electron outgoing from the lead j and the operator $\hat{b}_{je}$ annihilates an incoming electron in lead j. And the combination $\hat{a}_{je} \pm \hat{a}^\dagger_{je}$ or $\hat{b}_{je} \pm \hat{b}^\dagger_{je}$, represent a chiral Majorana edge state upto a normalization constant. The matrix elements r and r' are the reflection amplitude at the central superconductor covered region between lead 1 and 2. And the matrix elements t and t' are the transmission amplitude at the

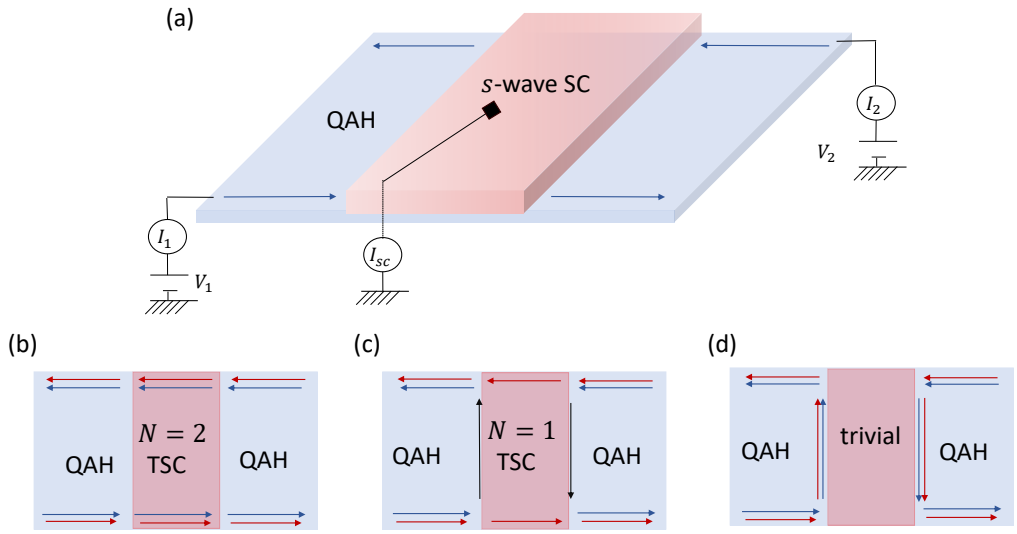

Figure 6.1: Transport experiment setup: (a) A two terminal setup with the superconductor covering the central portion of a quantum anomalous Hall (QAH) system: (b) When the central region behaves as $N = 2$ topological superconductor, the two Majorana at the edge are transmitted through the central region. (c) When the central region behaves as $N = 1$ topological superconductor, one of the Majorana is transmitted and one is reflected from the central region. (d) When the central region behaves as a trivial superconductor, both the Majorana are reflected back.

central region. Because in this picture a quantum anomalous Hall edge state is interpreted as two Majorana edge state and all the edge states transport is coherent in Majorana, if one assumes the situation shown in Fig. 6.1(c), where the central region being in the $N = 1$ phase, one of the Majorana is transmitted and the other reflected back. The reflection and the transmission matrix elements must be unit in magnitude:

$$|r| = |r'| = |t| = |t'| = 1\,. \tag{6.2}$$

The scattering matrix then can be formulated using Eq. 6.1:

$$\begin{pmatrix} \hat{b}_{1e} \\ \hat{b}^{\dagger}_{1e} \\ \hat{b}_{2e} \\ \hat{b}^{\dagger}_{2e} \end{pmatrix} = \frac{1}{2} \begin{pmatrix} r & r & t & -t \\ r & r & -t & t \\ t' & -t' & -r' & r' \\ -t' & t' & r' & r' \end{pmatrix} \begin{pmatrix} \hat{a}_{1e} \\ \hat{a}^{\dagger}_{1e} \\ \hat{a}_{2e} \\ \hat{a}^{\dagger}_{2e} \end{pmatrix} . \tag{6.3}$$

Following the superconducting generalization of the Landauer-Buttiker formalism [121], we arrive at the following quantum transport equations in the current leads:

$$I_1 = \frac{e^2}{h}[(1 - g_{11}(V_1 - V_{sc}) - g_{12}(V_2 - V_{sc})] \,, \tag{6.4a}$$

$$I_2 = \frac{e^2}{h}[-g_{21}(V_1 - V_{sc}) + (1 - g_{12})(V_2 - V_{sc})] \,, \tag{6.4b}$$

where,

$$g_{ii} = \mathcal{R}_N - \mathcal{R}_A \,, \tag{6.5a}$$

$$g_{ij}|_{i \neq j} = \mathcal{T}_N - \mathcal{T}_A \,, \tag{6.5b}$$

and $\mathcal{R}_N$, $\mathcal{R}_A$ are the normal and Andreev reflection probabilities respectively, and $\mathcal{T}_N$, $\mathcal{T}_A$ are the normal and Andreev transmission probabilities respectively. Following Eq. 6.2 and 6.3,

$$\mathcal{R}_N = \mathcal{R}_T = \mathcal{T}_N = \mathcal{T}_A = \frac{1}{4} \,. \tag{6.6}$$

Substituting Eq. 6.5 and 6.6 in Eq. 6.4 and taking the limit $V_1 = -V_2 = V$, the two terminal conductance is obtained:

$$G_{12} = \frac{I_1}{V_1 - V_2} = \frac{e^2}{2h} \,. \tag{6.7}$$

Hence for the transport device shown in Fig. 6.1, when the central region is $N = 1$ topological superconductor and the region on the two sides are in quantum anomalous Hall phase [see the configuration in Fig. 6.1(b)], the two terminal conductance must be half-quantized in the units of e^2/h. One can similarly show that when the central region is $N = 2$ topological superconductor [See Fig. 6.1(b)] or $N = 0$ topological superconductor [See Fig. 6.1(d)], the two terminal conductance is unit quantized or zero respectively.

6.2 Experimental observations

The above mentioned transport device has been achieved in two recent experiments [26, 37]. The experimental device is based on a magnetically doped thin film of TI covered in center by a thin film of an s-wave superconductor.

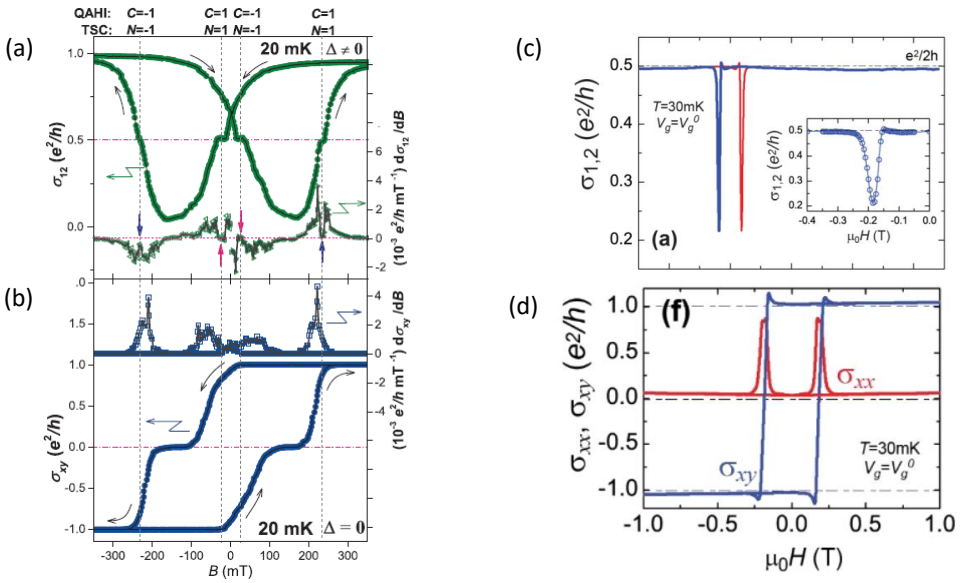

Figure 6.2: The two different transport studies based on the device shown in Fig. 6.1: The panel on the left (a),(b) shows data from He *et. al.* [26] [Science **357**, 294–299 (2017)]. The panel on the right (c), (d) shows data from similar device by Kayyalha *et. al.* [37][arXiv:1904.06463].

As discussed in chapter 3, the tuning of the quantum anomalous Hall effect in a magnetic TI is done via tuning of the mass term of the two layer model Hamiltonian. Experimentally, the tuning of the mass term is equivalent to the tuning of the magnetic order of the magnetic dopants in the TI, which is done via application of a small external perpendicular magnetic field. The $N = 1$ topological superconducting phase is expected to appear as an intermediate phase when the magnetic TI undergoes the quantum anomalous Hall transitions.

Figure 6.2 shows data from the two recent experiment on the above mentioned device [26, 37]. Both experiments show half quantized two terminal

conductance [See Fig. 6.2(a) and Fig. 6.2(c)]. However, their interpretations are different. The panel on the left shows, along with small regions of half quantized plateau of the two terminal conductance as expected near quantum anomalous Hall transition; a quantized two terminal conductance when the magnetic TI is deep in its quantum anomalous Hall phase. The panel on the right on the other hand shows only half quantized two terminal conductance for the entire range of the magnetic field.

If the picture of coherent transport of the Majorana at the edge is correct as shown in Fig. 6.1(b)-(d), when the normal part is deep in its quantum anomalous Hall phase, the central region must eventually reach $N = 2$ topological superconducting phase shown in Fig. 6.1 (b). In this scenario, both the Majorana modes are coherently transmitted through the central region. This scenario must give a quantized two terminal conductance as seen in the left panel of the Fig. 6.2. Thus, along with the observation of the half quantized two terminal conductance, the observation of the quantized two terminal conductance is necessary for the Majorana transport (next section shows that it is not sufficient). The experiment on the right panel [37] of Fig. 6.2 definitely does not have Majorana edge state and the experiment.

6.2.1 Disorder induced transport

Here we discuss an alternate scenario proposed independently by Huang *et. al.* [65] and Ji *et. al.* [64] that can also provide the transport signature seen in the left panel of the Fig. 6.2 without the coherent transport of the Majorana at the edge.

Using the Eq. 6.4 to describe the quantum transport and based on the device symmetry, substituting $g_{11} = g_{22} = g$ and $g_{12} = g_{21} = \tilde{g}$, we write down the two terminal conductance as

$$G_{12} = \frac{e^2}{2h}\left[\frac{\tilde{g}^2 - (1-g)^2}{g + \tilde{g} - 1}\right]. \tag{6.8}$$

The conditions on the above equation to yield half quantized two terminal conductance is simply $\tilde{g} = g$. The coherent Majorana transport picture satisfies only one point of this general condition. Now, to understand another alternative physical scenario that satisfies the above condition, first imagine

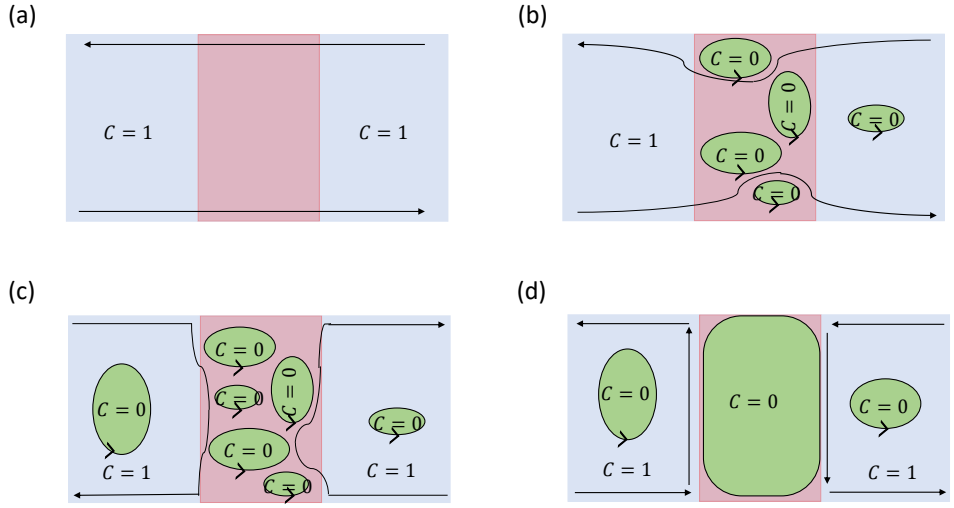

Figure 6.3: The percolation picture of the quantum anomalous Hall/superconductor device: (a) When the normal part is deep in quantum anomalous Hall phase, the electronic edge state is coherently transmitted through the central region and shows quantized two terminal conductance. (b) and (c) When the normal part is close to its quantum anomalous Hall-normal insulator transition, the critical region is described through percolation of domains of different topological character. For the electronic edge state to transport near the critical point, it has to go around the highly disordered domains of different topological phase and in the process it loses coherence and becomes an equal incoherent mixture of electron and hole. This scenario can also give half quantized two terminal conductance. (d) When the normal part becomes trivial, the electronic edge state is reflected back from the central region and the two terminal conductance vanishes.

the central region is not superconducting, instead is a bulk metal. This is possible if the superconductor can not proximity induce the pairing gap effectively. In that case the superconducting region in the middle simply behaves as a reservoir for the electronic edge state and the two ends of of the edge state at the central region experience the same chemical potential. All the transport coefficients are simply $g = \tilde{g} = 0$ in this case, and one again gets the half quantized two terminal conductance. This is likely to be the case with the experiment in the right panel. However, this is not the case in the experiment on the left panel, because it shows a quantized conductance plateau at larger magnetic fields, along with the half-quantized plateau. Next, we show that effect of disorder can lead to the physical scenario similar to the above mentioned metal reservoir scenario exactly in the experimental region where half-quantized conductance plateau is observed.

The magnetic TI are inherently disordered systems, in particular when they are close to the quantum anomalous Hall transition. This is because when magnetic order of the ferromagnetic dopants is controlled via external magnetic field, the transition happens through domains of magnetically ordered and disordered dopants. One can understand the system near transition using percolation picture qualitatively presented in the Fig. 6.3. Near the critical point presented in the Fig. 6.3(b) and (c), the percolation domains are highly disordered and spread throughout the bulk. For the electronic edge state to transport through the central region, it has to find a path around these domains. In doing so, the initially 1D edge state has to effectively travel a long trajectory going through the bulk, where it has finite tunneling amplitude into the regions of $N = 0$ domains. During this process with the domains of different topological character, the edge state loses its coherence and becomes an equal mixture of electron and hole. This phenomena is qualitatively similar to the central region behaving like a normal metal even if it induces proximity gap. Hence near this critical region, the system can exhibit half-quantized two terminal conductance without the coherent transport of the Majorana. Importantly, when the magnetic TI is fully magnetized and is deep in its quantum anomalous Hall phase, it can coherently transport the electronic edge state and show the quantized two terminal conductance as seen in the left panel of Fig. 6.2. The Ref. [65, 64] analyze this scenario quantitatively

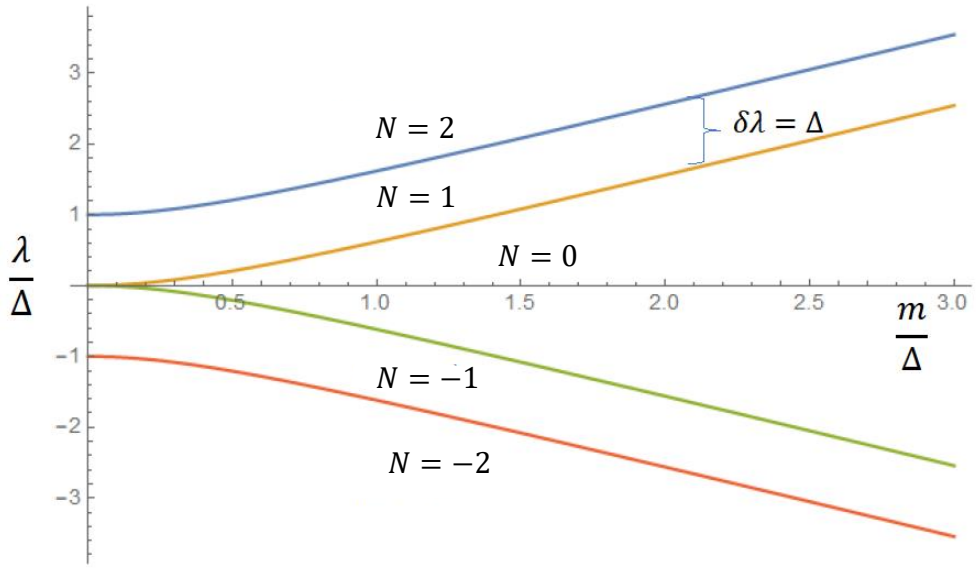

Figure 6.4: Topological phase diagram of the bilayer magnetic TI proximity coupled to s-wave superconductor as function of the interlayer coupling of the two layer of the TI. In the simple model, the width of the $N = 1$ phase remains unchanged, whereas the width of the $N = 0$ phase changes.

and show that, it can reproduce the experimental data of He *et. al.* [26] shown in left panel of Fig. 6.2.

6.3 Discussion

In conclusion, even after recent experimental progress in achieving high quality quantum anomalous Hall devices and proximity coupling them to the superconductor, the experimental signatures of topological superconductivity and chiral Majorana edge modes in these systems are under heavy debate [26, 63, 65, 64, 66, 37].

The debate can be divided at two levels or arguments:

1. First, is it possible to proximity induce coherent superconductivity at mesoscale size devices, when the superconducting coherence lengths are

much smaller? The argument is based on early theoretical work [122], which studies a quantum Hall edge state encountering a superconductor along one of the edge. In a semi-classical skipping orbit picture of the quantum Hall edge state (one can expect the basic idea still applies to quantum anomalous Hall edge state even when the skipping orbit picture is not valid.), every time an electron bounces off the superconducting wall, it comes back as a hole due to Andreev reflection. Hence the semicalssical orbits alternate between electron and hole character. If the superconductor is along the entire edge of the quantum Hall device, because of the repeated Andreev reflection with the superconductor, the edge state acquires a steady state, which is an incoherent equal mixture of electrons and holes. In this picture, the transport device discussed here will always show half quantized conductance per quantum Hall edge irrespective of how deep in quantum (anomalous) Hall phase is the non-proximitized part. This picture is argued by Kayyalha *et. al.* [37] to explain their observation of persistent half quantized plateau shown in the right panel of Fig. 6.2. However, the theory [122] assumes the superconducting region along the quantum Hall edge to be trivial. Hence on the other side of the quantum Hall edge (in the superconductor), there is no possibility of coherent transport of the edge state. This leads to the incoherent mixture of the electron and hole resulting from multiple Andreev reflection. If the superconducting region is topological (which is at least possible from the simple models considered here), the superconducting side can allow the coherent transport. Thus simply based on this argument, if the central region of the device can have clear $N = 1$ topological superconducting phase, the transport experiment can work in principle.

2. Second, is it possible to distinguish between disorder induced transport data and data due to coherent transport of the Majorana? The progress in this direction can be made by observing the trends in the size of different plateaus associated with different topological region as the details of the sample are changes. Figure 6.4 shows the topological phase diagram as a function of the interlayer hybridization; obtained from the simple coupled Dirac model for the magnetic TI and the uniform proximity model for the induced superconductivity as studied in chapter 3.

The interlayer hybridization parameter can be tuned by performing experiments on TI samples of different thickness. Interestingly, the width of the $N = 1$ phase is independent of the TI thickness, while width of the $N = 0$ phase changes as shown in the Fig. 6.4. In the language of the of the transport experiment, this means that half-quantized plateau should remain robust with the same plateau width while the width of the zero conductance plateau changes for the experiments on the TI films of different thickness. Of course, all this can change as the microscopic details will change with different samples and the phase diagram may not closely resemble the one obtained in the toy model. To understand these effects more comprehensively, as future work we are solving the system self consistently to see how the size of different topological regions change in a microscopic model. This can help predict the contrasting behavior of plateaus originating from topology versus originating from disorder as a function of the experimental conditions with greater confidence.

The above experimental issues in this system are specific to the efforts to observe 2D topological superconducting phase and are not necessarily an issue for the 1D topological superconductivity through fabricating quasi 1D structures. This is because of the larger system size of the 2D possibly limiting the coherently induce proximity gap and the $N = 1$ phase being predicted as an intermediate phase when the normal part is under quantum Hall transition. Thus making disorder an unavoidable feature. The 1D topological superconductivity studied in Chapter 3 of this thesis is not affected by these factors because of, (i) of the smaller size of the 1D system, and (ii) the non-trivial $\mathbb{Z}_2 = -1$ phase in 1D limit is achieved when the normal part is deep in its quantum anomalous Hall phase, thus the disorder issues become irrelevant. Hence the quasi 1D structures based on the quantum anomalous Hall device is a promising platform to create and manipulate Majorana zero modes.

Finally, the earlier theory work [25] on which the above mentioned experiments are based, does not consider the effect of vortex lattice. Even though the experiments are performed at very weak magnetic field, the inherent thin film nature of the superconductor implies that even at small magnetic field the

superconductor is in its vortex lattice phase[1]. Chapter 4 of this thesis makes progress in this direction. We show that under vortex lattice state, the type of vortex lattice can determine if the system can host even or odd number of chiral Majorana edge states. One can imagine tuning the vortex lattice in this system to observe the effect on the experimental conductance plateau, since if they are induced by disorder their tunability via vortex lattice is not expected.

[1]The active system size in the experiment is about 1mm $\times$ 1mm and the half-quantized plateau are observed at $B \sim 0.02T$ and $B \sim 0.2T$, which corresponds to average inter-vortex separation of about $185nm$ and 60nm.

Appendices

Appendix A

Berry curvature

Here for a general 2×2 Hamiltonian, we show the the conventional expression for Berry curvature, which involves derivatives on eigenstates is same as the solid angle expression used in main text 2.2.1. A general 2×2 Hamiltonian projected over the Pauli matrices,

$$\mathcal{H}(\boldsymbol{k}) = h_0(\boldsymbol{k})\sigma_0 + \mathbf{h}(\boldsymbol{k})\cdot\boldsymbol{\sigma}\,. \tag{A.1}$$

has eigenvalues and normalized eigenvectors

$$E_{\mp}(\boldsymbol{k}) = h_0(\boldsymbol{k}) \mp |\boldsymbol{h}(\boldsymbol{k})|\,, \tag{A.2a}$$

$$u_{\mp}(\boldsymbol{k}) = \left(\mp\frac{h_x(\boldsymbol{k}) - ih_y(\boldsymbol{k})}{\sqrt{2(|\boldsymbol{h}(\boldsymbol{k})| \pm h_z(\boldsymbol{k}))|\boldsymbol{h}(\boldsymbol{k})|}},\ \sqrt{\frac{|\boldsymbol{h}(\boldsymbol{k})| \pm h_z(\boldsymbol{k})}{2|\boldsymbol{h}(\boldsymbol{k})|}}\right)^T. \tag{A.2b}$$

For the further discussion, it is convenient to parametrize the eigenvectors in the following form:

$$u_{-}(\boldsymbol{k}) = \left(-e^{i\phi_k}\sin\frac{\theta_k}{2},\ \cos\frac{\theta_k}{2}\right)^T, \tag{A.3a}$$

$$u_{+}(\boldsymbol{k}) = \left(e^{i\phi_k}\cos\frac{\theta_k}{2},\ \sin\frac{\theta_k}{2}\right)^T, \tag{A.3b}$$

such that

$$\sqrt{\frac{|\boldsymbol{h}(\boldsymbol{k})| + h_z(\boldsymbol{k})}{2|\boldsymbol{h}(\boldsymbol{k})|}} = \sqrt{\frac{1}{2}(1+\cos\theta_k)} = \cos\frac{\theta_k}{2}\,, \tag{A.4a}$$

$$\sqrt{\frac{|\boldsymbol{h}(\boldsymbol{k})| - h_z(\boldsymbol{k})}{2|\boldsymbol{h}(\boldsymbol{k})|}} = \sqrt{\frac{1}{2}(1-\cos\theta_k)} = \sin\frac{\theta_k}{2}\,, \tag{A.4b}$$

and

$$\frac{-h_x(\boldsymbol{k}) + ih_y(\boldsymbol{k})}{\sqrt{2[|\boldsymbol{h}(\boldsymbol{k})| + h_z(\boldsymbol{k})]|\boldsymbol{h}(\boldsymbol{k})|}} = -e^{i\phi_k}\,\sin\frac{\theta_k}{2}\,, \tag{A.5a}$$

$$\frac{h_x(\boldsymbol{k}) - ih_y(\boldsymbol{k})}{\sqrt{2[|\boldsymbol{h}(\boldsymbol{k})| - h_z(\boldsymbol{k})]|\boldsymbol{h}(\boldsymbol{k})|}} = e^{i\phi_k}\,\cos\frac{\theta_k}{2}\,. \tag{A.5b}$$

The Berry curvature of the n^{th} band is defined as

$$\begin{aligned}\boldsymbol{\Omega}_n(\boldsymbol{k}) &= -i\boldsymbol{\nabla}_{\boldsymbol{k}} \times \langle u_n(\boldsymbol{k})|\boldsymbol{\nabla}_{\boldsymbol{k}}|u_n(\boldsymbol{k})\rangle \\ &= -i\left(\left\langle \frac{\partial u_n(\boldsymbol{k})}{\partial k_x}\middle|\frac{\partial u_n(\boldsymbol{k})}{\partial k_y}\right\rangle - \left\langle \frac{\partial u_n(\boldsymbol{k})}{\partial k_y}\middle|\frac{\partial u_n(\boldsymbol{k})}{\partial k_x}\right\rangle\right)\hat{z}\end{aligned} \tag{A.6}$$

The evaluation of the Berry curvature requires the derivative of the eigenvectors with respect to $k_j\,; j = x, y$. The derivatives follow:

$$\frac{\partial u_-(\boldsymbol{k})}{\partial k_j} = \left(-e^{i\phi_k}\left[\frac{1}{2}\cos\frac{\theta_k}{2}\frac{\partial\theta_k}{\partial k_j} + i\sin\frac{\theta_k}{2}\frac{\partial\phi_k}{\partial k_j}\right],\ -\frac{1}{2}\sin\frac{\theta_k}{2}\frac{\partial\theta_k}{\partial k_j}\right)^T, \tag{A.7a}$$

$$\frac{\partial u_+(\boldsymbol{k})}{\partial k_j} = \left(-e^{i\phi_k}\left[\frac{1}{2}\sin\frac{\theta_k}{2}\frac{\partial\theta_k}{\partial k_j} - i\cos\frac{\theta_k}{2}\frac{\partial\phi_k}{\partial k_j}\right],\ \frac{1}{2}\cos\frac{\theta_k}{2}\frac{\partial\theta_k}{\partial k_j}\right)^T. \tag{A.7b}$$

Substituting Eq. A.7 in the Berry curvature expression in Eq. A.6 takes the values for the lower and the upper band respectively

$$-i\left\langle \frac{\partial u_-}{\partial k_x}\middle|\frac{\partial u_-}{\partial k_y}\right\rangle + i\left\langle \frac{\partial u_-}{\partial k_y}\middle|\frac{\partial u_-}{\partial k_x}\right\rangle = \frac{1}{2}\sin\theta_k\left(\frac{\partial\phi_k}{\partial k_y}\frac{\partial\theta_k}{\partial k_x} - \frac{\partial\phi_k}{\partial k_x}\frac{\partial\theta_k}{\partial k_y}\right), \tag{A.8a}$$

$$-i\left\langle \frac{\partial u_+}{\partial k_x}\middle|\frac{\partial u_+}{\partial k_y}\right\rangle + i\left\langle \frac{\partial u_+}{\partial k_y}\middle|\frac{\partial u_+}{\partial k_x}\right\rangle = -\frac{1}{2}\sin\theta_k\left(\frac{\partial\phi_k}{\partial k_y}\frac{\partial\theta_k}{\partial k_x} - \frac{\partial\phi_k}{\partial k_x}\frac{\partial\theta_k}{\partial k_y}\right), \tag{A.8b}$$

which can be cast into the expression of Berry curvature that depends on the the elements of the 2×2 Hamiltonian

$$\begin{aligned}\boldsymbol{\Omega}_{n=\mp}(\boldsymbol{k}) &= \frac{(n=\pm 1)}{2}\sin\theta_k\left(\frac{\partial\phi_k}{\partial k_y}\frac{\partial\theta_k}{\partial k_x} - \frac{\partial\phi_k}{\partial k_x}\frac{\partial\theta_k}{\partial k_y}\right)\hat{z}\,, \\ &= \pm\hat{\boldsymbol{h}}(\boldsymbol{k})\cdot\left(\frac{\partial\hat{\boldsymbol{h}}(\boldsymbol{k})}{\partial k_x}\times\frac{\partial\hat{\boldsymbol{h}}(\boldsymbol{k})}{\partial k_y}\right).\end{aligned} \tag{A.9}$$

In the BdG construction because of the particle-hole redundancy introduced by doubling the Hilbert space, one only need to consider the lower band. The Berry curvature is simply the solid angle expression in the Eq. 2.21 of chapter 2.

Appendix B

Magnetic topological insulator/superconductor phase boundaries

Here we derive some exact relations to describe topological phase boundaries for the magnetic TI thin film proximity coupled to an s-wave superconductor studied in chapter 3. Since all the interesting low energy physics appears near Γ-point, it suffices to consider the gap closing and opening at Γ point as the source of topological phase transitions. The BdG Hamiltonian is obtained at Γ-point

$$H_{BdG} = \begin{pmatrix} H_0(0) & \hat{\Delta} \\ \hat{\Delta}^\dagger & -H_0^*(0)\,, \end{pmatrix} \tag{B.1}$$

where H_0 is defined in Eq. 3.6 and $\hat{\Delta}$ is defined in Eq. 3.4. We consider the case of $\mu = \lambda' = 0$. For a realistic system with superconductor only introducing pair potential in bottom layer, $\Delta_t = 0$. Substitution of $k_x = k_y = 0$, simplifies the 8×8 BdG Hamiltonian and allows for simple exact expressions for topological phase boundaries even for the realistic parameters.

The topological phase boundaries are described by following 8 equations:

$$\pm \frac{1}{2}(\Delta + \sqrt{4m^2 + \Delta^2} + 2\lambda) = 0 \tag{B.2a}$$

$$\pm \frac{1}{2}(\Delta - \sqrt{4m^2 + \Delta^2} - 2\lambda) = 0 \tag{B.2b}$$

$$\pm \frac{1}{2}(\Delta - \sqrt{4m^2 + \Delta^2} + 2\lambda) = 0 \tag{B.2c}$$

$$\pm \frac{1}{2}(\Delta + \sqrt{4m^2 + \Delta^2} - 2\lambda) = 0\,. \tag{B.2d}$$

The Fig. 3.4 (b) in chapter 3 simply plots these curves when normalized by m.

Appendix C

Pairing matrix elements in Landau level basis

In this section we derive expression for pairing matrix element in the Landau level basis. The evaluation involves calculating the integral in Eq. 4.7. For the sake of generality, the pair potential $\Delta(\boldsymbol{r})$ when solved self consistently in the parent superconductor, takes the form of sum of different COM channels j [70]:

$$\Delta(\boldsymbol{r}) = \sum_{j,t} \Delta_{j,t} \phi_{j,\sqrt{2}\,t a_y}(\sqrt{2}\boldsymbol{r})\,. \tag{C.1}$$

The pair potential used in the main text is simply just keeping only the $j = 0$ channel of the above form. The pairing matrix element between non relaticistic 2DEG Landau levels as shown in Eq. 4.7

$$\mathcal{G}^{N,M}_{Y,Y'} = \sum_{t,j} \int d\boldsymbol{r} \Delta_t \phi_{j,\sqrt{2}ta_y}(\sqrt{2}\boldsymbol{r}) \phi^*_{N,Y}(\boldsymbol{r}) \bar{\phi}_{M,Y'}(\boldsymbol{r})\,, \tag{C.2}$$

after substituting the pair potential, the matrix element involves integrals over product of three Landau level wavefunctions. Since $\bar{\phi}_{M,Y'} = \phi^*_{M,-Y'}$, transforming $Y' \to -Y'$(since it is just a dummy variable in current form), and using the transformation to the COM and relative coordinate systems, the identity [69]

$$\phi_{N,Y}(\boldsymbol{r_1}) \phi_{M,Y'}(\boldsymbol{r_2}) = \sum_j \mathcal{B}^{N,M}_j \phi^R_{j,Y_c}([\boldsymbol{r_1} + \boldsymbol{r_2}]/2) \phi^r_{N+M-j,Y_r}(\boldsymbol{r_1} - \boldsymbol{r_2})\,, \tag{C.3}$$

can be used. Here the transformation matrix $\mathcal{B}^{N,M}_j$ is defined in Eq. 4.11, Y_c, and Y_r are COM and relative guiding centers respectively. The transformation to COM and relative coordinates simplifies pairing matrix elements following

the steps:

$$\begin{aligned}\mathcal{G}^{N,M}_{Y,Y'} &= \sum_t \sum_{j,j'} [\Delta_{t,j} \mathcal{B}^{N,M}_{j'} \phi^{r*}_{N+M-j',Y_r}(0) \int d\boldsymbol{r} \phi_{j,\sqrt{2}ta_y}(\sqrt{2}\boldsymbol{r}) \phi^{R*}_{j',Y_c}(\boldsymbol{r})] \\ &= \sum_t \sum_{j,j'} [\Delta_{t,j} \mathcal{B}^{N,M}_{j'} \varphi_{N+M-j'}\left(-\frac{Y_r}{\sqrt{2}\ell}\right) \frac{\delta_{Y_c,ta_y}}{\sqrt{L_x}} \\ &\qquad \times \int dy \varphi_j\left(\frac{\sqrt{2}}{\ell}(y - ta_y)\right) \varphi_{j'}\left(\frac{\sqrt{2}}{\ell}(y - Y_c)\right)] \,. \end{aligned} \tag{C.4}$$

Here $Y_c = (Y + Y')/2$ and $Y_r = Y - Y'$. The pairing matrix element is then

$$\mathcal{G}^{N,M}_{Y,Y'} = \sum_{t,j} \Delta_{t,j} \mathcal{B}^{N,M}_{j} \varphi_{N+M}\left(-\frac{Y_r}{\sqrt{2}\ell}\right) \frac{\delta_{Y+Y',2ta_y}}{\sqrt{L_x}} \,, \tag{C.5}$$

which after sum over t and using Eq. 4.10 and substituting $\chi_{|N|+|M|-j}$ for $\varphi_{|N|+|M|-j}$ is the same as written in Eq. 4.9 of the main text. When the guiding centers are represented by integer stripe index and a continuum as described in main text, the COM and relative guiding centers are described as,

$$Y_c = (s + s')a_y/2 + (k_x + k'_x)\ell^2/2 \,, \tag{C.6a}$$

$$Y_r = (s - s')a_y + (k_x - k'_x)\ell^2 \,, \tag{C.6b}$$

and the condition δ_{Y_c,ta_y}, gives $k_x = -k'_x$, $s + s' = 2t$. The above matrix elements are calculated in the non-relativistic 2DEG Landau level basis for the compactness of the expression, however, all the numerical calculation in our main text are performed in Dirac Landau level basis. The transformation of the above algebra to Dirac Landau levels N and M follows simply as,

$$\begin{aligned}\mathcal{F}^{N,M}_{Y,Y'} &= \sum_t \int d\boldsymbol{r} \Delta_t \phi_{0,\sqrt{2}ta_y}(\sqrt{2}\boldsymbol{r}) \psi^*_{N,Y}(\boldsymbol{r}) \bar{\psi}_{M,Y'}(\boldsymbol{r}) \\ &= \mathcal{N}_N \mathcal{N}_M \sum_t \int d\boldsymbol{r} \Delta_t \phi_{0,\sqrt{2}ta_y}(\sqrt{2}\boldsymbol{r}) \\ &\qquad \times [S_N \phi^*_{|N|-1,Y}(\boldsymbol{r}) \bar{\phi}_{|M|,Y'}(\boldsymbol{r}) - S_M \phi^*_{|N|,Y}(\boldsymbol{r}) \bar{\phi}_{|M|-1,Y'}(\boldsymbol{r})] \,, \end{aligned} \tag{C.7}$$

which simplifies to

$$\mathcal{F}^{N,M}_{Y,Y'} = \sum_t \Delta_t \mathcal{D}^{N,M}_0 \varphi_{N+M}\left(-\frac{Y_r}{\sqrt{2}\ell}\right)\frac{\delta_{Y+Y',2ta_y}}{\sqrt{L_x}}\,. \tag{C.8}$$

Above only $j = 0$ pairing channel is retained. Here $\mathcal{D}^{N,M}_j$ is defined in Eq. 4.19 of the main text. Using the integer stripe index and continuum label representation for the guiding center in Eq. C.8, one can obtain Eq. 4.18 of main text.

Appendix D

Vortex lattice symmetry and magnetic Bloch states

When the superconductor has vortex lattice symmetry, such that $|\Delta_{t+q}| = |\Delta_t|$, we first write the integer index s of the guiding center as $pq + m$, such that

$$Y = (pq + m)a_y + k_x\ell^2\,, \tag{D.1a}$$

$$Y' = (p'q + m')a_y - k_x\ell^2\,. \tag{D.1b}$$

Then the pairing matrix element coupling guiding centers Y and Y' in this representation is given by

$$\begin{aligned}\mathcal{F}^{N,M}_{\{p,m\};\{p',m'\}}(k_x) = &\sum_{t,n}\Delta_{tq+n}\delta_{p+p',2t}\delta_{m+m',2n} \\ &\times \chi_{|N|+|M|-1}([q(p-p') + (m-m')]a_y + 2k_x\ell^2)\,.\end{aligned} \tag{D.2}$$

In this representation the BdG matrix equation takes the form (only the upper block shown, lower block follows trivially):

$$\begin{aligned}&\xi_N u^\nu_{N,p,m}(k_x) + \sum_{M,p',m'}\mathcal{F}^{N,M}_{\{p,m\};\{p',m'\}}(k_x)v^\nu_{M,p',m'}(k_x) = Eu^\nu_{N,p,m}(k_x) \\ &\implies \xi_N u^\nu_{N,p,m}(k_x) + \sum_{M}\mathcal{F}^{N,M}_{\{p,m\};\{2t-p,2n-m\}}(k_x)v^\nu_{M,2t-p,2n-m}(k_x) = Eu^\nu_{N,p,m}(k_x)\end{aligned} \tag{D.3}$$

To diagonalize the above matrix equations, we now transform to the magnetic Bloch states defined on the electron and hole part of the Landau level basis in the BdG equations respectively

$$\phi_{N,m,\boldsymbol{k}}(\boldsymbol{r}) = \sqrt{\frac{qa_y}{L_y}} \sum_t \mathrm{e}^{ik_y(qt+m)a_y} \mathrm{e}^{i\pi\lambda qt(t-1)/2} \mathrm{e}^{i(\pi\lambda m-\theta/2)t} \phi_{N,k_x\ell^2+(qt+m)a_y}(\boldsymbol{r})\,, \tag{D.4a}$$

$$\phi^*_{N,m,-\boldsymbol{k}}(\boldsymbol{r}) = \sqrt{\frac{qa_y}{L_y}} \sum_t \mathrm{e}^{ik_y(qt+m)a_y} \mathrm{e}^{-i\pi\lambda qt(t-1)/2} \mathrm{e}^{-i(\pi\lambda m-\theta/2)t} \phi^*_{N,-k_x\ell^2+(qt+m)a_y}(\boldsymbol{r})\,. \tag{D.4b}$$

Now after expanding the eigenvector as

$$\Psi^\nu_{m,\boldsymbol{k}}(\boldsymbol{r}) = (\sum_N u^\nu_{N,m,\boldsymbol{k}} \psi_{N,m,\boldsymbol{k}}(\boldsymbol{r}),\ \sum_N v^\nu_{N,m,\boldsymbol{k}} \psi^*_{N,m,-\boldsymbol{k}}(\boldsymbol{r}))^T\,, \tag{D.5}$$

the upper BdG block diagonalization equation

$$\xi_N u^\nu_{N,n}(\boldsymbol{k}) + \sum_{M,m} \mathcal{F}^{N,M}_{n,m}(\boldsymbol{k}) v^\nu_{M,m}(k_x) = E(\boldsymbol{k}) u^\nu_{N,n}(\boldsymbol{k})\,, \tag{D.6}$$

is obtained for $n \in [0, .., q-1]$. Here the Fourier representation of the pairing matrix element is obtained as:

$$\mathcal{F}^{N,M}_{n,m}(\boldsymbol{k}) = \mathcal{D}^{N,M}_0 \sum_t \Delta_{qt+(n+m)/2} \mathrm{e}^{-i\pi\lambda qt(t-1)} \mathrm{e}^{-i(2\pi\lambda n-\theta)t} \mathrm{e}^{ik_y a_y(2qt+n-m)} \times \chi_{|N|+|M|-1}[(2qt+n-m)a_y + 2k_x\ell^2]\,. \tag{D.7}$$

For the purpose of the discussion next in App. E, we also explicitly write down the pairing matrix element for electrons in ordinary non-relativistic 2DEG Landau levels:

$$\mathcal{G}^{N,M}_{n,m}(\boldsymbol{k}) = \mathcal{B}^{N,M}_0 \sum_t \Delta_{qt+(n+m)/2} \mathrm{e}^{-i\pi\lambda qt(t-1)} \mathrm{e}^{-i(2\pi\lambda n-\theta)t} \mathrm{e}^{ik_y a_y(2qt+n-m)} \times \chi_{N+M}[(2qt+n-m)a_y + 2k_x\ell^2]\,. \tag{D.8}$$

Appendix E

Superconductivity in non-relativistic 2DEG Landau level

Here, we extend the discussion in the chapter 4 to the non-relativistic 2DEG Landau levels and show the main results of inducing superconductivity in quantum Hall regime and the connection between vortex lattice structure and odd-$\mathbb{Z}$ classification of topological superconductivity is insensitive to this detail. Although the low field limit of the two cases is dramatically different. To convey the main point through simplified analysis, we consider only the $q = 1$ case.

To have a good comparative understanding of the two cases, first consider the single Landau level limit. When μ is exactly at Landau level energy, the spectrum:

$$E(\boldsymbol{k}) = \begin{cases} \pm|\mathcal{F}^{N,N}(\boldsymbol{k})| & \text{Dirac Landau level}\,, \\ \pm|\mathcal{D}^{N,N}(\boldsymbol{k})| & \text{Ordianry 2DEG}\,. \end{cases} \tag{E.1}$$

only differs through the order of the Hermite polynomial appearing in the pairing matrix element. Now notice that, the single Landau level pairing matrix element for Dirac Landau level has odd Hermite polynomial of order $2|N|-1$, while for ordinary 2DEG, has even Hermite polynomial of order $2N$. Because of this, $\mathcal{F}^{N,N}(\boldsymbol{k}) = -\mathcal{F}^{N,N}(-\boldsymbol{k})$ and $\mathcal{D}^{N,N}(\boldsymbol{k}) = \mathcal{D}^{N,N}(-\boldsymbol{k})$. Hence, irrespective of type of vortex lattice, the BdG Hamiltonian in single Landau level is odd parity for Dirac case and even parity for ordinary non-relativistic 2DEG case. This means only the Dirac case in its single Landau level limit can be an effective p-wave system. Now focusing on only $\boldsymbol{k} = 0$ point, the Dirac case is gapless at that point with Dirac touching point, while ordinary 2DEG case is generally not.

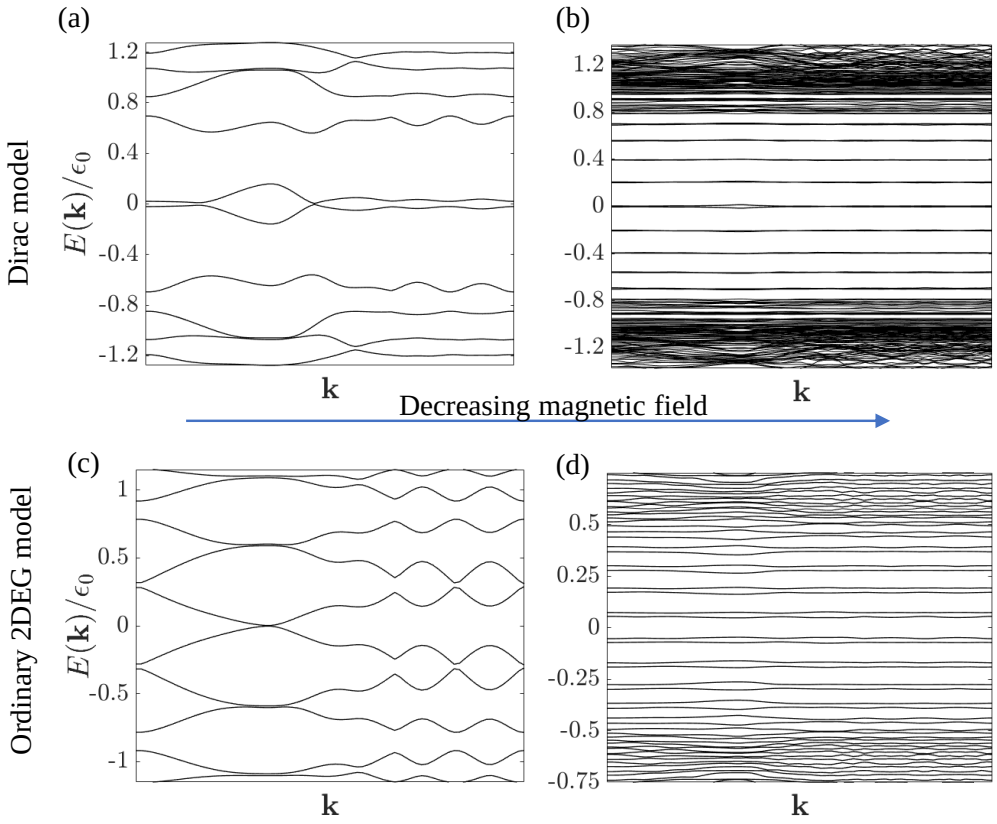

Figure E.1: Bulk BdG quasiparticle spectrum at strong (a) and (c) vs weak (b) and (d) field. For the Dirac model of the normal state, as the magnetic field is decreased the lowest energy vortex core bound states are at zero energy as shown in (b). This indicates the system is effective p-wave superconductor as predicted by Fu-Kane model [22]. In contrast when Landau levels of ordinary 2DEG are proximity coupled to s-wave superconductor, in the weak field limit, the lowest vortex core bound state is at finite energy as shown in (d). This is expected for an s-wave superconductor. Figure is reproduced from the research article arXiv1903.12249.

The discussion in single Landau limit, although brings out qualitative difference between effective pairing symmetry of Dirac Landau level case compared to non-relativistic 2DEG Landau level case, however under our con-

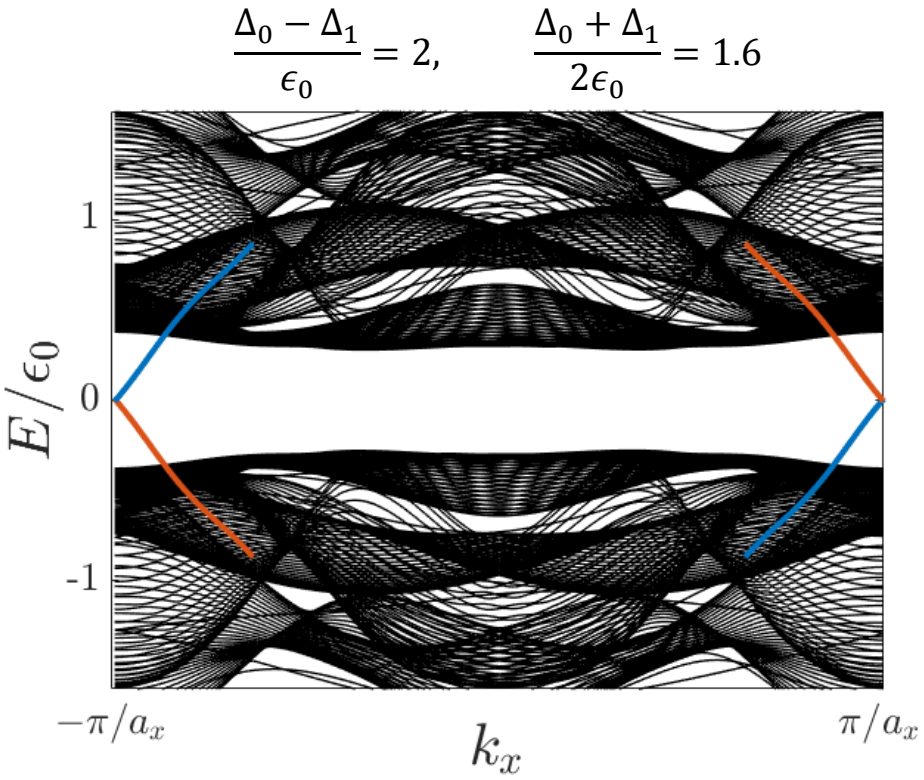

Figure E.2: A representative case of finite width spectrum (in the units of $\epsilon_0 = \hbar\omega_c$ of two ordinary 2DEG Landau levels proximity coupled to an s-wave superconductor. For clarity, we have removed the non topological edge state from the figure. The red and blue denote opposite edges. Hence, the system has exactly one chiral edge mode. The parameters are chosen fictitiously, such that Landau level gaps and superconducting pair potential amplitudes are comparable. Figure is reproduced from the research article arXiv1903.12249.

struction single Landau level cannot drive topological phase changes in either scenario. If we turn to the opposite limit of weak magnetic field where many Landau levels contribute to pairing, the situation is again dramatically different for Dirac and ordinary non-relativistic 2DEG case. Dirac case with $\mathcal{T}$-symmetry proximitized to an s-wave superconductor is shown to be an effective p-wave superconductor [22], while the ordinary 2DEG case is s-wave superconductor. This can be seen in the Fig. E.1(b) and (d). In the isolated

vortex limit, which is relevant at weak magnetic field, an s-wave superconductor binds Caroli-de Gennes-Matricon states to the vortex core, which have energy levels $E_n \sim (n + 1/2)\Delta^2/E_F$, where Δ is the superconducting gap and E_F is the Fermi energy and n is a positive integer [123]. This can be seen by the finite energy of the lowest energy band in Fig. E.1(d). In contrast for the p-wave superconductor vortex core levels have energy $E_n \sim n\Delta^2/E_F$ [124]. This is evident in the Fig. E.1 (b) with the zero energy band of vortex core states. In terms of possibility of Majorana, this means the Dirac case can bind Majorana zero modes at the vortex core under suitable conditions, while the vortex core bound states for non-relativistic 2DEG case is always complex fermion because of the associated finite energy.

For the intermediate limit of a few Landau level, which is of focus in chapter 4, the qualitative physics for Dirac and non-relativistic 2DEG is similar. In particular, in context of possibility of odd or even number of chiral Majorana edge modes, the vortex lattice structure is the main tuning knob. As shown in Fig E.2 for a representative case of two landau level model of ordinary 2DEG, the odd number of chiral Majorana edge modes can be achieved by suitable tuning of Landau level gap, superconducting pair potential and vortex lattice structure.

Appendix F

Sum of particle-particle ladder diagrams

In this section we calculate the particle-particle ladder diagrams already calculated in chapter 5 in detail. While doing so, we derive some of the identities used in Sec. 5.2. This section should be read alongside Sec. 5.2. The diagrams upto second order are shown in Fig. F.1. The calculations are presented by showing interaction order by order for first two order and n^{th} order and then deriving their sum.

F.1 First order interaction

The interaction matrix element for δ function interaction between the pair of non-relativistic Landau levels can be evaluated using the transformation to the COM and relative states:

$$\begin{aligned}
&\langle \phi_{N,Y_c+Y_r/2}(\boldsymbol{r}_1)\phi_{M,Y_c-Y_r/2}(\boldsymbol{r}_2)|V_0\delta(\boldsymbol{r}_1-\boldsymbol{r}_2)|\phi_{N',Y_c'+Y_r'/2}(\boldsymbol{r}_1)\phi_{M',Y_c'-Y_r'/2}(\boldsymbol{r}_2)\rangle \\
&= V_0\sum_{j,j'}\mathcal{B}_j^{N,M}\mathcal{B}_{j'}^{N',M'}\phi^{r*}_{N+M-j,Y_r}(0)\phi^{r}_{N'+M'-j',Y_r'}(0)\int d\boldsymbol{R}\phi^{R*}_{j,Y_c}(\boldsymbol{R})\phi^{R}_{j',Y_c'}(\boldsymbol{R}) \\
&= \frac{V_0}{L_x}\sum_{j}\mathcal{B}_j^{N,M}\mathcal{B}_{j}^{N',M'}\phi^{r}_{N+M-j}(-Y_r)\phi^{r}_{N'+M'-j}(-Y_r')\,. \qquad \text{(F.1)}
\end{aligned}$$

For the double band system considered in chapter 5, the interactions diagonal in the layer index take the form $\hat{V} = V_0\delta(\boldsymbol{r})\sigma_0$, the interaction matrix element

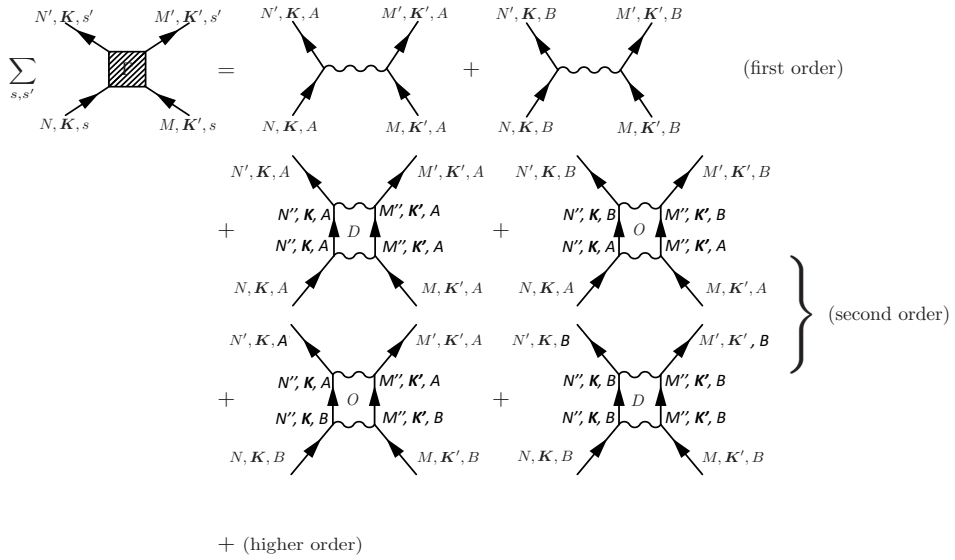

Figure F.1: The illustration of the type of ladder diagrams calculated here: For bilayer graphene A and B denote the two layer and for monolayer graphene they denote two sublattices. The interaction line is diagonal in A and B, however the free particle propagation is not because the non-interacting Landau level eigenstates are not diagonal in A and B.

evaluates to

$$\begin{aligned}\langle N, Y_r/2; M, -Y_r/2|\, \hat{V}\delta(\boldsymbol{r}_1-\boldsymbol{r}_2)\,|N', Y_r'/2; M', -Y_r'/2\rangle \\ = \frac{V_0}{L_x}\mathcal{N}_N\mathcal{N}_M\mathcal{N}_{N'}\mathcal{N}_{M'}\sum_j [S_N S_{N'}\mathcal{B}_j^{|N|-1,|M|+\gamma-1}\mathcal{B}_j^{|N'|-1,|M'|+\gamma-1} \\ + S_M S_{M'}\mathcal{B}_j^{|N|+\gamma-1,|M|-1}\mathcal{B}_j^{|N'|+\gamma-1,|M'|-1}] \\ \times \phi^r_{|N|+|M|+\gamma-2-j}(-Y_r)\phi^r_{|N'|+|M'|+\gamma-2-j}(-Y')\,. \quad \text{(F.2)}\end{aligned}$$

Above the COM guiding center labels are removed from the expression since COM guiding center is conserved during interaction.

F.2 Second order interaction

For the single band non-relativistic 2DEG, there is only one second order diagram, which is evaluated as

$$\begin{aligned}
&\sum_{N'',M'',Y''} \mathcal{K}^0_{N'',M''} \langle N, Y_r/2; M, -Y_r/2| \hat{V} |N'', Y''_r/2; M'', -Y''_r/2\rangle_0 \\
&\qquad\qquad \times \langle N'', Y''_r/2; M'', -Y''_r/2| \hat{V} |N', Y'_r/2; M', Y'_r/2\rangle_0 \\
&= \left(\frac{V_0}{L_x}\right)^2 \sum_j \phi^r_{N+M-j}(-Y_r)\phi^r_{N'+M'-j}(-Y'_r)\mathcal{B}^{N,M}_j \mathcal{B}^{N',M'}_j \sum_{N'',M''} \mathcal{K}^0_{N'',M''} (\mathcal{B}^{N'',M''}_j)^2 \,.
\end{aligned} \tag{F.3}$$

In contrast for the two band systems considered in chapter 5, there are four diagrams at the second order as shown in the Fig. F.1. The second order ladder diagrams are then the sum of these four diagrams represented algebraically below:

$$\begin{aligned}
&\sum_{N'',M'',Y''} \mathcal{K}^\gamma_{N'',M''} \langle N, Y_r/2; M, -Y_r/2| \hat{V} |N'', Y''_r/2; M'', -Y''_r/2\rangle_\gamma \\
&\qquad\qquad \times \langle N'', Y''_r/2; M'', -Y''_r/2| \hat{V} |N', Y'_r/2; M', Y'_r/2\rangle_\gamma \\
&= \left(\frac{V_0}{L_x}\right)^2 \mathcal{N}_N \mathcal{N}_M \mathcal{N}_{N'} \mathcal{N}_{M'} \sum_j \phi^r_{|N|+|M|+\gamma-2-j}(-Y_r)\phi^r_{|N'|+|M'|+\gamma-2-j}(-Y'_r) \\
&\times \Bigg\{ \Bigg[(S_N S_{N'} \underbrace{\mathcal{B}^{|N|-1,|M|+\gamma-1}_j \mathcal{B}^{|N'|-1,|M'|+\gamma-1}_j}_{\text{AAA'A'}} + S_M S_{M'} \underbrace{\mathcal{B}^{|N|+\gamma-1,|M|-1}_j \mathcal{B}^{|N'|+\gamma-1,|M'|-1}_j}_{\text{BBB'B'}}) \\
&\qquad \times \sum_{N'',M''} (\mathcal{N}_{N''}\mathcal{N}_{M''} S_{N''})^2 \mathcal{K}^\gamma_{N'',M''} \underbrace{(\mathcal{B}^{|N''|-1,|M''|+\gamma-1}_j)^2}_{\text{A"A"A"A"/B"B"B"B"}} \Bigg] \\
&\quad + \Bigg[(S_N S_{M'} \underbrace{\mathcal{B}^{|N|-1,|M|+\gamma-1}_j \mathcal{B}^{|N'|+\gamma-1,|M'|-1}_j}_{\text{AAB'B'}} + S_M S_{N'} \underbrace{\mathcal{B}^{|N|+\gamma-1,|M|-1}_j \mathcal{B}^{|N'|-1,|M'|+\gamma-1}_j}_{\text{BBA'A'}}) \\
&\qquad \times \sum_{N'',M''} (\mathcal{N}_{N''}\mathcal{N}_{M''})^2 S_{N''} S_{M''} \mathcal{K}^\gamma_{N''M''} \underbrace{B^{|N''|-1,|M''|}_j B^{|N''|,|M''|-1}_j}_{\text{A"A"B"B"/B"B"A"A"}} \Bigg] \Bigg\} \,.
\end{aligned} \tag{F.4}$$

In evaluating the above expressions, the following identities are used:

$$\sum_{Y_r} \phi^r_{|N|+|M|-j}(-Y_r)\phi^r_{|N|+|M|-j'}(-Y_r) = \delta_{j,j'}\,, \tag{F.5a}$$

$$(\mathcal{B}^{N,M}_j)^2 = (\mathcal{B}^{M,N}_j)^2\,. \tag{F.5b}$$

These identities are used in the evaluation of all the higher order diagrams without further mention. In particular the identity in Eq. F.5a allows the separation of diagrams as sum of COM channels.

For compactness, we represent the diagonal and off-diagonal terms of the pair propagator given below by D_j and Q_j respectively

$$D_{j,\gamma} = \frac{V_0}{L_x}\sum_{N,M} (\mathcal{N}_N\mathcal{N}_M S_N)^2\, \mathcal{K}^{\gamma}_{N,M}(\mathcal{B}^{|N|-1,|M|+\gamma-1}_j)^2\,, \tag{F.6a}$$

$$Q_{j,\gamma} = \frac{V_0}{L_x}\sum_{N,M} (\mathcal{N}_N\mathcal{N}_M)^2\, S_N S_M \mathcal{K}^{\gamma}_{N,M}\mathcal{B}^{|N|-1,|M|+\gamma-1}_j \mathcal{B}^{|N|+\gamma-1,|M|-1}_j\,. \tag{F.6b}$$

F.3 n^{th} order interation

For the simple single band quadratically dispersing 2DEG, the n^{th} order diagram sum is rather straightforward:

$$\begin{aligned}
&\langle N, Y_r/2; M, -Y_r/2| \\
&\qquad \times \Bigg[\hat{V}\Big(\sum_{N'',M'',Y''} \mathcal{K}^0_{N'',M''}|N'', Y''_r/2; M''-Y''_r/2\rangle\langle N'', Y''_r/2; M''-Y''_r/2|\hat{V}\Big)^n \\
&\qquad\qquad\qquad\qquad \times |N', Y'_r/2; M', Y'_r/2\rangle_0 \\
&= \left(\frac{V_0}{L_x}\right)^n \sum_j \phi^r_{N+M-j}(-Y_r)\phi^r_{N'+M'-j}(-Y'_r)\mathcal{B}^{N,M}_j\mathcal{B}^{N',M'}_j \\
&\qquad\qquad \times \left(\sum_{N'',M''} \mathcal{K}^0_{N'',M''}(\mathcal{B}^{N'',M''}_j)^2\right)^{n-1}\,.
\end{aligned} \tag{F.7}$$

For the two band cases, the evaluation of higher order diagram is more conveniently evaluated in pair of orders. For example evaluation of $(n)^{th}$ +

$(n+1)^{th}$ order diagrams can be done rather easily because of the odd and even order combination. We substitute $n = 2m$ and the diagram sum for the two band models follow:

$$
\begin{aligned}
&\langle N, Y_r/2; M, -Y_r/2| \\
&\quad \times \Bigg[\hat{V} \Big(\sum_{N'',M'',Y''} \mathcal{K}^{\gamma}_{N'',M''} |N'', Y_r''/2; M'' - Y_r''/2\rangle \langle N'', Y_r''/2; M'' - Y_r''/2| \hat{V} \Big)^{2m} \\
&\quad + \hat{V} \Big(\sum_{N'',M'',Y''} \mathcal{K}^{\gamma}_{N'',M''} |N'', Y_r''/2; M'' - Y_r''/2\rangle \langle N'', Y_r''/2; M'', -Y_r''/2| \hat{V} \Big)^{2m+1} \Bigg] \\
&\qquad\qquad \times |N', Y_r'/2; M', Y_r'/2\rangle_{\gamma} \\
&= \left(\frac{V_0}{L_x} \right)^{2m} \mathcal{N}_N \mathcal{N}_M \mathcal{N}_{N'} \mathcal{N}_{M'} \sum_j \phi^r_{|N|+|M|+\gamma-2-j}(-Y_r) \phi^r_{|N'|+|M'|+\gamma-2-j}(-Y_r') \\
&\times \Bigg\{ \Bigg[(S_N S_{N'} \mathcal{B}_j^{|N|-1,|M|+\gamma-1} \mathcal{B}_j^{|N'|-1,|M'|+\gamma-1} + S_M S_{M'} \mathcal{B}_j^{|N|+\gamma-1,|M|-1} \mathcal{B}_j^{|N'|+\gamma-1,|M'|-1}) \\
&\qquad \times \left(\sum_{p=0}^{p=m} \binom{2m}{2p} D_{j,\gamma}^{2p} Q_{j,\gamma}^{2(m-p)} + \frac{V_0}{L_x} \sum_{p=0}^{m} \binom{2m+1}{2p+1} D_{j,\gamma}^{2p+1} Q_{j,\gamma}^{2(m-p)} \right) \Bigg] \\
&+ \Bigg[(S_N S_{M'} \mathcal{B}_j^{|N|-1,|M|+\gamma-1} \mathcal{B}_j^{|N'|+\gamma-1,|M'|-1} + S_M S_{N'} \mathcal{B}_j^{|N|+\gamma-1,|M|-1} \mathcal{B}_j^{|N'|-1,|M'|+\gamma-1}) \\
&\qquad \times \left(\sum_{p=0}^{p=m-1} \binom{2m}{2p+1} D_{j,\gamma}^{2(m-p)-1} Q_{j,\gamma}^{2p+1} + \frac{V_0}{L_x} \sum_{p=0}^{m} \binom{2m+1}{2p+1} D_{j,\gamma}^{2(m-p)} Q_{j,\gamma}^{2p+1} \right) \Bigg] \Bigg\}.
\end{aligned}
\tag{F.8}
$$

F.4 Sum of all orders

After establishing the general expression of sum of ladder diagram of any order, we need to sum over all orders. For the single band quadratic case, the sum of all orders follow simply from the sum of geometric progression and one can obtain expression consistent with the Ref. [69].

For the double-band case, to perform the sum, we use the following bino-

mial relations:

$$\sum_{p=0}^{p=m} \binom{2m}{2p} D^{2p} Q^{2(m-p)} = \sum_{p=0}^{p=2m} \binom{2m}{p} D^{p} Q^{2m-p} + \sum_{p=0}^{p=2m} \binom{2m}{p} D^{p} (-O)^{2m-p}$$

$$= \frac{(D+Q)^{2m} + (D-Q)^{2m}}{2} \tag{F.9a}$$

$$\sum_{p=0}^{p=m} \binom{2m+1}{2p+1} D^{2p+1} Q^{2(m-p)}$$

$$= \sum_{p=0}^{p=2m+1} \binom{2m+1}{p} D^{p} Q^{2m-p+1} - \sum_{p=0}^{p=2m+1} \binom{2m+1}{p} D^{p} (-Q)^{2m-p+1}$$

$$= \frac{(D+Q)^{2m+1} + (D-Q)^{2m+1}}{2} \,. \tag{F.9b}$$

One can obtain the final expression shown in Eq. 5.15 and Eq. 5.16 in chapter 5.

Bibliography

[1] K. v. Klitzing, G. Dorda, and M. Pepper, "New method for high-accuracy determination of the fine-structure constant based on quantized hall resistance," *Physical Review Letters*, vol. 45, pp. 494–497, aug 1980.

[2] E. Witten, "Three lectures on topological phases of matter," *arXiv:1510.07698*, 2015.

[3] R. E. Prange and S. M. Girvin, eds., *The Quantum Hall Effect*. Springer US, 1987.

[4] A. H. MacDonald, "Introduction to the physics of the quantum hall regime," *arXiv:cond-mat/9410047*, 1994.

[5] D. J. Thouless, M. Kohmoto, M. P. Nightingale, and M. den Nijs, "Quantized hall conductance in a two-dimensional periodic potential," *Physical Review Letters*, vol. 49, pp. 405–408, aug 1982.

[6] Q. Niu, D. J. Thouless, and Y.-S. Wu, "Quantized hall conductance as a topological invariant," *Physical Review B*, vol. 31, pp. 3372–3377, mar 1985.

[7] F. D. M. Haldane, "Model for a quantum hall effect without landau levels: Condensed-matter realization of the "parity anomaly"," *Physical Review Letters*, vol. 61, pp. 2015–2018, oct 1988.

[8] C.-Z. Chang, J. Zhang, X. Feng, J. Shen, Z. Zhang, M. Guo, K. Li, Y. Ou, P. Wei, L.-L. Wang, Z.-Q. Ji, Y. Feng, S. Ji, X. Chen, J. Jia, X. Dai, Z. Fang, S.-C. Zhang, K. He, Y. Wang, L. Lu, X.-C. Ma, and Q.-K. Xue, "Experimental observation of the quantum anomalous hall effect in a magnetic topological insulator," *Science*, vol. 340, pp. 167–170, mar 2013.

[9] D. Xiao, M.-C. Chang, and Q. Niu, "Berry phase effects on electronic properties," *Reviews of Modern Physics*, vol. 82, pp. 1959–2007, jul 2010.

[10] X.-L. Qi and S.-C. Zhang, "Topological insulators and superconductors," *Reviews of Modern Physics*, vol. 83, pp. 1057–1110, oct 2011.

[11] E. Majorana, "Teoria simmetrica dell'elettrone e del positrone," *Il Nuovo Cimento*, vol. 14, pp. 171–184, apr 1937.

[12] E. Majorana and L. Maiani, "A symmetric theory of electrons and positrons," in *Ettore Majorana Scientific Papers*, pp. 201–233, Springer Berlin Heidelberg, 2006.

[13] C. Nayak, S. H. Simon, A. Stern, M. Freedman, and S. Das Sarma, "Non-abelian anyons and topological quantum computation," *Reviews of Modern Physics*, vol. 80, no. 3, pp. 1083–1159, 2008. RMP.

[14] C. Beenakker, "Search for majorana fermions in superconductors," *Annual Review of Condensed Matter Physics*, vol. 4, no. 1, pp. 113–136, 2013.

[15] R. M. Lutchyn, J. D. Sau, and S. Das Sarma, "Majorana fermions and a topological phase transition in semiconductor-superconductor heterostructures," *Physical Review Letters*, vol. 105, no. 7, p. 077001, 2010. PRL.

[16] J. D. Sau, R. M. Lutchyn, S. Tewari, and S. D. Sarma, "Generic new platform for topological quantum computation using semiconductor heterostructures," *Physical Review Letters*, vol. 104, jan 2010.

[17] J. Alicea, "Majorana fermions in a tunable semiconductor device," *Physical Review B*, vol. 81, mar 2010.

[18] J. Alicea, Y. Oreg, G. Refael, F. von Oppen, and M. P. A. Fisher, "Non-abelian statistics and topological quantum information processing in 1d wire networks," *Nature Physics*, vol. 7, pp. 412–417, feb 2011.

[19] V. Mourik, K. Zuo, S. M. Frolov, S. R. Plissard, E. P. A. M. Bakkers, and L. P. Kouwenhoven, "Signatures of majorana fermions in hybrid superconductor-semiconductor nanowire devices," *Science*, vol. 336, no. 6084, pp. 1003–1007, 2012.

[20] A. Das, Y. Ronen, Y. Most, Y. Oreg, M. Heiblum, and H. Shtrikman, "Zero-bias peaks and splitting in an al–InAs nanowire topological superconductor as a signature of majorana fermions," *Nature Physics*, vol. 8, pp. 887–895, nov 2012.

[21] L. P. Rokhinson, X. Liu, and J. K. Furdyna, "The fractional a.c. josephson effect in a semiconductor–superconductor nanowire as a signature of majorana particles," *Nature Physics*, vol. 8, pp. 795–799, sep 2012.

[22] L. Fu and C. L. Kane, "Superconducting proximity effect and majorana fermions at the surface of a topological insulator," *Phys. Rev. Lett.*, vol. 100, p. 096407, Mar 2008.

[23] M.-X. Wang, C. Liu, J.-P. Xu, F. Yang, L. Miao, M.-Y. Yao, C. L. Gao, C. Shen, X. Ma, X. Chen, Z.-A. Xu, Y. Liu, S.-C. Zhang, D. Qian, J.-F. Jia, and Q.-K. Xue, "The coexistence of superconductivity and topological order in the bi2se3 thin films," *Science*, vol. 336, pp. 52–55, mar 2012.

[24] J.-P. Xu, M.-X. Wang, Z. L. Liu, J.-F. Ge, X. Yang, C. Liu, Z. A. Xu, D. Guan, C. L. Gao, D. Qian, Y. Liu, Q.-H. Wang, F.-C. Zhang, Q.-K. Xue, and J.-F. Jia, "Experimental detection of a majorana mode in the core of a magnetic vortex inside a topological insulator-superconductor Bi2Te3/ NbSe2 heterostructure," *Physical Review Letters*, vol. 114, jan 2015.

[25] X.-L. Qi, T. L. Hughes, and S.-C. Zhang, "Chiral topological superconductor from the quantum hall state," *Phys. Rev. B*, vol. 82, p. 184516, Nov 2010.

[26] Q. L. He, L. Pan, A. L. Stern, E. C. Burks, X. Che, G. Yin, J. Wang, B. Lian, Q. Zhou, E. S. Choi, K. Murata, X. Kou, Z. Chen, T. Nie,

Q. Shao, Y. Fan, S.-C. Zhang, K. Liu, J. Xia, and K. L. Wang, "Chiral majorana fermion modes in a quantum anomalous hall insulator-superconductor structure," *Science*, vol. 357, no. 6348, pp. 294–299, 2017.

[27] Y. Zeng, C. Lei, G. Chaudhary, and A. H. MacDonald, "Quantum anomalous hall majorana platform," *Phys. Rev. B*, vol. 97, p. 081102, Feb 2018.

[28] C.-Z. Chen, Y.-M. Xie, J. Liu, P. A. Lee, and K. T. Law, "Quasi-one-dimensional quantum anomalous hall systems as new platforms for scalable topological quantum computation," *Physical Review B*, vol. 97, mar 2018.

[29] S. Nadj-Perge, I. K. Drozdov, J. Li, H. Chen, S. Jeon, J. Seo, A. H. MacDonald, B. A. Bernevig, and A. Yazdani, "Observation of majorana fermions in ferromagnetic atomic chains on a superconductor," *Science*, vol. 346, no. 6209, pp. 602–607, 2014.

[30] H. Kim, A. Palacio-Morales, T. Posske, L. Rózsa, K. Palotás, L. Szunyogh, M. Thorwart, and R. Wiesendanger, "Toward tailoring majorana bound states in artificially constructed magnetic atom chains on elemental superconductors," *Science Advances*, vol. 4, p. eaar5251, may 2018.

[31] A. Palacio-Morales, E. Mascot, S. Cocklin, H. Kim, S. Rachel, D. K. Morr, and R. Wiesendanger, "Atomic-scale interface engineering of majorana edge modes in a 2d magnet-superconductor hybrid system," *arXiv: 1809.04503*, 2018.

[32] J.-X. Yin, Z. Wu, J.-H. Wang, Z.-Y. Ye, J. Gong, X.-Y. Hou, L. Shan, A. Li, X.-J. Liang, X.-X. Wu, J. Li, C.-S. Ting, Z.-Q. Wang, J.-P. Hu, P.-H. Hor, H. Ding, and S. H. Pan, "Observation of a robust zero-energy bound state in iron-based superconductor fe(te,se)," *Nature Physics*, vol. 11, pp. 543–546, jun 2015.

[33] Z. Wang, P. Zhang, G. Xu, L. K. Zeng, H. Miao, X. Xu, T. Qian, H. Weng, P. Richard, A. V. Fedorov, H. Ding, X. Dai, and Z. Fang,

"Topological nature of theFeSe0.5te0.5superconductor," *Physical Review B*, vol. 92, sep 2015.

[34] X. Wu, S. Qin, Y. Liang, H. Fan, and J. Hu, "Topological characters inFe(te1-xSex)thin films," *Physical Review B*, vol. 93, mar 2016.

[35] P. Zhang, K. Yaji, T. Hashimoto, Y. Ota, T. Kondo, K. Okazaki, Z. Wang, J. Wen, G. D. Gu, H. Ding, and S. Shin, "Observation of topological superconductivity on the surface of an iron-based superconductor," *Science*, vol. 360, pp. 182–186, mar 2018.

[36] Y. Cao, V. Fatemi, S. Fang, K. Watanabe, T. Taniguchi, E. Kaxiras, and P. Jarillo-Herrero, "Unconventional superconductivity in magic-angle graphene superlattices," *Nature*, vol. 556, pp. 43–50, mar 2018.

[37] M. Kayyalha, D. Xiao, R. Zhang, J. Shin, J. Jiang, F. Wang, Y.-F. Zhao, L. Zhang, K. M. Fijalkowski, P. Mandal, M. Winnerlein, C. Gould, Q. Li, L. W. Molenkamp, M. H. W. Chan, N. Samarth, and C.-Z. Chang, "Non-majorana origin of the half-quantized conductance plateau in quantum anomalous hall insulator and superconductor hybrid structures," *arXiv:1904.06463*, 2019.

[38] P. Zhang, L. Pan, G. Yin, Q.-L. He, and K. L. Wang, "A note on half-quantized conductance plateau of chiral majorana in quantum anomalous hall insulator and superconductor structures," *arXiv:1904.12396*, 2019.

[39] J. Alicea, "New directions in the pursuit of majorana fermions in solid state systems," *Reports on Progress in Physics*, vol. 75, no. 7, p. 076501, 2012.

[40] M. Sato and Y. Ando, "Topological superconductors: a review," *Reports on Progress in Physics*, vol. 80, p. 076501, may 2017.

[41] G. Chaudhary and A. H. MacDonald, "Vortex lattice structure and topological superconductivity in the quantum hall regime," *arXiv:1903.12249*, 2019.

[42] A. Altland and M. R. Zirnbauer, "Nonstandard symmetry classes in mesoscopic normal-superconducting hybrid structures," *Physical Review B*, vol. 55, pp. 1142–1161, jan 1997.

[43] A. P. Schnyder, S. Ryu, A. Furusaki, and A. W. W. Ludwig, "Classification of topological insulators and superconductors in three spatial dimensions," *Physical Review B*, vol. 78, nov 2008.

[44] A. Y. Kitaev, "Unpaired majorana fermions in quantum wires," *Physics-Uspekhi*, vol. 44, pp. 131–136, oct 2001.

[45] X.-L. Qi, T. L. Hughes, and S.-C. Zhang, "Topological field theory of time-reversal invariant insulators," *Physical Review B*, vol. 78, nov 2008.

[46] P. Ghosh, J. D. Sau, S. Tewari, and S. D. Sarma, "Non-abelian topological order in noncentrosymmetric superconductors with broken time-reversal symmetry," *Physical Review B*, vol. 82, nov 2010.

[47] S. Tewari and J. D. Sau, "Topological invariants for spin-orbit coupled superconductor nanowires," *Physical Review Letters*, vol. 109, oct 2012.

[48] S. D. Sarma, M. Freedman, and C. Nayak, "Majorana zero modes and topological quantum computation," *npj Quantum Information*, vol. 1, p. 15001, 2015.

[49] B. A. Bernevig, *Topological Insulators and Topological Superconductors*. LSU Press, 2013.

[50] J. Wang, Q. Zhou, B. Lian, and S.-C. Zhang, "Chiral topological superconductor and half-integer conductance plateau from quantum anomalous hall plateau transition," *Phys. Rev. B*, vol. 92, p. 064520, Aug 2015.

[51] E. J. Fox, I. T. Rosen, Y. Yang, G. R. Jones, R. E. Elmquist, X. Kou, L. Pan, K. L. Wang, and D. Goldhaber-Gordon, "Part-per-million quantization and current-induced breakdown of the quantum anomalous hall effect," *Physical Review B*, vol. 98, aug 2018.

[52] Q. Liu, C.-X. Liu, C. Xu, X.-L. Qi, and S.-C. Zhang, "Magnetic impurities on the surface of a topological insulator," *Physical Review Letters*, vol. 102, apr 2009.

[53] Y. L. Chen, J.-H. Chu, J. G. Analytis, Z. K. Liu, K. Igarashi, H.-H. Kuo, X. L. Qi, S. K. Mo, R. G. Moore, D. H. Lu, M. Hashimoto, T. Sasagawa, S. C. Zhang, I. R. Fisher, Z. Hussain, and Z. X. Shen, "Massive dirac fermion on the surface of a magnetically doped topological insulator," *Science*, vol. 329, pp. 659–662, aug 2010.

[54] R. Yu, W. Zhang, H.-J. Zhang, S.-C. Zhang, X. Dai, and Z. Fang, "Quantized anomalous hall effect in magnetic topological insulators," *Science*, vol. 329, pp. 61–64, jun 2010.

[55] D. J. J. Marchand and M. Franz, "Lattice model for the surface states of a topological insulator with applications to magnetic and exciton instabilities," *Physical Review B*, vol. 86, oct 2012.

[56] T. Fukui, Y. Hatsugai, and H. Suzuki, "Chern numbers in discretized brillouin zone: Efficient method of computing (spin) hall conductances," *Journal of the Physical Society of Japan*, vol. 74, pp. 1674–1677, jun 2005.

[57] A. C. Potter and P. A. Lee, "Multichannel generalization of kitaev's majorana end states and a practical route to realize them in thin films," *Physical Review Letters*, vol. 105, nov 2010.

[58] J. Alicea, Y. Oreg, G. Refael, F. von Oppen, and M. P. A. Fisher, "Non-abelian statistics and topological quantum information processing in 1d wire networks," *Nature Physics*, vol. 7, pp. 412–417, feb 2011.

[59] S. Plugge, A. Rasmussen, R. Egger, and K. Flensberg, "Majorana box qubits," *New Journal of Physics*, vol. 19, p. 012001, jan 2017.

[60] F. Pientka, A. Keselman, E. Berg, A. Yacoby, A. Stern, and B. I. Halperin, "Topological superconductivity in a planar josephson junction," *Physical Review X*, vol. 7, may 2017.

[61] M. Hell, M. Leijnse, and K. Flensberg, "Two-dimensional platform for networks of majorana bound states," *Physical Review Letters*, vol. 118, mar 2017.

[62] T. Karzig, C. Knapp, R. M. Lutchyn, P. Bonderson, M. B. Hastings, C. Nayak, J. Alicea, K. Flensberg, S. Plugge, Y. Oreg, C. M. Marcus, and M. H. Freedman, "Scalable designs for quasiparticle-poisoning-protected topological quantum computation with majorana zero modes," *Physical Review B*, vol. 95, jun 2017.

[63] C.-Z. Chen, J. J. He, D.-H. Xu, and K. T. Law, "Effects of domain walls in quantum anomalous hall insulator/superconductor heterostructures," *Physical Review B*, vol. 96, jul 2017.

[64] W. Ji and X.-G. Wen, "$\frac{1}{2}(e^2/h)$ conductance plateau without 1d chiral majorana fermions," *Phys. Rev. Lett.*, vol. 120, p. 107002, Mar 2018.

[65] Y. Huang, F. Setiawan, and J. D. Sau, "Disorder-induced half-integer quantized conductance plateau in quantum anomalous hall insulator-superconductor structures," *Phys. Rev. B*, vol. 97, p. 100501, Mar 2018.

[66] B. Lian, J. Wang, X.-Q. Sun, A. Vaezi, and S.-C. Zhang, "Quantum phase transition of chiral majorana fermions in the presence of disorder," *Phys. Rev. B*, vol. 97, p. 125408, Mar 2018.

[67] R. S. K. Mong, D. J. Clarke, J. Alicea, N. H. Lindner, P. Fendley, C. Nayak, Y. Oreg, A. Stern, E. Berg, K. Shtengel, and M. P. A. Fisher, "Universal topological quantum computation from a superconductor-abelian quantum hall heterostructure," *Phys. Rev. X*, vol. 4, p. 011036, Mar 2014.

[68] G. S. Jeon, J. K. Jain, and C. X. Liu, "Topological superconductivity in landau levels," *Physical Review B*, 2019.

[69] A. H. MacDonald, H. Akera, and M. R. Norman, "Landau quantization and particle-particle ladder sums in a magnetic field," *Physical Review B*, vol. 45, pp. 10147–10150, may 1992.

[70] M. R. Norman, A. H. MacDonald, and H. Akera, "Magnetic oscillations and quasiparticle band structure in the mixed state of type-ii superconductors," *Phys. Rev. B*, vol. 51, pp. 5927–5942, Mar 1995.

[71] M. Tinkham, *Introduction to Superconductivity.* Dover Publications, Inc., Mineola, New York, 1996.

[72] B. Zocher and B. Rosenow, "Topological superconductivity in quantum hall˘superconductor hybrid systems," *Phys. Rev. B*, vol. 93, p. 214504, Jun 2016.

[73] S. B. Chung, X.-L. Qi, J. Maciejko, and S.-C. Zhang, "Conductance and noise signatures of majorana backscattering," *Physical Review B*, vol. 83, mar 2011.

[74] T. Liu and M. Franz, "Electronic structure of topological superconductors in the presence of a vortex lattice," *Phys. Rev. B*, vol. 92, p. 134519, Oct 2015.

[75] J. M. Murray and O. Vafek, "Majorana bands, berry curvature, and thermal hall conductivity in the vortex state of a chiralp-wave superconductor," *Physical Review B*, vol. 92, oct 2015.

[76] H. B. Heersche, P. Jarillo-Herrero, J. B. Oostinga, L. M. K. Vandersypen, and A. F. Morpurgo, "Bipolar supercurrent in graphene," *Nature*, vol. 446, pp. 56–59, mar 2007.

[77] X. Du, I. Skachko, and E. Y. Andrei, "Josephson current and multiple andreev reflections in graphene SNS junctions," *Physical Review B*, vol. 77, may 2008.

[78] M. T. Allen, O. Shtanko, I. C. Fulga, A. R. Akhmerov, K. Watanabe, T. Taniguchi, P. Jarillo-Herrero, L. S. Levitov, and A. Yacoby, "Spatially resolved edge currents and guided-wave electronic states in graphene," *Nature Physics*, vol. 12, pp. 128–133, nov 2015.

[79] L. Bretheau, J. I.-J. Wang, R. Pisoni, K. Watanabe, T. Taniguchi, and P. Jarillo-Herrero, "Tunnelling spectroscopy of andreev states in graphene," *Nature Physics*, vol. 13, pp. 756–760, may 2017.

[80] S.-Y. Xu, N. Alidoust, I. Belopolski, A. Richardella, C. Liu, M. Neupane, G. Bian, S.-H. Huang, R. Sankar, C. Fang, B. Dellabetta, W. Dai, Q. Li, M. J. Gilbert, F. Chou, N. Samarth, and M. Z. Hasan, "Momentum-space imaging of cooper pairing in a half-dirac-gas topological superconductor," *Nature Physics*, vol. 10, pp. 943–950, nov 2014.

[81] K. Nomura and A. H. MacDonald, "Quantum hall ferromagnetism in graphene," *Physical Review Letters*, vol. 96, jun 2006.

[82] Z. Jiang, Y. Zhang, H. L. Stormer, and P. Kim, "Quantum hall states near the charge-neutral dirac point in graphene," *Physical Review Letters*, vol. 99, sep 2007.

[83] J. G. Checkelsky, L. Li, and N. P. Ong, "Zero-energy state in graphene in a high magnetic field," *Physical Review Letters*, vol. 100, may 2008.

[84] A. F. Young, C. R. Dean, L. Wang, H. Ren, P. Cadden-Zimansky, K. Watanabe, T. Taniguchi, J. Hone, K. L. Shepard, and P. Kim, "Spin and valley quantum hall ferromagnetism in graphene," *Nature Physics*, vol. 8, pp. 550–556, may 2012.

[85] M. Cheng, R. M. Lutchyn, V. Galitsk, , and S. D. Sarma, "Splitting of majorana-fermion modes due to intervortex tunneling in a $p_x + ip_y$ superconductor," *Phys. Rev. Lett.*, vol. 103, p. 107001, Aug. 2009.

[86] R. R. Biswas, "Majorana fermions in vortex lattices," *Physical Review Letters*, vol. 111, sep 2013.

[87] P. Rickhaus, M. Weiss, L. Marot, and C. Schönenberger, "Quantum hall effect in graphene with superconducting electrodes," *Nano Letters*, vol. 12, pp. 1942–1945, mar 2012.

[88] M. B. Shalom, M. J. Zhu, V. I. Fal'ko, A. Mishchenko, A. V. Kretinin, K. S. Novoselov, C. R. Woods, K. Watanabe, T. Taniguchi, A. K. Geim, and J. R. Prance, "Quantum oscillations of the critical current and high-field superconducting proximity in ballistic graphene," *Nature Physics*, vol. 12, pp. 318–322, dec 2015.

[89] F. Amet, C. T. Ke, I. V. Borzenets, J. Wang, K. Watanabe, T. Taniguchi, R. S. Deacon, M. Yamamoto, Y. Bomze, S. Tarucha, and G. Finkelstein, "Supercurrent in the quantum hall regime," *Science*, vol. 352, pp. 966–969, may 2016.

[90] Z. Tešanović and M. Rasolt, "New type of superconductivity in very high magnetic fields," *Physical Review B*, vol. 39, pp. 2718–2721, feb 1989.

[91] Z. Tešanović, M. Rasolt, and L. Xing, "Superconductivity in a very high magnetic field," *Physical Review B*, vol. 43, pp. 288–298, jan 1991.

[92] H. Akera, A. H. MacDonald, S. M. Girvin, and M. R. Norman, "Vortex-lattice states at strong magnetic fields," *Phys. Rev. Lett.*, vol. 67, pp. 2375–2378, Oct 1991.

[93] G. Chaudhary, X. Li, and A. H. MacDonald, "Mean-field superconductivity in dirac-cone at high magnetic field," in *APS March Meeting, New Orelans, 2017.*, 2017.

[94] A. L. Fetter and J. D. Walecka, *Quantum Theory of Many-Particle Systems*. Dover Publications Inc., 2003.

[95] A. Rajagopal and R. Vasudevan, "De haas-van alphen oscillations in the critical temperature of type II superconductors," *Physics Letters*, vol. 23, pp. 539–540, nov 1966.

[96] L. W. Gruenberg and L. Gunther, "Effect of orbital quantization on the critical field of type-II superconductors," *Physical Review*, vol. 176, pp. 606–613, dec 1968.

[97] Z. Tešanović, M. Rasolt, and L. Xing, "Quantum limit of a flux lattice: Superconductivity and magnetic field in a new relationship," *Physical Review Letters*, vol. 63, pp. 2425–2428, nov 1989.

[98] T. Maniv, A. I. Rom, I. D. Vagner, and P. Wyder, "de haas–van alphen effect in the superconducting state of a two-dimensional metal," *Physical Review B*, vol. 46, pp. 8360–8375, oct 1992.

[99] M. Norman, H. Akera, and A. MacDonald, "Mean-field superconductivity in a strong magnetic field," *Physica C: Superconductivity*, vol. 196, pp. 43–47, jun 1992.

[100] M. G. Vavilov and V. P. Mineev, "de haas-van alphen effect in superconductors," *Journal of Experimental and Theoretical Physics*, vol. 85, pp. 1024–1034, nov 1997.

[101] V. P. Mineev, "Phase transition into the superconducting mixed state and the de haas-van alphen effect," *Philosophical Magazine B*, vol. 80, pp. 307–321, mar 2000.

[102] V. Zhuravlev and T. Maniv, "Exact analytic gorkov-ginzburg-landau theory of type-II superconductivity in the magnetoquantum oscillations limit," *Physical Review B*, vol. 85, mar 2012.

[103] M. Rasolt and Z. Tesanovic, "Theoretical aspects of superconductivity in very high magnetic fields," *Reviews of Modern Physics*, vol. 64, pp. 709–754, jul 1992.

[104] T. Maniv, V. Zhuravlev, I. Vagner, and P. Wyder, "Vortex states and quantum magnetic oscillations in conventional type-II superconductors," *Reviews of Modern Physics*, vol. 73, pp. 867–911, nov 2001.

[105] K. W. Song and A. E. Koshelev, "Strong landau-quantization effects in high-magnetic-field superconductivity of a two-dimensional multiple-band metal near the lifshitz transition," *Physical Review B*, vol. 95, may 2017.

[106] M. Yankowitz, S. Chen, H. Polshyn, Y. Zhang, K. Watanabe, T. Taniguchi, D. Graf, A. F. Young, and C. R. Dean, "Tuning superconductivity in twisted bilayer graphene," *Science*, vol. 363, pp. 1059–1064, jan 2019.

[107] X. Lu, P. Stepanov, W. Yang, M. Xie, M. A. Aamir, I. Das, C. Urgell, K. Watanabe, T. Taniguchi, G. Zhang, A. Bachtold, A. H. MacDonald, and D. K. Efetov, "Superconductors, orbital magnets, and correlated states in magic angle bilayer graphene," *arXiv:1903.06513*, 2019.

[108] X. Liu, Z. Hao, E. Khalaf, J. Y. Lee, K. Watanabe, T. Taniguchi, A. Vishwanath, and P. Kim, "Spin-polarized correlated insulator and superconductor in twisted double bilayer graphene," *arXiv:1903.08130*, 2019.

[109] R. Bistritzer and A. H. MacDonald, "Moire bands in twisted double-layer graphene," *Proceedings of the National Academy of Sciences*, vol. 108, pp. 12233–12237, jul 2011.

[110] C. W. J. Beenakker, "Specular andreev reflection in graphene," *Physical Review Letters*, vol. 97, aug 2006.

[111] A. MacDonald, H. Akera, and M. Norman, "Quantum mechanics and superconductivity in a magnetic field," *Australian Journal of Physics*, vol. 46, no. 3, p. 333, 1993.

[112] P. Fulde and R. A. Ferrell, "Superconductivity in a strong spin-exchange field," *Physical Review*, vol. 135, pp. A550–A563, aug 1964.

[113] L. A.I. and O. Y. N., "Inhomogeneous state of superconductor," *Sov. Phys. JETP. 20: 762-769(1965)*, 1965.

[114] G. Tarnopolsky, A. J. Kruchkov, and A. Vishwanath, "Origin of magic angles in twisted bilayer graphene," *Physical Review Letters*, vol. 122, mar 2019.

[115] N. Bultinck, S. Chatterjee, and M. P. Zaletel, "Anomalous hall ferromagnetism in twisted bilayer graphene," *arXiv:1901.08110*, 2019.

[116] G. Chaudhary and A. H. MacDonald, "The evolution of landau levels near magic angles in twisted bilayer graphene." unpublished.

[117] N. H. Lindner, E. Berg, G. Refael, and A. Stern, "Fractionalizing majorana fermions: Non-abelian statistics on the edges of abelian quantum hall states," *Physical Review X*, vol. 2, oct 2012.

[118] D. K. Efetov, L. Wang, C. Handschin, K. B. Efetov, J. Shuang, R. Cava, T. Taniguchi, K. Watanabe, J. Hone, C. R. Dean, and P. Kim, "Specular interband andreev reflections at van der waals interfaces between graphene and NbSe2," *Nature Physics*, vol. 12, pp. 328–332, dec 2015.

[119] G.-H. Lee, K.-F. Huang, D. K. Efetov, D. S. Wei, S. Hart, T. Taniguchi, K. Watanabe, A. Yacoby, and P. Kim, "Inducing superconducting correlation in quantum hall edge states," *Nature Physics*, vol. 13, pp. 693–698, apr 2017.

[120] C. Brun, T. Cren, and D. Roditchev, "Review of 2d superconductivity: the ultimate case of epitaxial monolayers," *Superconductor Science and Technology*, vol. 30, p. 013003, nov 2016.

[121] M. P. Anantram and S. Datta, "Current fluctuations in mesoscopic systems with andreev scattering," *Physical Review B*, vol. 53, pp. 16390–16402, jun 1996.

[122] H. Hoppe, U. Zülicke, and G. Schön, "Andreev reflection in strong magnetic fields," *Physical Review Letters*, vol. 84, pp. 1804–1807, feb 2000.

[123] C. Caroli, P. D. Gennes, and J. Matricon, "Bound fermion states on a vortex line in a type II superconductor," *Physics Letters*, vol. 9, pp. 307–309, may 1964.

[124] N. B. Kopnin and M. M. Salomaa, "Mutual friction in superfluidHe3: Effects of bound states in the vortex core," *Physical Review B*, vol. 44, pp. 9667–9677, nov 1991.